BRNO UNIVERSITY OF TECHNOLOGY
VYSOKÉ UČENÍ TECHNICKÉ V BRNĚ

CENTRAL EUROPEAN INSTITUTE OF TECHNOLOGY BUT
STŘEDOEVROPSKÝ TECHNOLOGICKÝ INSTITUT VUT

PROCESSING OF AEROGEL COATINGS ON BULK MATERIALS SUBSTRATES

PŘÍPRAVA AEROGELOVÝCH POVRCHOVÝCH ÚPRAV NA OBJEMOVÝCH MATERIÁLECH

DOCTORAL THESIS
DIZERTAČNÍ PRÁCE

AUTHOR
AUTOR PRÁCE
Jorge Alberto Torres Rodríguez

SUPERVISOR
ŠKOLITEL
prof. Ing. Jozef Kaiser, Ph.D.

BRNO 2019

ABSTRACT

In this thesis, a systematic study of the synthesis and processing of advanced thermal-stable aerogels for potential high-temperature applications was carried out. The first part of this work details the synthetic implications to prepare an aerogel and its applications along with a description of the sol-gel coatings deposition techniques. The experimental procedure is divided into three sections. The first one shows the followed synthetic protocols to prepare ZrO_2, YSZ, $Ln_2Zr_2O_7$ (*Ln* = La^{3+}, Nd^{3+}, Gd^{3+}, and Dy^{3+}) aerogels, and $Ln_2Zr_2O_7$ powders and xerogels. Then is described the used deposition method to prepare aerogel coatings on metallic substrates. Followed this, the characterization techniques are specified. It was found that the amount of water and nitric acid plays a determinant role to obtain suitable wet gels to transform into aerogels. Upon calcination at 500 °C, the ZrO_2 and YSZ aerogels have a high surface area up to 114 m^2 g^{-1}, however, at 1000 °C, complete densification occurs losing all their porous structure. In comparison with the ZrO_2 and YSZ, the $Ln_2Zr_2O_7$ aerogels are thermally more stable since preserves their porosity at elevated calcination (1000 °C) with values >160 m^2 g^{-1}. In the studied temperature range, the ZrO_2 aerogel experiment a complex tetragonal ↔ monoclinic phase transition driven by the crystallite size, while the YSZ is constituted by single-tetragonal phase. The phase composition of the rare-earth zirconates is highly dependent on the synthesis method; all the $Ln_2Zr_2O_7$ materials are pyrochlore or fluorite crystalline phases. The direct casting of the aerogel on the metallic substrate yield completely broken coatings due to effect of shrinkage, while the slurry dip-coating allowed to fabricate homogeneous, thick, and coarse aerogel coatings. These coatings do not present phase changes and remain highly porous after different heat treatments.

ABSTRAKT

Tato práce se zabývá systematickou studií syntézy a zpracováním pokročilých tepelně stabilních aerogelů pro potenciální vysokoteplotní aplikace. V první části dizertační práce jsou podrobně popsány syntetické implikace pro přípravu aerogelů a jejich aplikace spolu s popisem depozičních metod povlaků vytvořených pomocí sol-gel procesu. Experimentální postup je rozdělen do tří částí. První z nich představuje syntetické protokoly k přípravě ZrO_2, YSZ, $Ln_2Zr_2O_7$ (*Ln* = La^{3+}, Nd^{3+}, Gd^{3+}, and Dy^{3+}) aerogelů, $Ln_2Zr_2O_7$ prášků a xerogelů. Dále

je popsána depoziční metoda, která byla použita pro přípravu povlaků z aerogelů na kovových substrátech. Poté jsou následně specifikovány techniky, jež byly použity pro charakterizaci. Bylo zjištěno, že množství vody a kyseliny dusičné hraje rozhodující roli v přípravě gelů vhodných pro transformaci na aerogely. Po kalcinaci při 500 °C mají ZrO_2 a YSZ aerogely velký povrch, a to až do 114 m^2 g^{-1}, avšak při 1000 °C dochází k úplnému zhuštění a ztrácí se tak veškerá jejich porézní struktura. Naopak ve srovnání s ZrO_2 and YSZ jsou aerogely $Ln_2Zr_2O_7$ tepelně stabilnější, protože si zachovávají svou porozitu při vyšší kalcinační teplotě (1000 °C), při které dosahují hodnot > 160 m2 g-1. Experimentálně bylo dále zjištěno, že ve studovaném teplotním rozsahu ZrO_2 aerogel tvoří tetragonální komplex ↔ monoklinický fázový přechod řízený velikostí krystalitů, zatímco YSZ je tvořena jedinou tetragonální fází. Fázové složení zirkoničitanů vzácných zemin je vysoce závislé na způsobu syntézy; všechny $Ln_2Zr_2O_7$ materiály jsou pyrochlorické nebo fluoritové krystalické fáze. Přímým odléváním aerogelu na kovový substrát dochází k úplnému rozpraskání povlaku z důvodu smršťování, zatímco máčením kovového substrátu v suspenzi je možné vyrobit homogenní, silné a hrubé povlaky z aerogelu. Tyto povlaky neobsahují fázové změny a zůstávají vysoce porézní i po různých tepelných úpravách.

KEYWORDS

Soft chemistry, sol-gel, zirconates, xerogels, supercritical drying, aerogels

KLÍČOVÁ SLOVA

Soft chemistry, sol-gel, zirkoničitany, xerogely, superkritické sušení, aerogely

ACKNOWLEDGMENTS

I would like to sincerely thank all the people who helped me during my doctoral studies at the Central European Institute of Technology (CEITEC), in Brno, Czech Republic. Special mention to my supervisor Prof. Jozef Kaiser and my co-supervisor Assoc. Prof. Ladislav Čelko for opening the doors to do research in their Materials Characterization and Advanced Coatings Research Group and their invested time throughout my studies.

Deep gratitude to Ph.D. Melita Menelaou for help, guidance, and formation in the research world. Your guidance and teachings were of great help to be able to complete this research. Thank you.

My best gratefulness to all my friends and colleagues that I meet throughout these years. To my great friend of many years Mariano, your support, help, and uncountable advice was essential, not only during the Ph.D. but also in my life. Thank you.

I would like to sincerely acknowledge the CEITEC Ph.D. Scholarship and Erasmus+ program for funding my doctoral studies.

All my love and thankfulness to my parents. Your patience, support, and love were my daily motivation.

SWORN STATEMENT

I hereby declare that I have written the Ph.D. thesis on my own according to advice of my supervisor Prof. Jozef Kaiser and that all the literary sources are quoted correctly and completely. This dissertation thesis is the property of the Central European Institute of Technology (CEITEC), Brno University of Technology (BUT), Czech Republic and it can be used for commercial purposes only with consent of the doctoral thesis supervisor and the director of CEITEC, BUT.

Jorge Alberto Torres Rodríguez

TORRES-RODRIGUEZ, J. *Processing of aerogel coatings on bulk material substrates*. Brno: Brno University of Technology, Central European Institute of Technology, 2019. 124 p. Dissertation supervisor: Prof. Eng. Jozef Kaiser, Ph.D.

Para mí amada esposa Diana y mi precioso hijo Santiago,

quienes iniciaron conmigo este viaje

CONTENTS

1. Introduction

Aerogels are unusual highly porous materials because of their distinctive microstructure consisting of small pores and nanoparticles. Commonly, aerogels are prepared by means of sol-gel chemistry in three main steps: (1) formation of a colloidal suspension or also called sol, (2) transformation of the sol into a solid three-dimensional network solvent-filled or wet gel, and (3) removal of the solvent within the structure to preserve the porous structure. The final aerogel is an air-filled porous structure, usually in monolithic or powder form. In their bulk form, aerogels have interesting physical properties such as high surface area (> 100 m^2 g^{-1}) and porosity, very low thermal conductivity (~0.01-0.02 W m^{-1} K^{-1}) and density (0.003-0.5 g cm^{-3}). These properties render them in a variety of applications in both scientific and industrial fields [1]. Most of these properties exhibited in the bulk form are also transferred to different forms of the aerogels, e.g. coatings and thin sheets.

The constantly rising demand for a number of applications requires the aerogels either as freestanding sheets or as thin coatings on different substrate materials. However, certain experimental details must be taken into account to prepare aerogels in such forms since the structure of the material is naturally weak and prone to experiment damage of the produced layer. During the last years, sol-gel processes have emerged to produce highly pure advanced ceramics in both bulk and coating shapes. Nevertheless, most of the scientific efforts in sol-gel coatings are focused on dense coatings, porous coatings aside. In comparison with dense ones, few reports have been published for processing porous sol-gel coatings.

To take advantage of the features of this material, new applications have emerged as in the energy and aerospace industries to enhance the thermal barrier coatings [2–5]. These devices require materials with low thermal conductivity and high stability to phase changes in their crystalline structure [6,7]. Some of these materials are yttria-stabilized zirconia (YSZ) and rare earth zirconates ($Ln_2Zr_2O_7$). Since aerogels can be prepared based on a large variety of metal oxides [1,8,9], the fusion of two novel materials such as rare-earth zirconates and aerogels for TBC applications was a great motivation for this research work. Thus, the present research details the development of a versatile synthetic methodology to produce ZrO_2, YSZ and rare earth zirconate aerogels of four lanthanides (La, Nd, Gd, and Dy) for future TBC applications. Moreover, a general study of sol-gel coatings deposition was carried out onto metallic substrates.

2. Literature review

This section surveys the literature and summarizes the development of aerogels, their production, different structural features, as well as sol-gel coatings preparation and applications.

Aerogel is an extremely porous system, which into a single material gathers outstanding properties such as very high surface area (>100 m^2 g^{-1}) and porosity (up to 98 % vol.), exceptionally low thermal conductivity (~0.01-0.02 W m^{-1} K^{-1}) and density (0.003-0.5 g cm^{-3}). It is formed by individual nanoparticles linked in a continuous random three-dimensional network. The aerogels are divide into two main categories, inorganic and organic; both prepared by the sol-gel method. This synthesis protocol of inorganic aerogels involves the preparation of a colloidal suspension (sol) of metallic oxide nanoparticles in an aqueous media (alcoholic solvent). To achieve this, mainly organic precursors and metallic-based compounds which undergoes a chemical reaction are necessary; thus, producing its respective metal oxide. At the beginning of the sol-gel process, the system is in liquid state but as the reactions proceed, the nanoparticles link progressively and the viscosity of the sol increases until it becomes a wet gel. A porous 3D network of metallic oxide filled with solvent builds this gel. Subsequently, the solvent is removed by a supercritical extraction to preserve the porous structure. The result is an aerogel (**Fig. 2.1**).

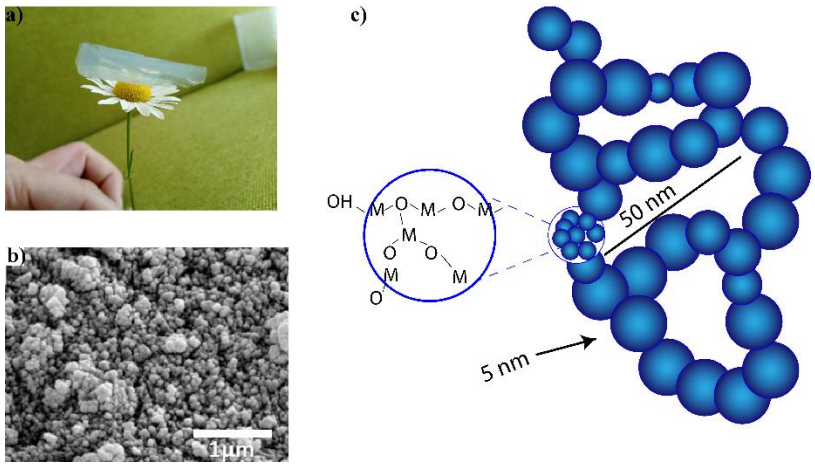

Fig. 2.1. SiO_2 aerogel; a) Photography of an aerogel synthesized with the ratio TMOS : MeOH : NH_3 : H_2O of 1 : 10 : 0.5 : 1; b) micrograph of an aerogel; c) representation of the microstructure depicted in b [10].

This material gathers several properties, among others, low thermal conductivity, refractive index, sound diffusion, and density, as well as extremely high surface area (**Table 2.1**). These properties in a single material confer them widespread applications in both science and industry fields.

Table 2.1 Physical properties of SiO_2 aerogels.

Properties	Value
Apparent density	0.003 – 0.5 g cm^3
Specific surface area	100 – 1500 m^2 g^{-1}
Solid percentage	0.13 – 0.15 vol.%
Mean pore diameter	~20 – 150 nm
Primary particle diameter	2 – 5 nm
Refractive index	1 – 1.05
Thermal tolerance	> 500 °C
Coefficient of thermal expansion	2 – 4 x10^{-6} K^{-1}
Dielectric constant	~1.1
Sound velocity	100 m s^{-1}
Optical transmittance	> 90 % (630 nm)

2.1. Synthesis of aerogels by sol-gel

The preparation of aerogels by sol-gel technique involves three elemental steps: (1) wet gel formation, (2) syneresis or aging, and (3) drying of the wet gel as depicted in **Fig. 2.2**.

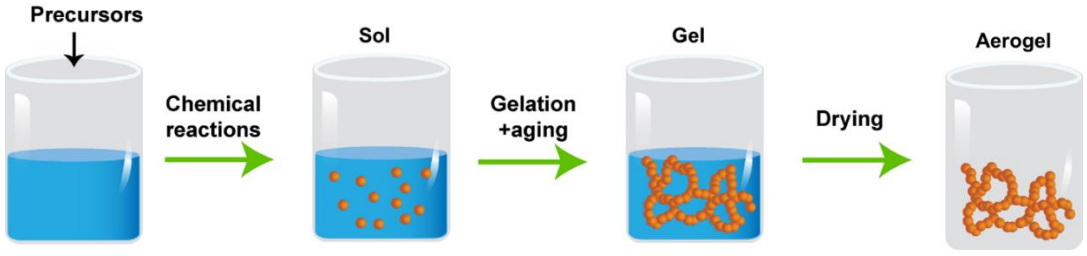

Fig. 2.2. Main steps in the synthesis of an aerogel material

2.1.1. Wet gel formation

A common way to complete the first stage is by hydrolysis and condensation reactions – also called sol-gel reactions – of alkoxides with organic solvents, water, and a catalyst. The alkoxides of general chemical formula $M(OR)_4$ (where M is a metal and R designates its parent alcohol) are characterized by a polar covalent bond M – O and are often in solution in their parent alcohol. These hydrolysis and condensation reactions are strongly affected by

process parameters such as the nature of the R group, the H_2O/alkoxide ratio and the catalyst. For instance, the sol-gel chemistry of silica is commonly driven by either acid or base catalysts since the reactions itself is quite slow. Therefore, the catalyst affects the properties of the final material since the given hydrolysis and condensation reactions kinetics are a function of the acid/base catalyst and its concentration (see **Scheme 2.1**).

The first reaction is hydrolysis which induces the substitution of the metal-bonded alkoxy group (–OR) by a hydroxyl (-OH). During this process, a pentacoordinate transition state occurs in both acid (**Scheme 2.1a**) or base-catalyzed reactions (**Scheme 2.1b**). Depending on the conditions and the Si/H_2O ratio, more than one alkoxy group may be hydrolyzed (**Eq. 2.1**). The rate of each hydrolysis step depends on the stability of the pentacoordinate transition state, which in turn depends on the relative electron-withdrawing or donating power of –OH against –OR groups. Thus, the result is that the hydrolysis is slower under acidic conditions and faster under basic conditions.

$$Si(OR)_4 + nH_2O \rightarrow Si(OR)_{4-n}(OH)_n + nROH \qquad \textbf{(Eq. 2.1)}$$

Scheme 2.1. General hydrolysis mechanism of Si-based alkoxides; a) acid-catalyzed, b) base-catalyzed [11].

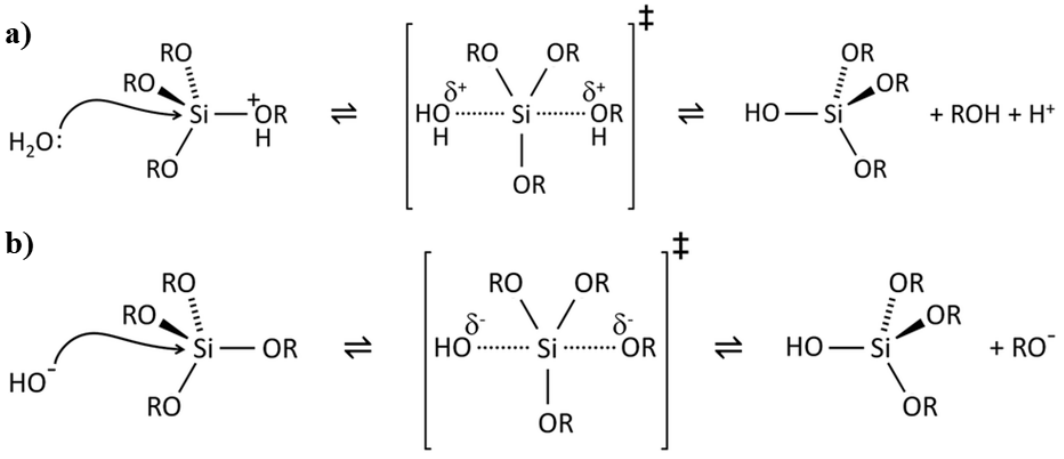

During the condensation reactions, two silanol groups react together and lead to the formation of siloxane bonds (or metaloxane bonds for different metals). Similar to the hydrolysis, the progress of the condensation reactions is a function of the hydrolysis degree. Namely, if there is a complete hydrolysate before the condensation reactions start, the $(OH)_3$Si-O-Si$(OH)_3$ formation takes place which has 6 active sites available to the condensation reactions that follow. The complete hydrolysis occurs when the reactions are

base-catalyzed and hydrolysis occurs progressively faster. Thus, multiple condensation reactions outcome in small, highly branched agglomerates dispersed in the sol which ultimately crosslinks to form a wet gel. Contrary to the base-catalyzed sol-gel reactions, under acidic conditions, the condensation reactions take place on terminal silanols (Si – OH) and chain-like structures are formed that lead to the formation of network-like gels. Both base and acid-catalyzed sol-gel reactions are represented in **Fig. 2.3** and **Scheme 2.2**.

Scheme 2.2. General condensation mechanism of Si-based alkoxides; a) acid-catalyzed, b) base-catalyzed [11].

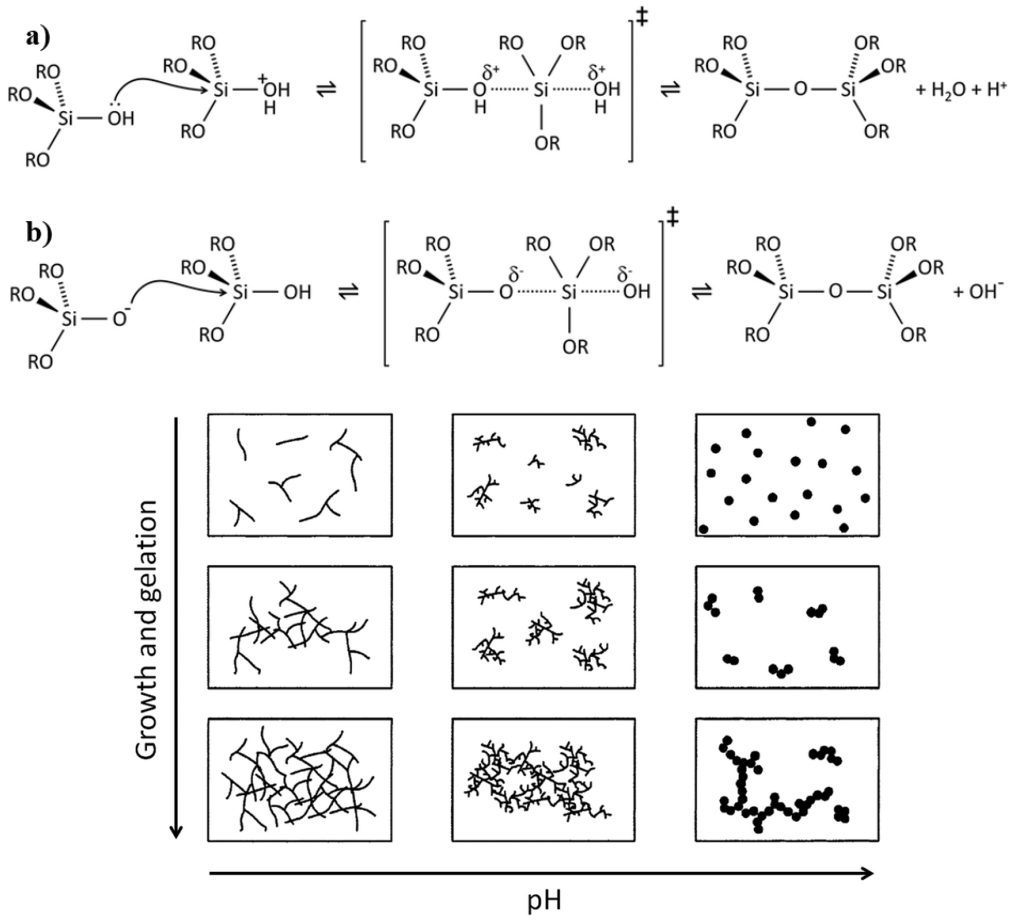

Fig. 2.3. Schematic representation of the progressive gel formation as function of pH [12].

Not only the catalyst has a direct influence on the hydrolysis and condensation kinetics and consequently in the final structure of the silica gels, but also there are other several factors. For instance, the alkoxide : water ratio can be tuned to limit hydrolysis. In addition, the nature and concentration of the solvent affect the molecular level mixing or even change

the solvent – alkoxide interaction. The length of the R chain of the alkoxide may produce inductive or steric impedance effects, which result in modification of the hydrolysis rates. Even, when other metal alkoxides are used (i.e. Zr- or Ti-based), the use of chelating agents such as acetylacetone (Acac) are necessary to reduce the very fast hydrolysis and condensation rates due the highly reactive nature of these alkoxide precursors.

The above-described mechanisms are not exclusive of the Si-based sol-gel reactions but also, other metal alkoxides follow similar pathways. Many other alkoxides to perform the sol-gel reactions are based on the elements with considerable lower electronegativity than Si such as Zr and Ti. Such electronegativity makes the metal atoms in the alkoxides prone to nucleophilic attack – nucleophile is a chemical species that donates an electron pair to form a chemical bond in relation to a reaction. The so-called partial charge model [13] allows calculating the partial charge (δ^+ or δ^-) of each atom in a given molecule and thus estimate its stability and reactivity. In summary, the higher the δ^+ value of a metal atom in an alkoxide, the higher the susceptibility to a nucleophilic attack from oxygen atoms of water molecules (hydrolysis) holding a δ^-. For instance, in four-coordinate alkoxides (e.g. $Si(OEt)_4$, $Ti(OEt)_4$, $Zr(OEt)_4$) the partial charges of Si, Ti, and Zr are +0.32, +0.63, and +0.74, respectively [12]. As Si atoms carry a moderate charge (+0.32), the kinetics of the global reactions of Si alkoxides is slow and the use of a catalyst is needed [14]. On the other hand, Zr atoms have considerably high charge (+0.74) which means that the metal reacts vigorously with water to produce precipitates [15–18]. In the case of Zr-based alkoxides, to control their hydrolysis/condensation reactions the use of additional additives is required. Most of the used additives are chelating agents like acetylacetone and propylene oxide to substitute for some of the alkoxide groups on the Zr. The strength of binding of the chelating agent along with the ligand : alkoxide ratio has an important effect on the reactivity of the zirconium precursor and the structural properties of the resulting wet gel [19]. The control of the sol-gel chemistry in this way has enabled the synthesis of several nanostructures for a wide range of applications such as catalysts, thermal insulator, drug carrier system, protective and insulation coatings, etc. [20–23]

2.2. Aging step

Regardless of the applied synthetic protocol to prepare a wet gel as discussed in the previous section, an aging step is always needed to complete the involved reactions and strengthen the solid structure. Despite the fact that the sol loses its fluidity and turns into a rigid gel, the sol-gel reactions continue due to the oxide backbone creates the pores in the wet gel and a significant amount of unreacted species are retained into the porous structure. In a wet gel, two main chemical processes are interacting during the aging: Syneresis and Ostwald-ripening [24]. The syneresis is the shrinkage of the gel network resulting in expulsion of liquid from the pores. This process is caused by the further condensation reactions after gelation due to these reactions continues by the presence of active hydroxyl groups. If two adjacent hydroxyl groups condense, on a network particle/surface, the newly formed metaloxane bond (M – O – M) occupies less space than the previously existing M – OH groups which lead to the expulsion of the liquid from the pores. This causes changes in the pore size distribution. In **Fig. 2.4**, a schematic representation is shown.

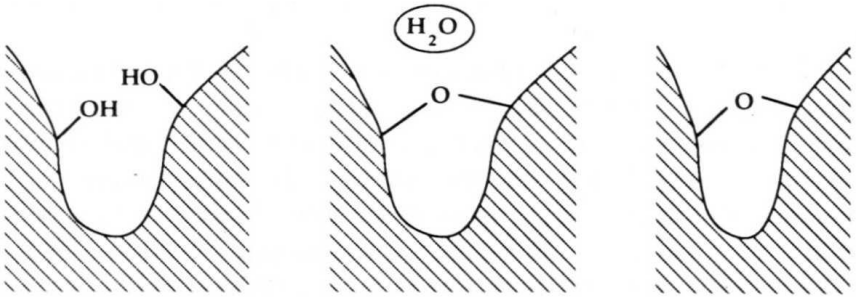

Fig. 2.4. Syneresis process in a wet gel [24].

The second process that takes place simultaneously is the ripening also called coarsening. This is a dissolution process and re-precipitation is driven by differences in solubility between surfaces with different radii of curvature. In other words, the smaller the particle, the greater is the solubility. Thus, smaller particles dissolve and the solute precipitates onto larger particles. The result is the reduction of the net curvature of the solid phase, in addition, small particles disappear and small pores are filled. A description is depicted in **Fig. 2.5**. The structural changes, which take place during aging, have a direct impact on the final properties of the aerogels.

Despite there are diverse treatments to enhance the stiffness of the sold network, two methods are the most applied ones: the increased aging temperature and aging solution composition. For instance, Einarsrud *et.al.* [25–27] have demonstrated that not only the aging period can be accelerated more than 40 times by aging the wet gels at 100 °C, but it also strengthens the structure.

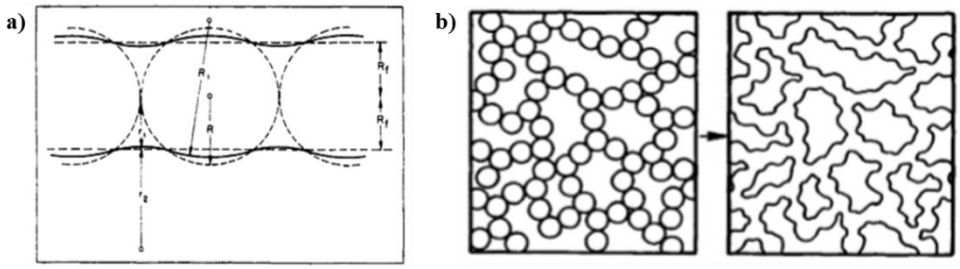

Fig. 2.5. Ripening process during aging; a) Dissolved silica redeposits from positive curvature to areas of negative curvature; b) The three-dimensional network progress to a coarser structure [25].

The strengthening is also possible by soaking the prepared wet gels into the precursor solvent to remove unreacted species. Additionally, the gels can be immersed into a solution containing the precursor alkoxide [28] or replacing the original solvent by another with higher solubility such as acetone [29]. Because this process is diffusion-controlled, the shape and dimensions are variables to consider, i.e., the larger the gel, the longer is the aging process. Another feature of this important step is the removal of residual water because it is not extracted during the supercritical drying step and its presence within the structure frequently results in opaque or cracked monoliths.

2.3. From gel to aerogel: Drying

Once the wet gel is formed and aged, the continuous porous network filled with solvent can be represented as shown in **Fig. 2.6**. The next step is to extract the solvent from the pores. However, since the wet gel is a solid – liquid system and interacts with air, there is the coexistence of solid – vapor (γ_{s-v}), liquid – vapor (γ_{l-v}), and solid – liquid interfaces (γ_{s-l}) which independently have a specific energy value. The difference in the specific energy of these interfaces result in capillary pressure (P_{cap}) and for a cylindrical shape is expressed, see Eq. 2.2, as follows [24]:

$$P_{cap} - \frac{2\gamma_{l-v}\,cos\theta}{r} \qquad \textbf{(Eq. 2.2)}$$

Where θ is the contact angle formed by the liquid – gas meniscus (**Fig. 2.6**) and r is the capillary radius. The implication of the capillary pressure in the drying of gels is not related to the vapor pressure itself, but rather to its effect on the solid phase. Thus, if the solvent (with capillary pressure on the solid network) is evaporated while the forces are still interacting, the porous structure shrinks and the result is a dense material or **xerogel**.

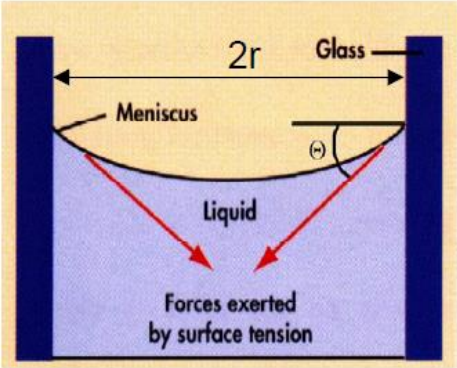

Fig. 2.6. Illustration of the capillary forces in the meniscus [30].

2.3.1. Supercritical drying

Highly shrunk xerogels as a product of uncontrolled drying own certain degree of porosity which confers them high surface area in comparison with dense materials [31–33]. However, when a larger volume and very high surface area are required, the capillary forces must be avoided. In this context, gels can be dried under supercritical conditions to produce aerogels with up to 98 % of porosity by its volume. During this process, a liquid replaces the liquid filling the pores. Then, when the liquid is subjected to pressure and temperature higher than its critical point (critical pressure Pc and critical temperature Tc) the fluid is in supercritical state. A supercritical fluid acquires specific properties and has an intermediate behavior between that of a liquid and a gas. In particular, supercritical fluids (SCFs) possess liquid-like densities, gas-like viscosities and most important for this purpose no surface tension. Thus, when the SCF is into the porous structure the capillary forces are neglected.

In a typical supercritical drying (SCD) process, a previously aged wet gel is placed in a sealed autoclave. Then, a fluid (most used is liquid CO_2) is flushed into the device. Following a controlled increase of the temperature, which produces a substantial pressure raise. Once the desired temperature and pressure are reached (above critical conditions of the fluid), the

supercritical fluid expands into the container. After certain period at supercritical conditions, the fluid is slowly vented until ambient conditions are reached and an aerogel is obtained. A supercritical drying pathway is depicted in **Fig. 2.7**.

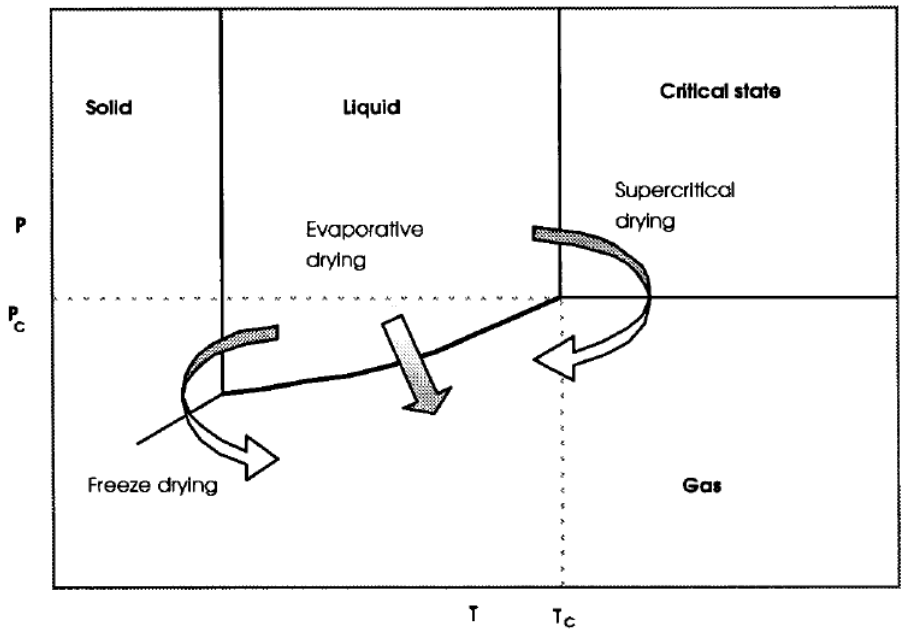

Fig. 2.7. Comparison of the drying methods to obtain aerogels [34].

2.3.2. Freeze-drying

Aerogels obtained by this method are often called cryogels due to the "cryo" conditions used in order to avoid the liquid-gas boundary. This process implies the solvent substitution in the pores by another with high sublimation pressure and low expansion coefficient. Once the replacement has been performed, the liquid is frozen and sublimed under a vacuum atmosphere. Some of the drawbacks of this method are that long aging periods are required and the obtained aerogels are in powder form due to frozen crystals often destroy the monolith [35–37].

2.3.3. Ambient drying

In the constant search for alternatives to obtain aerogels without the use of supercritical drying due to high costs for industrial applications, an emerging drying method at ambient conditions has gained attention. In general, these approaches involve surface modification to minimize the capillary forces and strengthening of the network to withstand the solvent

evaporation. During the chemical modification of the wet gel surface, the water-alcohol mixture within the pores is replaced by a water-free solvent, in the case of silica aerogels, this step is known as silylation. Then, a surface modifier is incorporated (e.g. chlorotrimethylsilane) to react with the Si-OH groups. Thus, the surface of the aerogels becomes hydrophobic. Later, a second solvent exchange takes place to finalize with the drying of the wet gel by evaporation of the solvent.

A variant of this method substitutes the solvent exchange using water glass as silica source and a silylation agent which in addition to modifying the surface, also reacts with the water present in the pores of the wet gel and thus, producing a surface tension drop suitable for ambient drying. Namely, in the first step, the wet gel is soaked into a mixture of hexamethyldisiloxane (HMDSO) and trimethylchlorosilane (TMCS). TMCS reacts with the OH- groups on the surface of the network to exchange the OH- groups by methyl groups ($-CH_3$). Then, TMCS reacts with the water at the HMDSO-H_2O interface to form HCl, which is at the same time, expelled along with the water. The wet gel is finally subcritically dried at ambient conditions [38].

2.4. Aerogel applications

Being widely studied, researchers have found plenty of applications for aerogels in multidisciplinary fields. Aerogels are not only the best solid thermal insulator ever produced but also, have the lowest sound propagation in solid material and the lowest dielectric constant. As can be seen, due to the enormous surface area, low density and low thermal conductivity, endless applications are possible. Nevertheless, the aerogels suffer from critical drawbacks when applied on industrial devices due to the weakness of the material to resist dynamic environments, the instability under certain working conditions (e.g., wetting, thermal shrinkage at high temperature, etc.), and for coatings approach, the deposition method, coating thickness, and lifetime. Some of the current applications of aerogels are described regarding their properties as shown in **Table 2.2.** Despite challenges for aerogels' applications, currently there are some companies focused on aerogels' commercialization. For instance the Swedish company Svenska Aerogel [39] developed the so-called material Quartzene® which is a versatile aerogel composite that can be used in paints for thermal insulation in buildings, air filtration and to enhance common thermal insulation materials

such as mineral wool, paper, cement, etc. In the past years, Cabot [40] has produced several aerogel products like light-diffusion panels with high thermal insulation capabilities, thermal insulating paints, and blankets, etc. Another leading company is Aspen Aerogels [41] a which industrialized several aerogel-based products for thermal protection at high and low temperatures such as insulation of pipelines, buildings, production spaces, etc. Aerogels are also used in clothing technologies [42].

Table 2.2. Existing and potential applications of aerogels. The table was adapted from [8,9].

Application	*Types of aerogels involved*	*Decisive aerogel properties*
Thermal insulation: monoliths, blankets, and panels for insulation of buildings, pipelines, packaging, winter apparel products, textiles	Silica, polyurethane, biopolymers (cellulose, alginate, pectin), carbon aerogels Composites: interpenetrated aerogel networks, granulate + aerogel network, nonporous material + aerogel granulate; textile + aerogel granulate; clay-containing aerogels	Thermal conductivity: main importance to the homogeneity of the pore size distribution to ensure Knudsen diffusion, macropores should be avoided; high mechanical stability; hydrophobicity
Drug delivery	Native silica; biopolymers: alginate, pectin, starch, chitosan, cellulose, and hybrids thereof	High surface area, accessibility of the pores for the drugs, affinity to specific drugs (surface modification may be needed)
Tissue engineering	Alginate, pectin, starch, chitosan, cellulose, and hybrids thereof	Combination of meso- and macroporosity in the same material, biocompatibility
Medical implants	Polyurea crosslinked aerogels, alginate, gellan gum, hybrids with gelatin	Pore structure suitable to applications (usually micropores to be avoided), biocompatibility, stability in liquids, biodegradability
Cosmetics	Silica particles	Amorphous aerogel backbone, potential adsorb liquid, flowability
Catalysts and carrier materials for catalysis and electrocatalysis	SiO_2, various metal oxides (TiO_2, Al_2O_3, CuO-CoO-MnO/SiO_2, Fe_2O_3, ZrO_2), graphene oxide, Ru/graphene, gold, chalcogenides and their mixtures, carbon (fuel cells), polysaccharides, (chitosan, alginate), noble metals and bimetals, Pt-Ni, hybrids of metal and semiconductor nanoparticles, photovoltaics	High surface area, stability in corresponding gaseous or liquid phases, transport through large meso- and macropores
Biocatalysis	Silica	Compatibility with enzymes, absence of toxic gelation by-products, pore sizes adjusted to the molecular size of the reaction products/adducts
Energy/hydrogen storage devices	Carbon, graphene-oxide	Large surface area, electrical conductivity

Sorbents for liquids, water treatment	Carbon, graphene-oxide, combinations thereof, including those with functionalized pores; functionalized/hydrophobized silica aerogels; magnetic cellulose aerogel, titania, clay aerogels	Surface functionalization to ensure selectivity to target molecules, open porosity, hydrophobicity, oleophobicity
Sorbent for gases	Silica, amino-modified silica, carbon, graphene-oxide, combinations thereof including functionalization (e.g., N- doping)	Surface functionalization to ensure the selectivity to target molecules, open porosity
Cherenkov detectors	Silica	Refractive index
Ballistic protection	Crosslinked silica aerogels	Mechanical strength

2.4.1. Applications of aerogel coatings

Most of the properties that are characteristic for bulk aerogels are also exhibited in other forms of the material, e.g., in thin sheets or films. A growing number of important applications require the aerogels either as freestanding sheets or as thin layers on substrate materials and most of the coated solid surfaces are glasses.

Optical. Thick aerogel coatings fabricated (≈ 2 μm) to act as coverslips on solar cells. The aerogel coatings are fabricated separately out the substrate and then bonded to the surface instead of being cast directly on it. In this case, the low refractive index of aerogels causes less reflective Fresnel loss for incident light than dense silica glass. This property allows the pass of light to the surface thus increasing the cell efficiency. Thin coatings (≈ 30μm) are deposited as a covering on the outer part of laser pump tubes. The aerogel minimizes the reflection of internally generated light at the outer envelope of the tube and increases the amount of excitation light reaching the lasing medium.

Acoustic. Thick aerogel films (≈ 0.5 μm) are formed on the surface of ceramic transducers to serve as acoustic impedance matching layers. Sending and receiving airborne acoustic waves is substantially increased by using aerogels in this application.

Electronic. Thin aerogel films (≈ 2 μm) are formed on silicon wafers to provide a low dielectric constant (ε) substrate in integrated circuits. The ε for aerogels is less than 2.0 and its value depends on the porosity which is controllable in aerogel films. Dielectric constants of the aerogels below 2 will enable a significant improvement in the speed of integrated circuits.

Thermal. Thin aerogel films (≈ 25 μm) have been formed on glass substrates for use in 'cool' infrared (IR) detectors. Here, the aerogel film serves as a thermal barrier to shield the IR detector elements from the heat radiated by the substrate materials. Many thick sheets (≈ 1 mm) of aerogel are coated with thin layers of metal, then laminated together to form a super-insulating thermal heat shield block. Aerogel, sheets are used in different industrial applications such as pipes, buildings, etc.

2.4.2. Applications of aerogels as coating thermal insulators

Low thermal conductivity aerogels (0.01 – 0.02 W m^{-1} K^{-1}) are potential candidates for thermal insulation applications such as clothes, buildings, industrial pipes, etc. [43–46] Aerogels can be used as translucent spacers in windows for daylight applications [47] or as building insulation since a transparent aerogel allows sun radiation penetration to the walls thus heating up the building, but due to its low thermal conductivity the generated heat remains [48,49]. Another field for aerogels thermal applications is in the form of a porous film as dielectric materials, reflective and anti-reflective coatings, flat panel displays, sensors, catalyst supports, and more recently as interlayer insulation in microelectromechanical system (MEMS) [50–52].

2.4.2.1. Thermal barrier coatings (TBCs)

Taking advantage of the best characteristics of the aerogels such as low thermal conductivity and low density, new applications have emerged over the years. One of them is as a precursor material for the improvement of thermal barrier coatings (TBCs) for aerospace industry [4,5,53]. A TBC (**Fig. 2.8**) is a multilayered system intended to protect important engine parts from damage due to extremely harsh working conditions [54]. In this multilayered system, one of the aims of the ceramic top coat is to protect the turbine components by reducing the substrate temperature. Due to the noteworthy of the ceramic top coat, among others, it must accomplish low thermal conductivity to achieve higher thermal gradient between the front and rear parts as well as phase stability at working temperature.

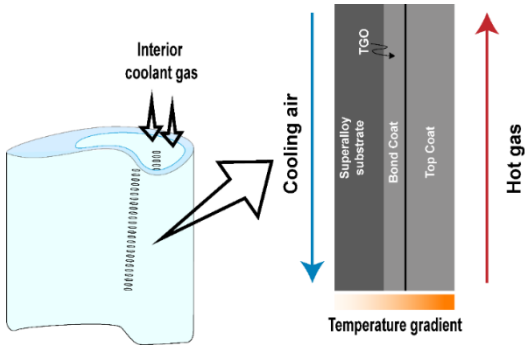

Fig. 2.8. Turbine blade with internal cooling channels and schematic representation of the thermal barrier coating and temperature gradient.

The low thermal conductivity of aerogels makes them good candidates to enhance the thermal properties of the TBCs top coat. Few studies have been published attempting to apply the aerogels in a TBC system. For instance, Fenech *et.al.* [55] compared the properties three YSZ materials (i.e. aerogel, xerogel, and commercial powder (16 mol%)) deposited by slurry dip coating on metallic substrates. When aerogel is used as precursor, coatings up to 90 μm were obtained with t-ZrO_2 phase whereas the commercial YSZ lead to c-ZrO_2. Other authors [4] prepared TBCs by slurry dipping into a YSZ slurry composed of 40% wt. aerogel powder. Such powder was previously crystallized into t-ZrO_2. They studied various process parameters (e.g., pre-oxidation of the bond coat, consolidation temperature, etc.) to control the appearance of cracks. The best performance under cycling oxidation tests was obtained for pre-oxidized samples and spray drying was used to reinforce the sol-gel top coat.

2.4.2.2. Yttria-stabilized zirconia

Among several types of ceramic top coats for TBCs, the 6-8 wt.% Y_2O_3 stabilized ZrO_2 (8YSZ or simply YSZ) it is the most widely used because it gathers most of the aforementioned requirements and can be deposited relatively easy either by air plasma spray (APS) or electron beam physical vapor deposition (EB-PVD) techniques [56,57]. However, beyond 1200 °C, the YSZ undergoes a phase transition from non-transformable tetragonal (metastable) zirconia (t'-ZrO_2) to tetragonal (t-ZrO_2) and cubic phase (c-ZrO_2), which upon quenching, the t-ZrO_2 further transforms into monoclinic (m-ZrO_2) phase. Especially the m-ZrO_2 to the t-ZrO_2 phase transition is accompanied by an increase of 4 % volume which induces irreversible damage of the coating [58]. Furthermore, the material suffers from microstructural changes, which led to a decrease in its mechanical properties [59].

Some studies of YSZ aerogels had been carried out. The first report on YSZ aerogels comes from Chervin *et.al.* [60] who prepared a 9 mol %YSZ aerogel by an epoxide-assisted sol-gel method and dried at supercritical conditions. This YSZ aerogel was of a mixture of c-ZrO_2/t-ZrO_2 stable from room temperature up to 1000 °C. The surface area of the as-obtained material was 406 m^2 g^{-1} and dropped to 159 and 26 m^2 g^{-1} upon calcination at 550 and 1000 °C, respectively. The same research group studied the effect of different cyclic ether compounds, solvent, and drying method of YSZ aerogels and xerogels. The Y_2O_3 composition was varied from 3 - 25 mol %. Before calcination, the surface areas of the aerogels were higher with the addition of propylene oxide (453 m^2 g^{-1}) than trimethylene oxide (up to 295 m^2 g^{-1}). After calcination at 550 °C, the surface area values were comparable (123 and 113 m^2 g^{-1} for propylene oxide and trimethylene oxide, respectively) [61]. Zhang *et.al.* produced YSZ aerogels by citric acid assisted sol-gel method. Their procedure yields single-phase t-ZrO_2 aerogels up to 1000 °C with surface area of 490, 315, and 63 m^2 g^{-1} for the as-obtained, and calcined at 400 and 1000 °C, respectively.

2.4.2.3. New materials as TBC precursor

Higher performance and durability requirements of gas-turbine engines will require a new generation of thermal barrier coatings. Many new TBCs materials have been proposed to achieve low thermal conductivity, high-temperature capability and higher thermal stability of the coating systems. Since TBCs operate under high-temperature and harsh conditions, factors such as the low thermal conductivity and the thermal expansion coefficient must be taken into account while exploring for new TBC materials composition. Thus, recent research efforts are focused on two main approaches: alternative materials and alternative stabilizers to the commonly used materials.

2.4.2.4. Perovskites

The most attractive feature of this type of material is its stability at high temperatures. The widely studied systems $BaZrO_3$ and $SrZrO_3$ have high melting points of 2690 and 2800 °C respectively. However, $BaZrO_3$ has poor thermal stability upon thermal cycling tests [62,63]. In contrast, the $SrZrO_3$ demonstrate better thermal stability during cycling test over 1250 °C. The drawback of this material is that it undergoes an orthorhombic to pseudo-tetragonal phase transition at ~ 730 °C which can be suppressed by the incorporation

of additional elements (e.g. Gd and Yb) [64,65]. On the other hand, the other type of perovskites with elevated melting point (3100 °C), low thermal conductivity and a complex composition such as $Ba(Mg_{0.3}Ta_{0.6})O_3$ (BMT) and $La(Al_{0.25}Mg_{0.5}T_{0.25})0_3$ (LAMT) are of research interest. However, during deposition (APS) a nonstoichiometric phase can be formed. Some studies indicate that the phase transition can be avoided if the residence time of the particles in the plasma plume is reduced [66,67].

2.4.2.5. Doping YSZ system with rare earths

The YSZ-M_xO group is based on conventional YSZ by adding another rare earth oxide to enhance its phase stability and further reduce the thermal conductivity. For instance, Ibegazene *et.al.* [68] found that 4.53 mol% Y_2O_3 and HfO_2 co-doped ZrO_2 exhibit non-transformable t-ZrO_2 phase without evidence of secondary phases. Other reports have shown that the addition of Sc_2O_3 stabilizes t-ZrO_2 up to 1400 °C[69]. It has been proved that co-doping the YSZ structure with different tri, tetra, and pentavalent elements (e.g. Gd_2O_3, Nd_2O_3, Eu_2O_3, etc.) enhance the phase stability of the system [68].

2.4.2.6. Rare-earth zirconates

Rare-earth zirconates ($Ln_2Zr_2O_7$; Ln is a trivalent rare-earth or lanthanide element Ln^{3+}) with pyrochlore and defect fluorite structures have attracted significant attention for high-temperature applications (>1200 °C) due to demonstrate low thermal conductivity, improved thermal stability until their melting point, good corrosion resistance, and low sintering behavior [70–73]. In this context, rare-earth zirconates exhibit lower thermal conductivities than the commonly used YSZ coatings, such as ~1.6 W m^{-1} K^{-1} at 700 °C in comparison with ~2.5 W m^{-1} K^{-1} of 9YSZ. Disordered fluorite (F) and ordered pyrochlore (P) $A_2B_2O_7$ which is a fluorite superstructure, are characteristic of this type of material [74]. The existence of either these structures is function of intrinsic factors (e.g. chemical composition, cations size ratio R_A^{3+}/R_B^{4+}, bonding character) and external factors (calcination procedure, synthetic conditions, etc.). Pyrochlore formation is favored when $R_A^{3+}/R_B^{4+} \geq 1.46$ and fluorite usually results when $R_A^{3+}/R_B^{4+}<1.46$ [75]. Moreover, the F ↔ P phase transition occurs at quite elevated temperatures (e.g. $Nd_2Zr_2O_7$ undergoes a transition at 2300 °C; $Gd_2Zr_2O_7$ undergoes a transition at 1500 °C), which is a higher than the YSZ system (1200 °C) that render them for TBCs applications.

2.4.3. Aerogel coatings deposition methodologies

Currently, most of the aerogel coatings are prepared by sol-gel approaches. Producing coatings by this methodology presents advantages such as high-purity, low-temperature deposition, cost-effectiveness, and the possibility of coating different substrate materials on complex geometries. To prepare aerogel films for any of the aforementioned applications, certain experimental details should be considered. Due to the exposed area is large, solvent evaporation is faster than in its monolithic counterpart. To decelerate the evaporation rate, the coating is cast in a controlled atmosphere chamber saturated with the precursor solvent. Another consideration is the surface treatment prior deposition due to any impurity decrease the gel adhesion. The next subsections summarize the most employed methods to deposit the aerogels on bulk substrates.

2.4.3.1. Dip-coating

In this method, the substrates are dipped into a precursor solution and then withdrawal it from the sol. A wet film is formed from the liquid upward along with the moving substrate. This process involves a complex interplay between many factors: solution (or in this case sol) viscosity, gravity force acting on the wet film, surface tension gradient, and drying effects. When the produced film is intended to transform into an aerogel, the substrate must be immediately placed into a saturated atmosphere to avoid rapid evaporation of the solvent, which results in a cracked xerogel. The main considerations of this technique are: 1) low thickness, which is usually improved by the use of solutions with greater viscosity, 2) the gelation times are shorter in comparison with bulk gels due to rapid evaporation, 3) the coated surfaces are flat since roughness can cause stresses and subsequent cracking, 4) the coated surface is immediately immersed in the aging solution until supercritical drying. A schematic representation is shown in **Fig. 2.9**.

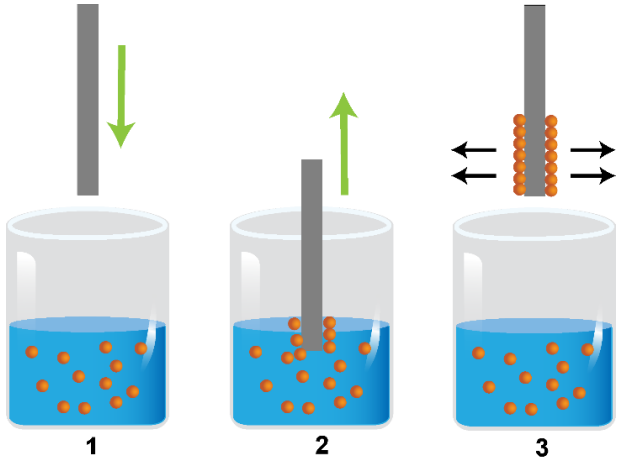

Fig. 2.9. Dip-coating process. 1) dipping, 2) wet coating formation, and 3) solvent evaporation.

Exist a variant of the dip-coating method, which substitutes the sol by a slurry. In this technique, the early drying of the deposited layer is avoided while the number of depositions and the powder loading of the slurry control the thickness. In the case of aerogels, the liquid phase of the slurry is the original sol (which also acts as a binder) with the same composition used for the aerogel preparation while the solid phase is the ground aerogel. In this case, the sol plays an important role as a binder between the dispersed powder, making it less likely that the coating will crack during the processing. Moreover, due to the amount of powder, the amount of wet gel is minimum and less shrinkage occurs during the drying step. For the deposition of aerogels by the sol-gel slurry approach, is necessary to consider important factors: dispersion and stability of the slurry, gelation time, and powder granulometry. Specifically, the addition of interacting components (e.g., aerogel powder) directly affects the stability of the sol [3]. This approach has been used to study the enhancement TBC by aerogel precursor. For instance, Fenech *et.al.* [55] compared to the deposition of three YSZ powders in the form of a commercial powder, xerogel, and aerogel. They found that commercial YSZ powder is mainly constituted by cubic phase, while the aerogel-based samples were found stable tetragonal. Both after 950 °C / 2hrs. Touzing *et.al.* [76] prepared a slurry of Al_2O_3 powder in a SiO_2 sol and studied the different deposition parameters such as sol composition, particle size, and heat treatment. They conclude that crack-free coatings of 50 μm thickness can be obtained when larger particles are used to produce the slurry (1-3 μm). In addition, they stated that the silica sol enhanced enormously the cohesion particle-to-particle and to the substrate.

2.4.3.2. Spin-coating

The spin coating deposition methodology is divided into four main stages: deposition, spin-up, spin-off, and evaporation (**Fig. 2.10**). In the deposition stage, a droplet is dispensed on the surface. During the spin-up step, the substrate holder is turned at controlled revolutions per minute (rpm) and the liquid flows radially outward, driven by centrifugal force. In the spin-off, the excess of liquid is ejected as a drop on the perimeter of the surface. In the last stage, evaporation takes over as primary mechanism of thinning, although evaporation is present in all the stages. In fact, for aerogel coatings preparation, all these stages must be carried out under alcohol saturated atmosphere. The main features of the spin coating are high homogeneity of the deposited layer, thickness lower than two micrometers, as, in the dip-coating method, the gelation time is shortened.

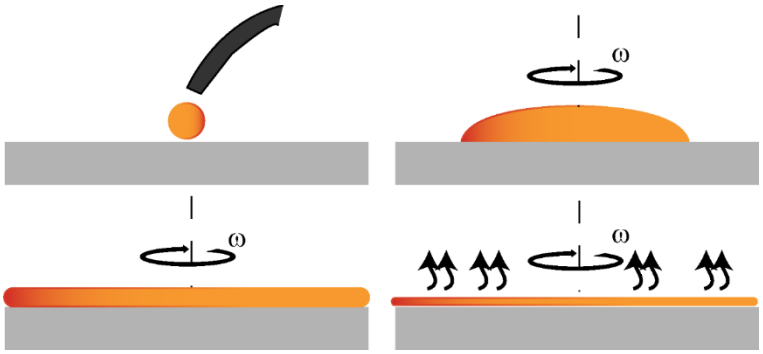

Fig. 2.10. Spin-coating process.

2.4.3.3. Surface tension coating

In this coating method, surface tension is used to draw the liquid onto the solid surfaces. A feature is made by forming a space between the substrate to be coated and another flat surface (treated to prevent bonding to the gel so that it should be removable after drying process). The liquid precursor fills the available volume by capillarity when the element is dipped into the solution. The spacers are used to separate the substrates by the desired film thickness. Common film thicknesses are in the range from 2 up to 50 μm.

2.4.3.4. Doctor-blade coating

Doctor-blade coating and its variants such as bar coating are methods designed for large-scale production. A typical deposition process consists of three main steps: (i) solution deposition onto the surface of the substrate, (ii) moving the coating tool to spread the solution and (iii) drying of the deposited coating. The most important parameters of this method are solution or suspension composition, distance of the coating tool to the substrate, and in some cases the surface temperature. Thin coatings are produced by this method (below 5 μm). Only a few publications exist producing aerogels by this method. In one of these works [77] was developed a doctor-blade method to deposit ambient-dried SiO_2 aerogel films with controlled porosity. Namely, they studied the effect of synthesis parameters (i.e. aging time, reagent concentration, etc.) in the porosity of the coatings onto fluorine-doped tin oxide (FTO). Authors found that long aging periods are needed (> 8 hrs.) to obtain high-quality coatings of 2 - 3.6 μm, with surface areas up to 530 $m^2 g^{-1}$. In another study [78], SiO_2-TiO_2 hybrid aerogels were tested as photoanodes and deposited by a doctor-blade method using an aerogel slurry. The thickness of the coating was ~10 μm. A similar procedure was employed by Pietron *et.al.* [79]. They reported the preparation of TiO_2-based aerogel coatings onto FTO substrates by spreading an aerogel slurry into a cavity formed by 60 μm thick adhesive tape. The final coatings were produced of 10 - 40 μm thick.

Aims of the doctoral thesis

The overall aim of this thesis is to carry out a systematic investigation on the synthesis and processing of advance thermal-stable aerogels for high-temperature applications. Four new aerogel materials have been selected in the form $Ln_2Zr_2O_7$ (Ln=La^{3+}, Nd^{3+}, Gd^{3+}, Dy^{3+}), along with ZrO_2 and YSZ. This work includes a study of the preparation of xerogels, aerogels, and aerogel-based coatings produced by different soft chemistry methodologies to identify the best processing routes to be applied as precursor material in future thermal barrier coatings applications. Secondary aims of the thesis are the following:

- Development of a versatile synthesis to prepare ZrO_2-based aerogels.
- Study the effect of temperature on ZrO_2 and ZrO_2-Y_2O_3 7% wt. YSZ aerogels.
- Perform a comparative study on the physicochemical properties of $Ln_2Zr_2O_7$ (Ln=La^{3+}, Nd^{3+}, Gd^{3+}, Dy^{3+}) aerogels, xerogels and powders upon heat treatment.
- Study the different deposition methodologies of aerogel coatings on metallic substrates with potential TBCs applications to be used in the future.

3. Methodology

3.1. Synthesis of aerogels

The synthesis of the studied materials is divided into three main categories: aerogels, xerogels, and powders. Aerogel coatings processing will be described later in this section. Namely, the preparation of aerogels by means of sol-gel method includes (1) wet gel synthesis, (2) aging, and (3) supercritical drying (SCD). The xerogels were prepared following similar procedure however, after the wet gel preparation, was directly dried at ambient conditions. Powders were prepared by the co-precipitation technique. The chemical reagents utilized in this research are listed in **Table 3.1**.

Table 3.1. Used reagents for the synthesis of all the studied systems.

Reactant	M (g mol^{-1})	ρ (g cm^{-3})	Purity (%)	Trade
Zirconium propoxide ($Zr(OPr)_4$)	327.57	1.044	70 % in 1-propanol	Sigma-Aldrich
1-Propanol ($C_3H_8O_7$)	60.10	0.804	99.7	Sigma-Aldrich
Acetyl acetone ($C_5H_8O_2$) (Acac)	100.12	0.97	99	Sigma-Aldrich
$La(NO_3)_3{\cdot}6H_2O$	432.92	N/A	96	Merck KGaA
$Nd(NO_3)_3{\cdot}6H_2O$	438.35	N/A	99.99	Alfa Aesar
$Gd(NO_3)_3{\cdot}6H_2O$	451.36	N/A	99.99	Sigma-Aldrich
$Dy(NO_3)_3{\cdot}xH_2O$	456.51	N/A	99.99	Sigma-Aldrich
$Y(NO_3)_3{\cdot}6H_2O$	383.01	N/A	99.98	Sigma-Aldrich
Polyethylene glycol	380-420	1.12	90	Sigma-Aldrich
Ammonia (NH_4OH)	35.05	0.9	28-30	Sigma-Aldrich
Nitric acid (HNO_3)	63.01	1.413	70	Sigma-Aldrich
H_2O	18.01	1	100	Distilled

The different synthetic protocols are summarized in **Scheme 3.1**.

Scheme 3.1. Synthetic procedures followed to obtain aerogels, xerogels, and powders.

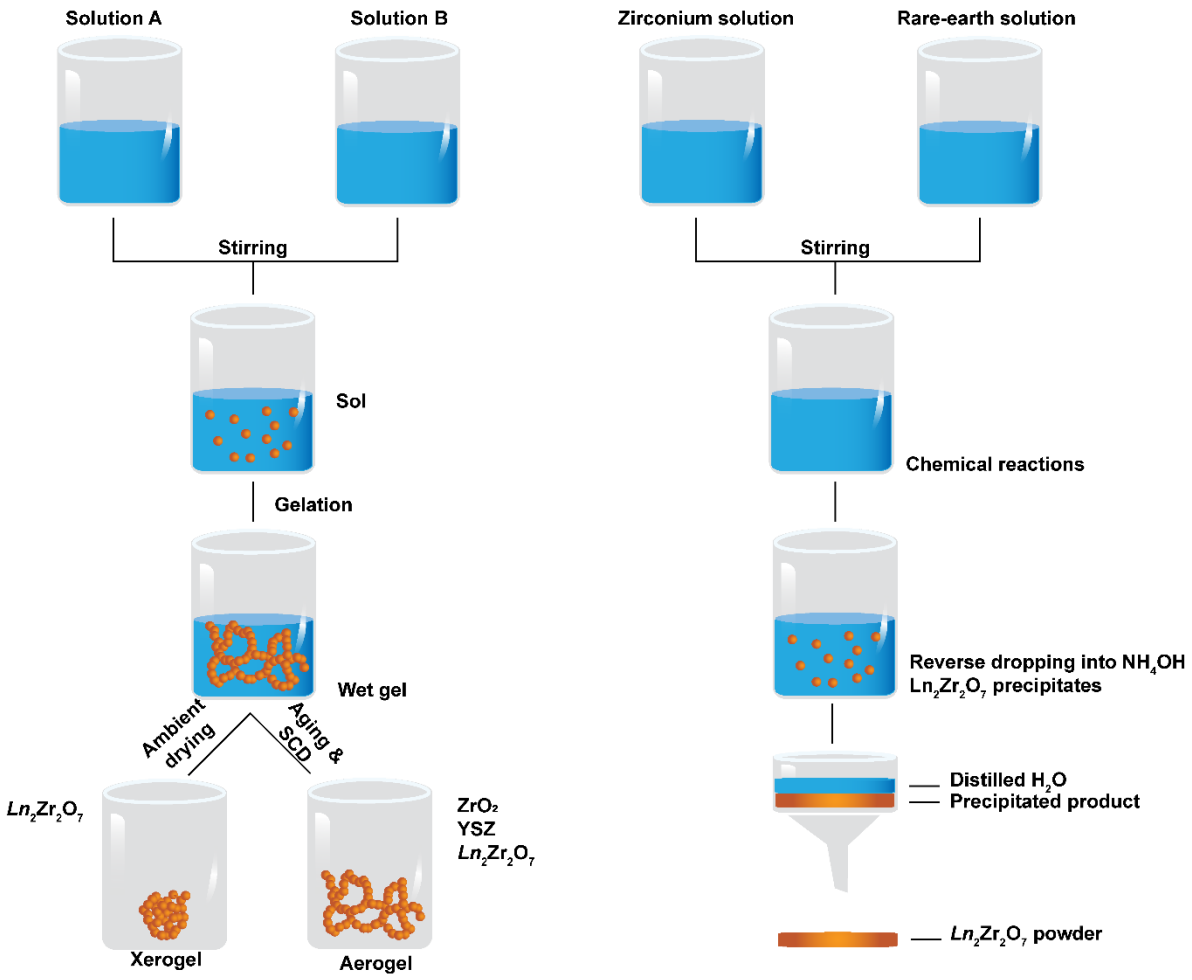

Following the above-depicted methodologies six aerogel materials were synthesized (ZrO_2, YSZ, and 4 lanthanide zirconates (LZ) $Ln_2Zr_2O_7$, *Ln* = La, Nd, Gd, and Dy). To compare the physicochemical properties of the LZ aerogels, $Ln_2Zr_2O_7$, xerogels, and powders were also synthesized.

In **Table 3.2** are displayed the different synthesized materials along with their respective calcination process and sample denomination.

Table 3.2. Summary of the prepared materials and their heat treatment procedures.

Sample	Denomination	Heat treatment #1			Heat treatment #2			Heat treatment #3		
		T_1 (°C)	R_1 (°C/min)	D_1 (h)	T_2 (°C)	R_2 (°C/min)	D_2 (h)	T_3 (°C)	R_3 (°C/min)	D_3 (h)
ZrO_2 aerogel	ZrO_2-AO**	300	3	12	500	10	2	1200	10	2
YSZ aerogel	YSZ-AO**	300	3	12	500	10	2	1200	10	2
***Ln*$_2$Zr$_2$O$_7$ powders**	LnZP* LZP NZP GZP DZP	120	3.3	12	1000	3.3	5	---	---	---
***Ln*$_2$Zr$_2$O$_7$ Xerogels**	LnZX* LZX NZX GZX DZX	120	3.3	12	1000	3.3	5	---	---	---
***Ln*$_2$Zr$_2$O$_7$ aerogels**	LnZA* LZA NZA GZA DZA	120	3.3	12	1000	3.3	5	---	---	---

T: temperature setpoint; R: used heating ramp; D: dwell time.

* *Ln* = La^{3+}, Nd^{3+}, Gd^{3+}, Dy^{3+}. The denomination was set with L for lanthanum, N for neodymium, G for gadolinium, and D for dysprosium; P for powders, X for xerogels, and A for aerogels (i.e. LnZA, and NZA corresponds to lanthanide zirconate aerogels, and Neodymium zirconate aerogel, respectively).

** The –AO stands for as-obtained samples.

ZrO_2 wet gel preparation. The ZrO_2 wet gels were prepared in the following 4 steps: i) 1M HNO_3 in 1-propanol solution was prepared (catalyst solution); ii) in a separate beaker, 1-propanol was mixed with the catalyst solution, then zirconium(IV) propoxide was slowly added under continuous stirring (solution A); iii) a third solution was prepared from distilled water and 1-propanol (solution B) and iv) solution B was slowly added to solution A and stirred vigorously with a magnetic stir bar for 5 min. The final molar ratio of $Zr(OPr)_4$, 1-PrOH, HNO_3, and H_2O was 1 : 150 : 2 : 3. The as-prepared sol was poured into a beaker and kept hermetically sealed until a rigid wet gel was formed. The final samples were denominated as listed in **Table 3.2**.

YSZ wet gel preparation. For the preparation of the YSZ gels, the composition and procedure to obtain ZrO_2 gels were replicated. However, yttrium(III) nitrate was initially dissolved in the solution A. In the case of the YSZ gels, the final molar ratio of $Zr(OPr)_4$, 1-PrOH, HNO_3, H_2O, and $Y(NO_3)_3$ were 1 : 150 : 2 : 3 : 0.14. Thus, the YSZ aerogel nominally consisted of 7 mol% of yttrium. The as-prepared sol was poured into a beaker and kept hermetically sealed until a rigid wet gel was formed. The final samples were denominated as listed in **Table 3.2**.

***Ln*$_2$Zr$_2$O$_7$ (*Ln*$^{3+}$ = La^{3+}, Nd^{3+}, Gd^{3+}, Dy^{3+}) wet gels preparation**. Initially, a solution containing 1-propanol and HNO_3 was prepared. Then $Ln(NO_3)_3 \cdot xH_2O$ (1.47, 1.50, 1.53 and 1.49 g for La, Nd, Gd, and Dy, respectively) was added under mild stirring to form a transparent solution. Zirconium(IV) propoxide was slowly added in order to avoid any undesired precipitation. The molar ratio of Ln^{3+}:Zr^{4+} ratio was kept constant at 1 : 1. The as-prepared sol was poured into a beaker and kept hermetically sealed until a rigid wet gel was formed. The synthesized wet gels were either supercritically dried (aerogels) or ambient dried (xerogels), see **Scheme 3.1**. Both aerogels and xerogels were calcined at 1000 °C for 5 hrs. The final samples were denominated as listed in **Table 3.2**.

Rare-earth zirconate (*Ln*$_2$Zr$_2$O$_7$; *Ln*$^{3+}$ = La^{3+}, Nd^{3+}, Dy^{3+}, or Gd^{3+}) powders. These materials were prepared by the co-precipitation technique. In particular, $Ln(NO_3)_3 \cdot xH_2O$ and zirconium(IV) oxychloride ($ZrOCl_2 \cdot xH_2O$) were used as the precursor materials and dissolved separately in deionized water. The Zr^{4+}:Ln^{3+} ratio was 1 : 1 and the concentration of both solutions was of 1M. After the stirring for 30 min, the solutions were mixed together and stirred for 2 h. Aqueous ammonia (24 %) was added dropwise to raise the pH up to 11. The rate of dropping was about 30 drops min^{-1}. The pH value was monitored continuously with a digital pH meter (VWR pHenomenal® 1100L; glass pH electrode with a built-in 221 temperature sensor). As a result, the gel-like precipitate was formed in all 4 systems, respectively, and was subsequently filtered off and washed twice with deionized water. Wet gels were dried at 120 °C for 12 h (see **Scheme 3.1**). To obtain dry powders the calcination was carried out at 1000 °C in air for 5 hrs. The final samples were denominated as listed in **Table 3.2**.

3.1.1. Aging of wet gels

Prior to the supercritical drying process, the aging step was performed to all the wet gels intended to transforms into an aerogel (ZrO_2, YSZ, and $Ln_2Zr_2O_7$) as follows: the aged gels were placed and soaked in a freshly prepared mixture of 1-PrOH and acetone, the mixture was changed every 24 hrs. For each cycle, the concentration of acetone was increased until pure acetone completely replaced the initial solvent (namely, 1-propanol : acetone; 100 : 0, 75 : 25, 50 : 50, 25 : 75, 0 : 100). This solvent exchange process washed out any leftover of the reagents and the byproducts.

3.1.2. Supercritical drying of wet gels

After the aging of the wet gels, in order to obtain the aerogels, the wet gels were supercritically dried using liquid CO_2. In a typical drying procedure, the aged wet gels were placed in an autoclave (see **Fig. 3.1**) and covered with fresh acetone. Followed this, the autoclave was sealed and liquid CO_2 was flushed into the device until the equilibrium conditions were reached (20 °C; ~56 bars). Then, the drain valve at the bottom of the autoclave was slightly open to allow the acetone flow out and parallel the liquid CO_2 diffuses into the wet gel pores displacing the solvent. This step took several hours to days. After complete replacement of acetone, all the valves were closed and the temperature was elevated up to 45 °C in a period of approx. 1 hour which produced a substantial increase in the pressure (~100 bar). These conditions were kept constant for next 3 hours. Then, the system was depressurized at an approximate rate of ~ 2 bar/min until room temperature and atmospheric pressure conditions.

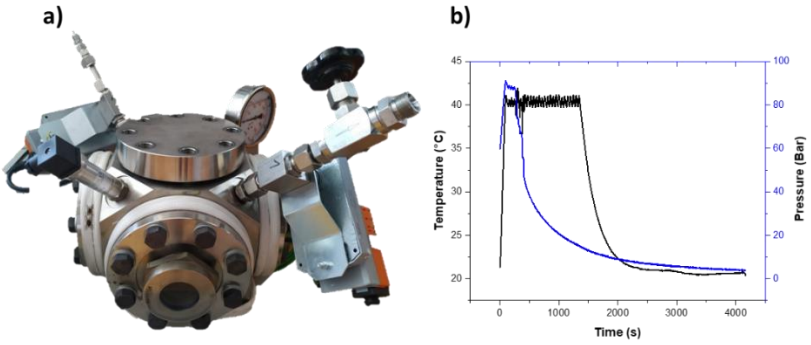

Fig. 3.1. The supercritical drying was performed in a 3L high-pressure autoclave; a) Photography of the supercritical drying device used to obtain the aerogel samples: b) typical supercritical drying plots recorded during an experiment.

3.2. Deposition of aerogel coatings

Coatings were prepared on two different metallic substrates : 20x20x5 mm 99.5 Al, and Ø 10 mm cylindrical and 10 mm in thickness Ni-based MAR-M-247 alloy. To enhance surface coarsening, prior deposition, the substrates were grit blasted using Al_2O_3 particles with the aim to increase the surface roughness and improve the coating adhesion. Then, surface treated substrates were ultrasonically cleaned in acetone for 30 minutes and dried by a flow of nitrogen. Different coating deposition methods were investigated in detail (**Fig. 3.2**).

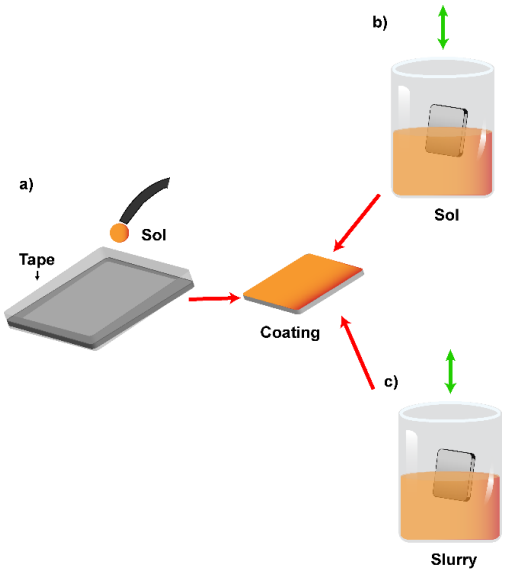

Fig. 3.2. Different employed deposition methods; a) doctor blade casting; b) dip-coating into a precursor sol, the sol further turned a wet gel layer which was dried under supercritical conditions; c) dip-coating into a slurry composed of aerogel as dispersed powder and the original sol as liquid media.

3.2.1. Doctor-blade method

In this process, the substrate was surrounded by tape as shown in **Fig. 3.2a**. Then, a YSZ sol was deposited onto the substrate surface prior the sol became a wet gel. Then the substrates with deposited gel were aged and subsequently supercritically dried to observe the transformation from gel to an aerogel directly on the surface of the substrate. For these experiments, the only variable was the amount of liquid poured on the surface to study the effect of the supercritical drying conditions as the thickness of the aerogel coating increases.

3.2.2. Dip-coating method

In the second approach, a typical dip-coating process was followed (**Fig. 3.2b**). First, a YSZ sol was prepared and poured into a vessel. Then, prior gelation, the metallic substrate was drowned and withdrawal to produce the desired layer. Finally, the coating was aged and dried under supercritical conditions of CO_2. For these experiments, the effect of the viscosity (viscosity increase proportionally with the time) was investigated.

3.2.3. Slurry dip-coating

Similar to the dip-coating experiments described above, the dip-coating technique was used to produce the aerogel coatings, however, in this case, was dipping the metallic substrate into slurry composed of aerogel powder and the original sol used to produce the aerogel powder. The detailed process of coating deposition is described in the following section.

3.2.3.1. Aerogel slurry powder preparation

To process the slurry coatings, the first step was the formation of a stable slurry composed of the initial sol ($La_2Zr_2O_7$) loaded with different amounts of $La_2Zr_2O_7$ aerogel powder. Thus, a new $La_2Zr_2O_7$ sol was prepared as described above (**section 2.1)** keeping the molar ratio of Zr^{4+} : Ln^{3+} 1 : 1 but only with larger amount of nitric acid (additional 2 mL) was used to avoid the sol turns to a wet gel and to disperse the aerogel powder. Once the sol was synthesized, different amounts of aerogel powder were added under continuous stirring. The amount of aerogel powder loaded into the sol was varied from 10 to 30 wt.% of the total solution. The stirring was kept overnight to assure complete powder dispersion. Coatings were obtained when dipping the substrates into the slurry. The number of dips varied from 1 to 3. After each dip, the coated substrate was heated at 50 °C / for 1 min to evaporate the excess of organic compounds. In the end, the coatings were heat-treated at various temperatures (from 600 up to 1000 °C) for 30 min in air with a ramp of 1 °C / min to consolidate the deposited layer. **Fig. 3.3** illustrates the coatings process preparation.

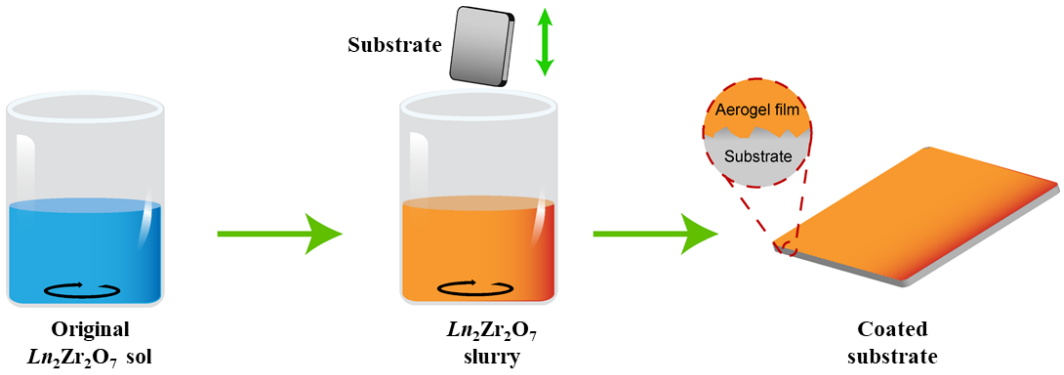

Fig. 3.3. Deposition process of the aerogel coatings; a) prepared sol as liquid continuous phase in the slurry; b) dispersion of the calcined aerogel powder into the sol to form a stable slurry; c) deposited layer onto the substrate.

3.3. Characterization

3.3.1. Microstructural study

To investigate the surface morphology of the materials and coatings produced, a high-resolution scanning electron microscope (HR-SEM) 460L Verios (FEI, Czech Republic) was used. Prior SEM studies, the samples were prepared on a carbon tape followed by a deposition of a conducting thin carbon layer. In the case of the coatings, to observe the cross-section, the substrates were mounted into an electrically conductive resin and polished up to 3 μm diamond paste prior the observation.

3.3.2. Calorimetry

Differential Scanning Calorimetry is a tool to understand the thermodynamic phenomena (i.e. crystallization, phase-transition, etc.) taking place at determined temperature range and how this affects the materials' behavior. Thermogravimetric analysis is a technique for continuous monitoring of the mass changes of a sample in function of the temperature or time. The mass spectrometry is analytical technique that determines the mass-to-charge ratio from a sample displayed in a spectrum that coupled with the aforementioned techniques gives a complete analysis of the thermodynamic phenomena and species driven directly from a sample. Thus, thermogravimetric analysis (TGA), differential scanning calorimetry (DSC) and coupled mass spectrometry (MS) were carried out simultaneously in a Netzsch STA 409c/CD apparatus. Analyses were performed with the as-obtained materials in synthetic air

atmosphere (14 %vol. of O_2 in Ar) using Al_2O_3 crucibles with a heating rate of 10 °C min^{-1} from 20 °C to 1300 °C. The MS signal of m/z: [H_2O] 18, [CO] 28, [CO_2] 44, [NO_x] 14, 30, and 46 were recorded.

3.3.3. Porosity

Nitrogen gas adsorption-desorption measurements are commonly used to determine the specific surface area as well as the pore size and distribution in aerogel materials. The measurements were performed in an Autosorb iQ (Quantachrome Instruments, Boynton Beach, FL, USA) sorption analyzer at 77.4 K. Prior standard measurements, the samples were degassed in vacuum at 180 °C for 12 hrs. The ASiQwin, version 4.0 (Quantachrome Instruments) was used for all calculations based on the obtained isotherms. Specific surface area (S_{BET}) was calculated by using the Brunauer-Emmett-Teller (BET) method [80] while the micropore volume and micropore area were calculated using the t-plots (De Boer) method [81], both from the adsorption isotherms. The pore size distribution of the samples was determined from the desorption isotherms using the Barrett-Joyner-Halenda (BJH) model [82].

3.3.4. Phase analysis

The phase composition and thermal stability of all the materials were substantial. Hence, the present crystalline phases were analyzed by X-ray diffraction (XRD). XRD patterns from all samples were recorded using an X-ray diffractometer (Rigaku, Japan) operating at the Bragg–Brentano geometry. A Cu-Kα radiation source (λ = 1.5406 Å) was used as the X-ray source. The operating voltage and current of the instrument were kept at 40 kV and 30 mA, respectively. The XRD patterns were collected from 10 to 90° or in some specific cases from 20 to 65°C with a step size of 0.02° and a scanning speed of 0.1° min^{-1}. To identify the systematic phase transition of ZrO_2 and YSZ samples, *in-situ* X-ray diffraction was performed. The samples were heated from 25 up to 1200 °C, each 100 °C a pattern was recorded from 22 to 37° with a step size of 0.02°. The scanning time was 5 min / step and was performed in duplicate. Data were processed using the HighScore+ software and ICDD PDF 2 and ICSD 2012 databases. Quantitative phase analysis was realized according to the Rietveld method using the fundamental parameter approach.

Crystallite size (D) was determined from the X-ray line broadening using Scherrer's equation (Eq. 3.1):

$$D = \frac{K\lambda}{\beta cos\theta} \qquad \textbf{(Eq. 3.1)}$$

where K is the shape factor (assumed spherical shapes; 0.89), λ is the X-ray wavelength (0.154 nm), β is the line broadening at half of the maximum intensity in radians (full width at half maximum: FWHM), and θ is the Bragg angle [83]. The FWHM values were determined by fitting the XRD pattern peaks. Additionally, Warren's correction (Eq. 3.2) was applied to determined FWHM:

$$\beta = \sqrt{(B^2 - b^2)} \qquad \textbf{(Eq. 3.2)}$$

where β is the FWHM after correction, B is the calculated FWHM and b is the FWHM of the fully crystalline LaB6 standard. When required, Rietveld refinement was performed by means of fitting the X-ray diffraction patterns using the commercially available peak fitting software HighScore+.

3.3.5. Spectroscopy

Raman spectroscopy is a technique that can be used to determine the present crystalline phases when XRD does not provide precise information. This issue occurs commonly in rare-earth zirconate materials where sometimes is difficult to discern from pyrochlore and fluorite crystalline phases. Thus, Raman spectroscopy was used to assign accurately the present crystalline phases in the bulk $Ln_2Zr_2O_7$ powders, xerogels, and aerogels. Therefore, non-polarized Raman spectra were acquired in backscattering geometry with a Horiba T64000 Raman spectrometer equipped with a triple monochromator in the subtractive configuration (spectral resolution of 0.6 cm^{-1}) coupled to a confocal microscope. A 488 nm line of a Coherent Innova Spectrum 70C Ar^+-Kr^+ laser was used as excitation source using a 20× objective with laser power on each sample of 5 mW. A liquid-nitrogen-cooled CCD (Jobin-Yvon Symphony) detector was used.

3.3.6. Furnace cycle oxidation test (FCT)

The $La_2Zr_2O_7$ coatings prepared by the slurry dip-coating were tested in the Rapid Temp Model 1612 BL laboratory box furnace with cycling package (CMfurnaces, USA). In a

typical experiment, the slurry coating samples were placed on the ceramic platform and subsequently heat-treated according to the plan of the experiment, which included the operating temperature, the duration of heat-treatment at operating temperature, the duration of subsequent fan cooling and the number of cycles to test. During FCT, the fan mounted in the side of the furnace cooled down the tested samples. The testing conditions of FCT included (i) the heating ramp of 77 °C/min to reach a working temperature of 1100 °C, (ii) 60 min dwell time at the temperature and followed by (iii) fan cooling of the samples for 15 min.

4. Results and discussion

For applications of aerogels in high-temperature coatings, the physicochemical properties of the aerogel to deposit are important, as it is the deposition methodology. Therefore, a complete assessment of six aerogels is discussed; namely, zirconia (ZrO_2), yttria-stabilized zirconia (YSZ), and rare earth zirconates $Ln_2Zr_2O_7$ (Ln = La^{3+}, Nd^{3+}, Gd^{3+}, and Dy^{3+}). In addition, the $Ln_2Zr_2O_7$ aerogel properties are compared with xerogels and powders with similar composition. Finally, a study of different deposition methods of aerogels was carried out.

4.1. ZrO_2 and YSZ aerogels: Synthesis and characterization

The development of a synthetic protocol to prepare ZrO_2 aerogels and that can be practical for other Zr-based aerogels was performed. The hydrolysis and condensation reactions of Zr-based aerogels employing zirconium propoxide is sensitive to the nature of the employed reactants. Most of the authors tackle this limitation by the use of an epoxide-assisted sol-gel method [84], while others use a non-alkoxide approach by means of more flexible reagents such as salts [85]. In this research work, a facile propoxide-based sol-gel synthesis without the use of additional reagents like epoxides was developed. To achieve this, several synthesis conditions and chemicals were assessed until a stable, and precipitation-free, wet gel was obtained suitable for supercritical drying in order to obtain successfully the aerogel material.

As stated in **Section 2.1**, the reactivity of some alkoxides such as $Zr(PrO)_4$ which has been used in this research, is quite high and therefore uncontrolled hydrolysis may occur. Thus, the first step to produce a Zr-based wet gel and subsequently an aerogel is the attenuation of the reactivity. In a first attempt to achieve this, different amounts of acetylacetone (Acac) were added to 1 mL of 1-propanol contained in a test tube and stirred for 1 minute. As the Acac dissolves, a transparent solution was obtained. Then, 1 mL of $Zr(OPr)_4$ was dropwise incorporated. In a separate test tube, 0.2 mL of distilled H_2O were mixed with 1 mL of 1-propanol. Finally, both solutions were mixed together under vigorous stirring. The results are summarized in **Table 4.1**. Samples with high volume of Acac (e.g. 0.8 and 1 mL) resulted in gelation after few seconds with visible precipitates. At such concentrations of Acac, hydrolysis reactions are suppressed and condensation reactions are

favored. Therefore, condensation is carried out more rapidly than hydrolysis, which results in the formation of a wet gel with partially hydrolyzed complexes and therefore precipitation forms. On the other hand, when the added amount of Acac was 0.4 mL, the hydrolysis reactions were favored and the sol was stable after several hours. Below 0.4 mL, a precipitated wet gel was formed.

In general, most of the experiments resulted in precipitated gels. This negative effect is derived from the quite high hydrolysis power of the zirconium precursor which immediately reacts with H_2O molecules [86,87]. This is an indication that the amount of Acac added is not adequate to reduce its reactivity.

Table 4.1. Synthesis conditions of the first Acac aerogel series.

Experiment	Zirconium propoxide $Zr(OPr)_4$	1-Propanol $C_3H_8O_7$	Acetyl acetone Acac	H_2O	Results
Z001	1 mL	1 mL	0.2 mL	0.2 mL	"Cloudy" gel with precipitate
Z002	1 mL	1 mL	0.4 mL	0.2 mL	Yellowish stable sol after 48 h (no gelation)
Z003	1 mL	1 mL	0.8 mL	0.2 mL	Instant gelation (precipitation)
Z004	1 mL	1 mL	1.0 mL	0.2 mL	Instant gelation (precipitation)

With the objective of decrease or eliminate the undesired precipitation, in the next series of experiments, the amount of Acac was decreased below 0.2 mL as is described in **Table 4.2**.

The decrease of the acetylacetone volume avoided the formation of precipitate. In addition, it derived into an absolute inhibition of the gelation after 48 h for all the compositions. Even when the water amount was significantly increased as in the experiment Z008, the gelation was suppressed. At the proposed conditions in **Table 4.2**, the Acac prevents uncontrolled progress of hydrolysis reactions and precipitation was avoided, however, it also stops condensation reactions, resulting in the stabilization of the sol without gel transformation.

Table 4.2. Synthesis conditions of the Acac aerogel series with lower acetylacetone volume

Experiment	Zirconium propoxide $Zr(OPr)_4$	1-Propanol $C_3H_8O_7$	Acetyl acetone Acac	H_2O	Results
Z005	1 mL	1 mL	0.005 mL	0.2 mL	Yellowish stable sol after 48 h (no gelation)
Z006	1 mL	1 mL	0.01 mL	0.2 mL	Yellowish stable sol after 48 h (no gelation)
Z007	1 mL	1 mL	0.15 mL	0.2 mL	Yellowish stable sol after 48 h (no gelation)
Z008*	1 mL	1 mL	0.2 mL	0.5 mL	Yellowish stable sol after 240 h (no gelation)

* Sample prepared with 1.5 times higher H_2O amount

When Acac was used as a stabilizer at volumes below 0.2 mL, precipitation does not occur, however, the gelation was completely inhibited. Thus, at the studied reaction conditions, the Acac was found as not suitable agent to obtain a gel for supercritical drying conditions. The nature of the stabilizer was changed and polyethylene glycol (PEG) substituted the Acac. For this purpose, two separated solutions were prepared. In the first one, 1 mL of 1-propanol mixed with different amounts of polyethylene glycol. After 5 minutes under vigorous stirring, 1 mL of zirconium propoxide was slowly added producing a white solution with no evident precipitation. A second solution was prepared by mixing a fixed amount of water (0.2 mL) with a second amount of 1-propanol (1 mL). Then, both solutions were mixed under vigorous stirring and the sol turned into transparent solution. All the prepared sols turned into a wet gel after certain time as shown in **Fig. 4.1**.

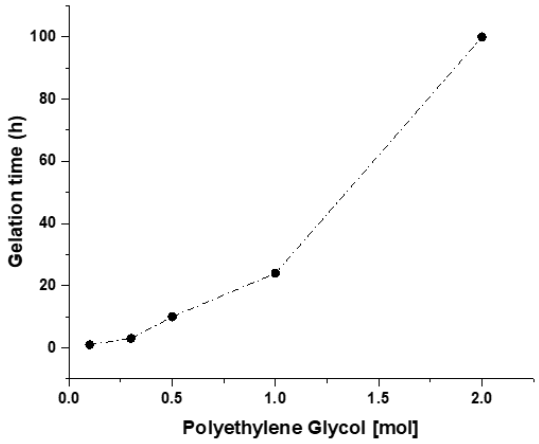

Fig. 4.1. Gelation time dependence as a function of PEG concentration.

Afterward, the produced gels were aged. During this procedure, the obtained wet gels were weak and some portion of the bulk was washed out. After the aging step, all the samples were dried under supercritical conditions of CO_2. Due to the weakness of the produced wet gels, the obtained aerogels were in powder shape. This result might be the effect of polyethylene glycol and, due to such additive, has double effect: attenuate the high reactivity of the $Zr(OPr)_4$ and as a surfactant. The first effect allows the progress of the hydrolysis and condensation reactions without formation of precipitates. However, the secondary effect is to create an impedance between the formed colloidal particles thus reducing their contact (**Fig. 4.2**). If the interaction between particles was highly reduced as in this case (increased gelation time proportionally to the amount of polyethylene glycol, **Fig. 4.1**). The resulting 3D network was built by smaller aggregates which resulted in a weak aerogel prone to high shrinkage degree and non-monolithic aerogels [88–90].

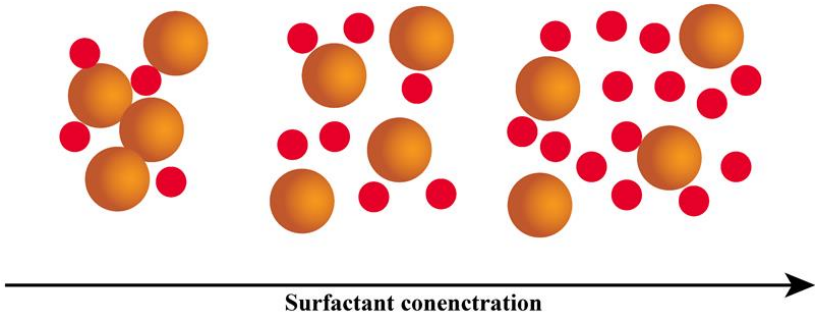

Fig. 4.2. Effect of surfactant concentration in a colloidal suspension. Orange spheres represent the colloidal particles; red spheres represent the surfactant molecules.

To avoid the weakening of the structure by the use of a surfactant, an acid catalyst was used that fulfills the function of attenuator of the reactivity of $Zr(OPr)_4$ and at the same time catalyzes the reaction [20,91–93]. Namely, the addition of acid will control the hydrolysis rate by protonating the -OR ligand thus creating a better leaving group and subsequently prevent precipitation [94].

These experiments were conducted under acidic conditions with HNO_3. A typical experiment was carried out as follows: a first solution was prepared by mixing 5 mL of 1-propanol with different amounts of 1M HNO_3, then, 1 mL of $Zr(OPr)_4$ was slowly added under vigorous stirring to avoid precipitation, resulting in a transparent solution. A second

solution was prepared by mixing 5 mL of 1-propanol with 0.05 mL of water. Finally, both solutions were mixed under vigorous stirring. In **Table 4.3**, the synthetic conditions are summarized.

Table 4.3. Aerogel samples synthesized by an acid-catalyzed approach

Sample	Zirconium propoxide $Zr(OPr)_4$	1-Propanol* $C_3H_8O_7$	HNO_3**	H_2O	Gelation time (min)	Results
Z009	1 mL	10 mL	0.05 mL	0.05 mL	-	Precipitation
Z010	1 mL	10 mL	0.1 mL	0.05 mL	10	White rigid gel
Z011	1 mL	10 mL	0.2 mL	0.05 mL	30	White soft gel
Z012	1 mL	10 mL	0.3 mL	0.05 mL	120	Weak gel
Z013	1 mL	10 mL	0.5 mL	0.05 mL	-	No gelation

* Total amount in two solutions; ** From 1M HNO_3 solution in 1-propanol

As listed in **Table 4.3**, if not enough acid is added, immediate precipitation occurs as in the experiment Z009. Further increase of the acid amount, progressively results in the increase of the gel time and formation of rigid gel, soft gel, and weak gel for 0.1, 0.2, and 0.3 mL of HNO_3 respectively. If the acid concentration is sufficiently high, then the condensation is completely suppressed. In this regard, the synthesized sample with 0.1 mL of HNO_3 was selected as the optimal and submitted to supercritical drying (the as-obtained sample is hereafter ZrO_2-AO). As can be observed in **Fig. 4.3**, the final specimen was a crack-free monolithic aerogel.

Fig. 4.3. Optimal ZrO_2 monolithic aerogel synthesized with 0.1 mL of HNO_3 under supercritical drying conditions of CO_2.

It is clear that the synthetic procedure to produce ZrO_2 aerogels is extremely sensitive to changes in the nature of the reagents and especially their concentration (e.g., H_2O and HNO_3). Once established the synthetic procedure to obtain zirconia aerogels, the next goal was the incorporation of the $Y(NO_3)_3$ to obtain Y_2O_3 7%wt. ZrO_2 aerogels (hereafter called YSZ). Thus, the next step was the addition of yttrium nitrate ($Y(NO_3)_3$). In this synthesis, 0.065 g of $Y(NO_3)_3$ were dissolved in 5 mL of 1-propanol and stirred for 10 min to ensure complete dissolution of the yttrium salt. Then, 0.1 mL 1M HNO_3 was added. To the obtained clear solution, 1 mL of $Zr(OPr)_4$ was slowly added under vigorous stirring and kept at such conditions 5 minutes. The second solution was prepared by mixing 5 mL of 1-propanol with 0.05 mL of distilled H_2O. Both solutions were then mixed under vigorous stirring and a transparent sol was formed. After a few minutes, the transparent sol became white and an increase in its viscosity was noticed. The complete gelation occurred after 10 minutes. Further supercritical drying yields a monolithic YSZ aerogel (the as-obtained sample is hereafter YSZ-AO) with a similar appearance to its ZrO_2 counterpart as shown in **Fig. 4.4**.

Fig. 4.4. Optimal YSZ monolithic aerogel synthesized with 0.1 mL of HNO_3 under supercritical drying conditions of CO_2.

It is clear that the incorporation of the Y^{3+} ions to form the aerogel of YSZ does not modify the synthetic protocol nor the obtained result since in both cases, high-quality monolithic aerogels are obtained. Thus, the synthetic protocol to prepare Zr-based aerogels was successfully optimized in terms of simplicity in comparison with the already reported methods. Moreover, with this procedure, crack-free aerogels were obtained which is useful for different applications [21,84,95]. This method also proved to be flexible to prepare

Zr-based aerogels since following the same method of synthesis; both pure zirconia aerogels and doped with Y_2O_3 were synthesized without major changes in the procedure.

4.1.1. Mechanism of formation of Zr-based aerogels

For a better understanding of the chemical process that takes place during the formation of Zr-based aerogels, a chemical mechanism of hydrolysis and condensation reactions was purposed based on the obtained experimental results.

As described in **Section 2.1**, during the hydrolysis reactions, the first step is the protonation of the alkoxide group, in this case, the zirconium propoxide ($Zr(OC_3H_7)_4$). Upon protonation, the partial positive charge on Zr ion is increased, leading to a nucleophilic attack (**Section 2.1**) from the H_2O molecule which has partially negatively charged oxygen with a pair of donor electrons thus forming a covalent bond as depicted in **Scheme 4.1**.

Scheme 4.1. The molecular mechanism of the acid-catalyzed hydrolysis of the Zr(IV) precursor leading to the formation of ZrO_2 and YSZ wet gels[10].

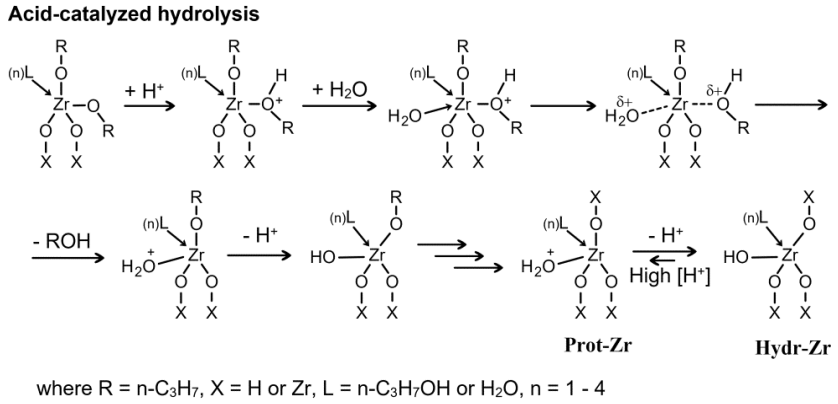

Then, as the oxygen atom forms the covalent bond with the Zr molecule, the –ROH becomes the leaving group and separates from the molecule while leaving an additional positive charge. The positive charge is repulsed by the Zr ion thus transferred to the surrounding H_2O molecule. Subsequently, the deprotonation of water occurs, the hydroxyl group (-OH) is formed and the replacement of one OR group by OH is completed. Once all alkoxide groups are hydrolyzed, a completely hydrolyzed transition complex is formed (denoted as Hydr-Zr). At this point, if the acid concentration [H^+] is high, it might protonate a hydroxyl group of the Hydr-Zr complex to form the transition complex Prot-Zr (**Scheme 4.1**).

To understand the role of acid concentration is necessary to observe**Table 4.4** and **Scheme 4.2**. From these results, can be noticed that at HNO_3 below 0.1 mL, precipitation occurs and above 0.4 mL the gelation is suppressed.

Table 4.4. Experimental conditions used to prepare samples ZrO_2-1, ZrO_2-2 and ZrO_2-3. ZrO_2-1: (@Moderate [H+]; ZrO_2-2: (@Medium [H+]; ZrO_2-3: (@High [H+].

Sample	**$Zr(OPr)_4$ [mL]**	**1-propanol [mL]**	**HNO_3 [mL]**	**H_2O [mL]**	***Tg*[a] [min]**	**Resultant gel**
ZrO_2-1	1	10	<0.1	0.05	NA	Precipitate
ZrO_2-2	1	10	0.1	0.05	10	Light white gel
ZrO_2-3	1	10	>0.4	0.05	NA	No gelation

a) Gelation time

In the proposed synthetic protocol, the nitric acid has two primary roles: control the hydrolysis and influence the rate and equilibrium state of the condensation reactions. Namely, at moderate acid concentrations (@Moderate [H+]) the condensation reactions are completed by H_2O and alcohol molecules which takes place in parallel (**Scheme 4.2a**). Independently if water or alcohol started the condensation, in the Hydr-Zr complex, the nucleophilic agent is the OH group and the leaving group is H_2O or alcohol (ROH) for water and alcohol condensation respectively. Thus, the formation of bridging Zr-O-Zr in the zirconia network takes place. If the acid concentration is higher (@Medium [H^+]), the protonated complex Prot-Zr is involved in the water condensation process. However, when the acid concentration is too high (@High [H^+]) the majority of the complexes are in the protonated form (Prot-Zr), therefore there is a substantial decrease of the active Hydr-Zr complex, which leads diminishing in the reactions rates and the condensation is inhibited. The overall process under strictly controlled conditions binds Zr to oxygen atoms until a particle is formed (so-called primary globules) in liquid media. The primary globules bond each other by O and OH terminal groups from larger aggregates also called secondary globules. These aggregates again link randomly to assemble a larger structure. As the number of aggregates increases, the formation of an open porous network takes place, which is accompanied by a loss of the sol fluidity until a rigid wet gel is formed [10].

When the sol turns into a wet gel, the aging process is required to complete the hydrolysis and condensation reactions (**Section 2.2**). Finally, the liquid within the pores is extracted under supercritical conditions with carbon dioxide as fluid to obtain the final aerogel.

Scheme 4.2. Sol-gel reactions of ZrO_2 aerogels; a) proposed mechanism for the formation of ZrO_2 nanoparticles and colloidal particles (sol) under different acidity conditions. b) The representation of the assembly of primary and secondary globules to a self-supported wet gel structure [10].

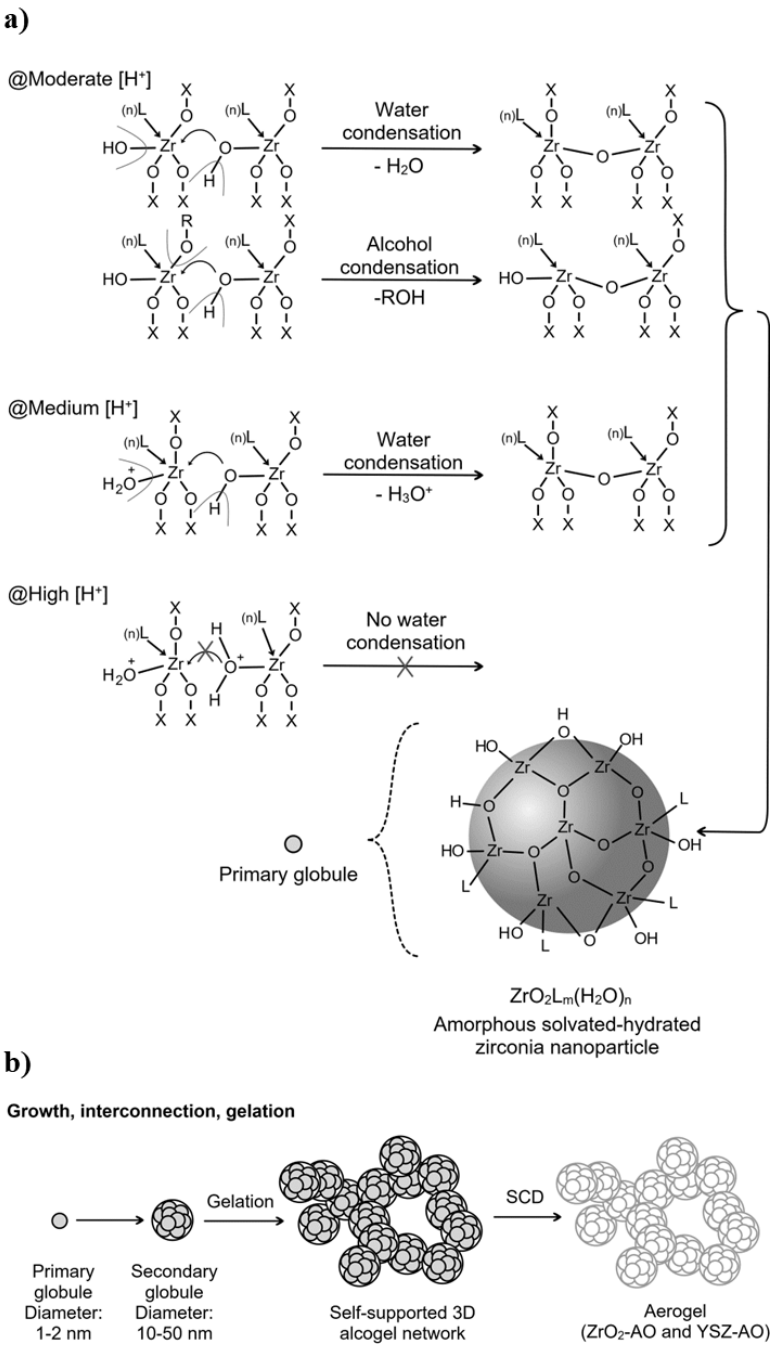

4.2 Characterization of ZrO_2 and YSZ aerogels

For high-temperature porous coatings applications, the structural changes upon heat treatment are important. Regardless of bulk or coating shaped aerogels, these materials commonly during experiment changes in their physicochemical properties (e.g., porosity, specific surface area, crystalline phase) after calcination [2,55,96]. Therefore, the effect of the temperature on the specific surface area, pore size distribution, surface morphology, and phase stability were evaluated.

As mentioned in **Section 2.4**, the thermal stability of materials for TBC applications is critical. Typically, the as-obtained aerogels result in amorphous state and their transition to a crystalline state is driven by several factors such as the nature of the reagents, pre, and post-processing of the material, heat treatment, crystallite size, etc. [21,94,105,106,97–104] In addition, these specimens contain traces of unreacted species, solvent molecules, and adsorbed water molecules. To investigate the physicochemical properties of the as-obtained aerogels (i.e. ZrO_2-AO and YSZ-AO) upon heat treatment a systematic study was carried out.

In **Fig. 4.5** are displayed the simultaneous thermogravimetric analysis (TG), differential scanning calorimetry (DSC), and mass spectroscopy (MS) of the ZrO_2-AO and YSZ-AO aerogels. Both samples follow similar patterns. The first mass loss at 121 °C takes place simultaneously with an endothermic peak in the DSC curve (**Fig. 4.5a and d**) which is associated with desorption of water molecules (MS plot in **Fig. 4.5b and e**) and is accompanied by changes of -7.84 wt.% and -7.59 wt.% for ZrO_2 and YSZ respectively. A broad exothermic peak arises from ~120 – 400 °C and ~150 – 450 °C complemented by mass loss of -4.87 wt.% and -16.97 wt.% for ZrO_2 and YSZ respectively. As can be seen in the MS data, these phenomena are directly related with the combustion of leftover synthesis products such as 1-PrOH (MS signal *m/z*: CO: 28, *m/z*: CO_2: 44) and HNO_3 (MS signal *m/z*: NO_x: 14, 30, and 46). As the temperature increased, a narrow exothermic peak at 419 °C and 455 °C for ZrO_2 and YSZ aerogels respectively were detected. These heat releases are attributed to the amorphous-to-tetragonal transition (later discussed in **Section 4.2.1**) of ZrO_2 due to there is no significant mass loss at these temperatures.

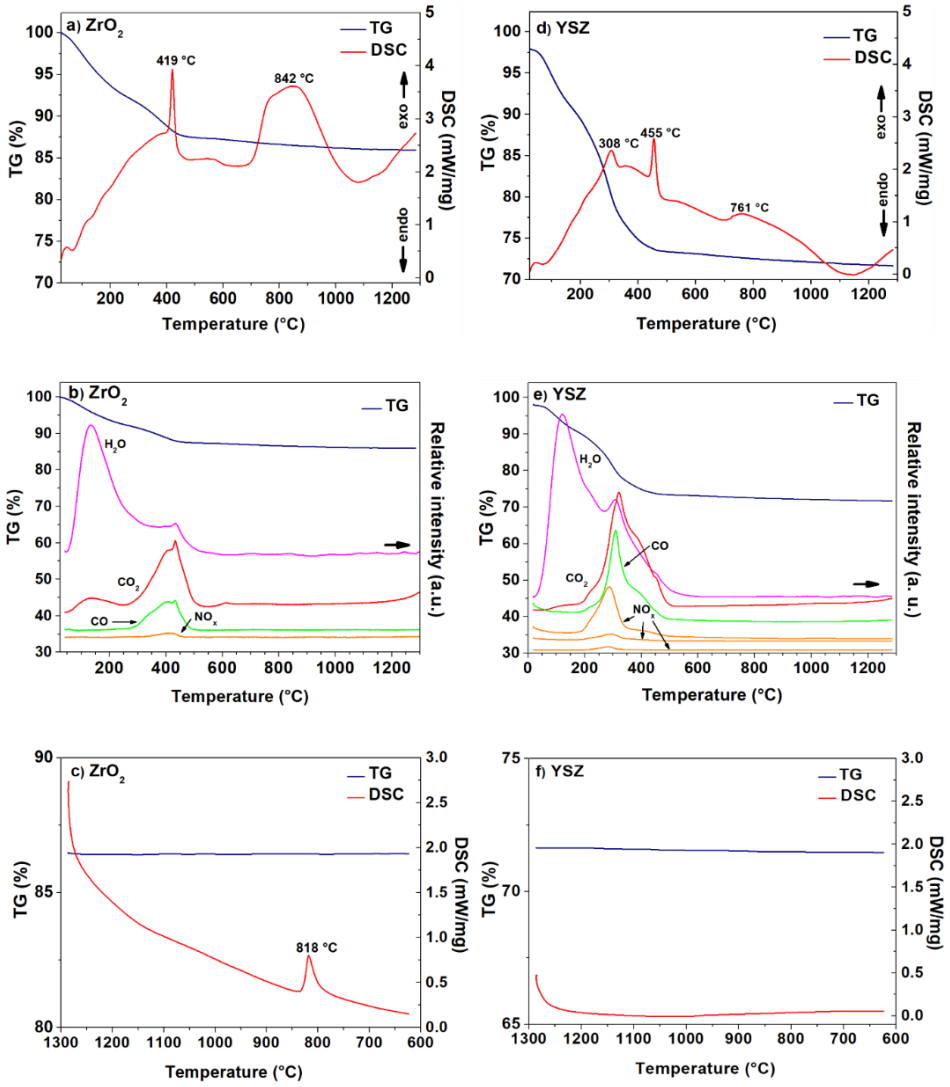

Fig. 4.5. Results of the thermal analysis of the as-prepared amorphous ZrO_2-AO and YSZ-AO aerogels. Comparison of the simultaneous TG/DSC signals and MS signals at m/z: H_2O: 18, CO: 28, CO_2: 44, and NO_x: 14; 30; 46, Graph a) and b): heating of the ZrO_2 sample. Graph c): cooling of the same sample. Graph d) and e): heating of the YSZ sample. Graph f): cooling of the same sample [10].

The difference of the crystallization temperature can be attributed to the presence of foreign species, such as ethoxy and nitrate groups in the YSZ aerogel [107]. This is supported by the significant larger weight loss of the YSZ aerogel (16.97 wt.%) in comparison with the ZrO_2 aerogel (4.87 wt.%) below 400 °C [10]. The ZrO_2 commonly experiment phase transformations during cooling down thus an additional DSC/TG analysis was performed (**Fig. 4.5c and f**) upon quenching to determine possible thermodynamic phenomena taking place. The ZrO_2 aerogel presented an exothermic event with a maximum at 818 °C without mass loss, determined as the transformation from tetragonal to monoclinic phase (**Fig. 4.8**);

whereas the YSZ aerogel does not show any additional thermodynamic event. This is indicative of the stabilization of the tetragonal phase at room temperature.

4.2.1 Effect of temperature on the aerogels properties

Upon exposure to high temperatures, the physicochemical properties of aerogels change. For instance, the porous structure of the material collapse and important changes on their porosity takes place. For porous coatings applications, these structural changes are of critical importance. Therefore, the effect of the calcination temperature on the specific surface area, pore size distribution, surface morphology, and phase stability were evaluated.

For such purpose, N_2 adsorption-desorption isotherms (**Fig. 4.6**) were measured to the as-obtained aerogels (ZrO_2-AO, YSZ-AO) and after calcination at 500 °C (ZrO_2-500, YSZ-500).

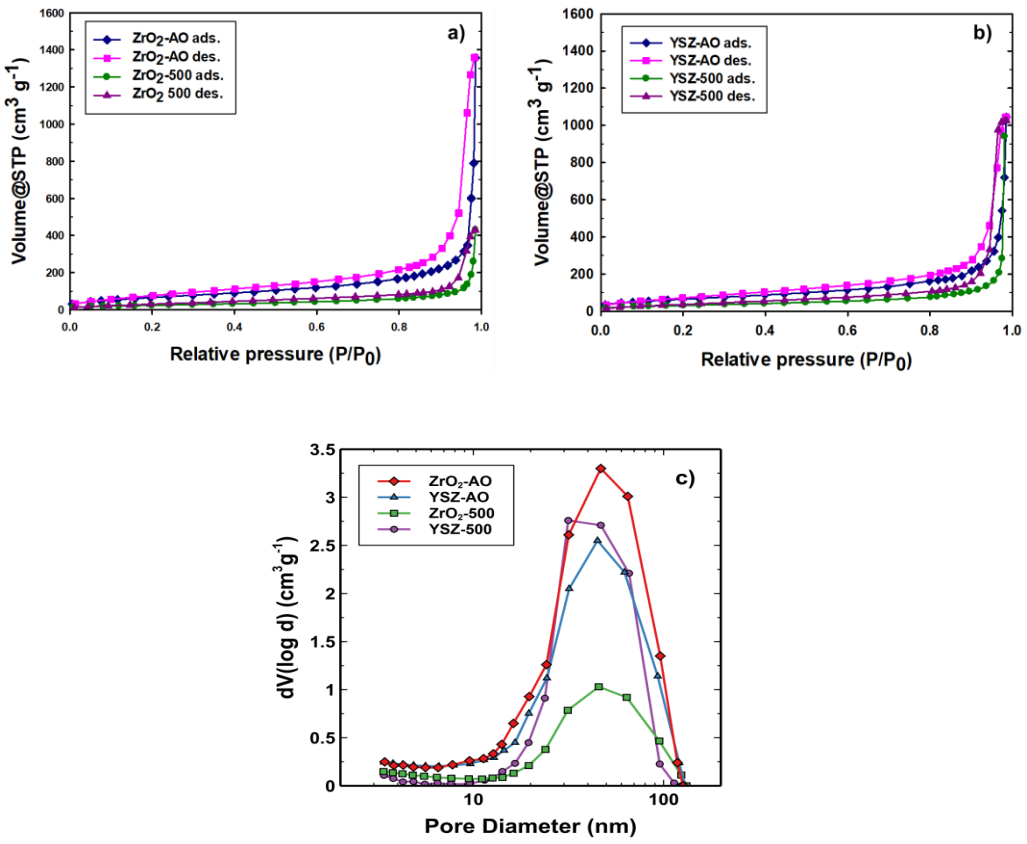

Fig. 4.6. Nitrogen gas adsorption (ads) – desorption (des) isotherms of ZrO_2 (a) and YSZ (b) aerogels as well as pore size distribution curves (c) before calcination (ZrO_2-AO, YSZ-AO) and after calcination at 500 °C (ZrO_2-500, YSZ-500)[10].

All the analyzed samples have a mesoporous structure confirmed by the adsorption-desorption curves type IV with H1 hysteresis [108]. The porosity properties of the studied aerogels are summarized in **Table 4.5**.

In **Table 4.5** can be observed that the ZrO_2-AO aerogel has a specific surface area (S_{BET}) of 255 $m^2 g^{-1}$ and a pore volume (V_p) of 2.1 $cm^3 g^{-1}$. Upon calcination at 500 °C, these values decreased to 87 $m^2 g^{-1}$ and 0.7 $cm^3 g^{-1}$ representing a reduction of 66% and 31% for S_{BET} and V_p respectively. The YSZ-AO aerogel has a S_{BET} of 243 $m^2 g^{-1}$ and a V_p of 1.6 $cm^3 g^{-1}$. After calcination, resulted in a drop of the S_{BET} to 114 $m^2 g^{-1}$ (54%) while the V_p remained unchanged. Characteristic pore sizes (the peak maximum of the distribution curve) are nearly identical for the as-obtained samples, and only moderately decrease upon heating at 500 °C. The macropore volume is calculated as the cumulative pore volume of pores $d > 50$ nm. The micropore contribution to the entire surface area was calculated by using the *t*-plot method, based on the de Boer model of statistical thickness [109]. There are no pores below $d = 2$ nm in the aerogels.

Table 4.5. Textural properties of the ZrO_2 and YSZ aerogels before and after calcination. Standard deviations are displayed for primary data.

Sample	S_{BET} [$m^2 g^{-1}$][a)]	V_p [$cm^3 g^{-1}$][b)]	$V_{mesopore}$ [$cm^3 g^{-1}$][c)]	$V_{macropore}$ [$cm^3 g^{-1}$][d)]	D_p [nm][e)]	$D_{p\text{-}avg}$ [nm][f)]	*C*-const.[g)]
ZrO_2-AO	255 ± 21	2.1 ± 0.2	1.4	0.71	47	33	39
ZrO_2-500	87 ± 13	0.7 ± 0.1	0.46	0.19	46	31	86
YSZ-AO	243 ± 14	1.6 ± 0.1	1.1	0.54	45	27	57
YSZ-500	114 ± 19	1.6 ± 0.3	1.3	0.35	37	56	83

a) BET specific surface area; b) Total pore volume; c) Pore volume of mesopores; d) Pore volume of macropores; e) Characteristic pore diameter: estimated at the maximum of the distribution curve; f) Average pore size: estimated by BJH method; g) Constant value as an indicator of the polarity of the sample surface [80,110].

The value of the *C*-constant is significantly higher for heat-treated samples, while the shape of the hysteresis loop remains unchanged. This indicates that the affinity of the probe gas (N_2) towards the aerogel surface is significantly different in AO and heat-treated samples. It can be assumed that a portion of the surface is covered with residual 1-propanol and unhydrolyzed propoxy groups in both the ZrO_2-AO and YSZ-AO aerogels. This is in

agreement with the detection of combustion products at ca. 400 ºC during the thermal analysis of as-prepared ZrO_2-AO and YSZ-AO samples (**Fig. 4.5**). The heat treatment of the aerogels at 500 ºC results in the desorption of residual solvents. The increase of the *C*-constant upon calcination is attributed to the elimination of residual nonpolar 1-propanol and propoxy groups from the surface which conducts the formation of new Zr-O-Zr bondings thus increasing its polarity [80,110].

The change of the total pore volume upon heat treatment indicates the shrinkage degree, which can be a reference criterion on the dimensional stability of the aerogels that in coatings for high-temperature applications is important due to the densification of the material. According to the values presented in **Table 4.5**, during heating, the ZrO_2-AO aerogel experiences a significant decrease in V_p since its value fall by 31% after heat treatment. On the other hand, the V_p of the YSZ aerogel does not change upon calcination at 500 °C / 2hrs which demonstrates that the YSZ aerogel is not only more stable to phase changes but is also less susceptible to dimensional changes upon calcination. Samples were also treated at the temperature of 1200 °C, however, at such conditions, the samples showed high densification degree and consequently, closing the open pores which resulted in values below 1 m^2 g^{-1}.

Microstructural and morphological changes before and after calcination at 500 °C / 2 hrs were also investigated. From **Fig. 4.7** is appreciated that the as-obtained samples have the characteristic aerogel microstructure built by aggregates of nanosized particles with no apparent differences between them. After heat treatment at 500 °C, the surface of the ZrO_2-500 sample shows some open pores and the particle aggregates are smaller. Both processes are due temperature effect because there is a restructuring of the material, which causes that aggregates formed by small nanoparticles to shrink and lose most of their porosity, although at the same time new pores are exposed as observed in **Fig. 4.7b**. This can be related to the decrease in the pore volume of the ZrO_2-500 determined by the adsorption-desorption of N_2 (**Table 4.5**). Such restructuring also has an influence on the YSZ sample since a greater concentration of aggregates on the surface can be observed. Therefore, the surface of the YSZ-500 is coarser containing larger aggregates. At 1200 ºC, the particles grow considerably and start to consolidate to form compact agglomerates that is indicative of an extensive sintering process. The ZrO_2 aerogel is highly densified and the loss of almost

all the porosity can be observed. Similar phenomena take place in the YSZ aerogel. Neither mesopores nor macropores are visible in the samples calcined at high temperatures. The observed morphologies by SEM are in good agreement with the porosimetry results (**Fig. 4.6** and **Table 4.5).**

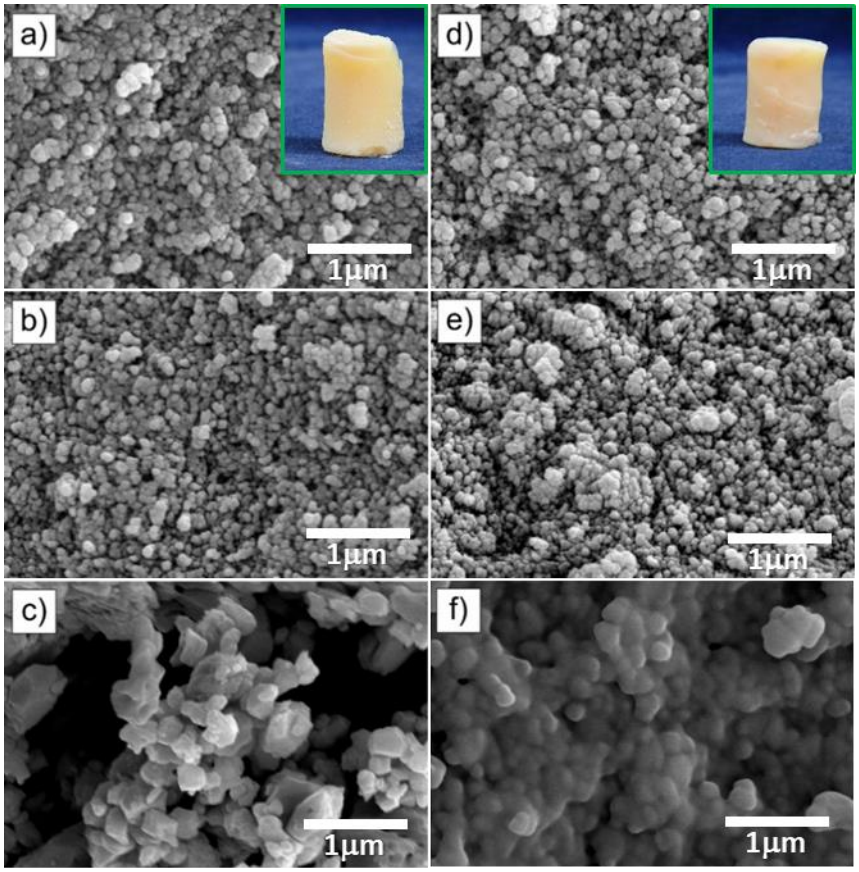

Fig. 4.7. SEM images of the ZrO_2 and YSZ aerogels before and after the heat treatment: a) ZrO_2-AO, b) ZrO_2-500, c) ZrO_2-1200, d) YSZ-AO, e) YSZ-500 and f) YSZ-1200. Insets: photographs of the ZrO_2-AO and YSZ-AO monoliths, respectively [10].

As earlier mentioned, any possible structural change in a material intended to be applied as top coat in a TBC system is of critical investigation due to such change that can incur adverse results. Therefore, the crystalline structure of both aerogels (ZrO_2 and YSZ) was investigated by powder X-ray diffraction (**Fig. 4.8**) immediately after supercritical drying (ZrO_2-AO and YSZ-AO), upon calcination at 500 °C / 2hrs (ZrO_2-500 and YSZ-500), and at 1200 °C / 2hrs (ZrO_2-1200 and YSZ-1200).

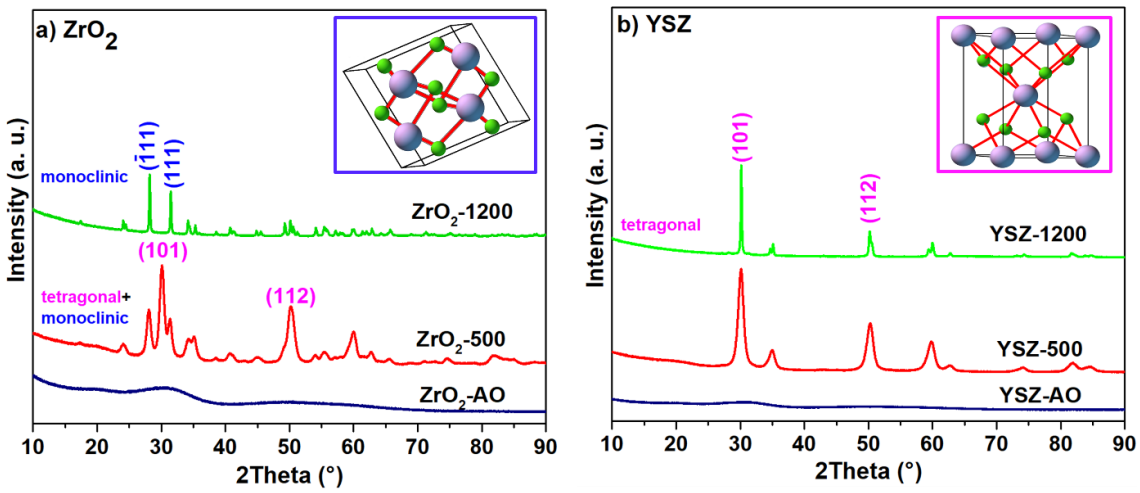

Fig. 4.8. X-ray diffraction patterns of a) ZrO_2 and b) YSZ aerogels before and after calcination at 500 ºC and 1200 ºC for 2 hrs. The diffraction patterns were taken after cooling to room temperature. Inset: monoclinic and tetragonal crystalline structures of ZrO_2[10].

As can be seen in the XRD patterns (**Fig. 4.8a**), the ZrO_2-AO aerogel is constituted by the amorphous phase that confirms the distinctive crystalline structure of the aerogels immediately after the supercritical drying process. However, upon calcination at 500 °C / 2hrs (ZrO_2-500 pattern), the amorphous zirconia transforms into a mixture of monoclinic (m-ZrO_2) and tetragonal zirconia (t-ZrO_2) confirmed by the appearance of the main diffraction peaks with oriented planes ($\bar{1}11$), (111) and (011), (112) for monoclinic and tetragonal phases, respectively. The YSZ-AO aerogel is also amorphous before calcination, however, contrary to the ZrO_2 aerogel, the calcination at 500 °C yields single t-ZrO_2 phase. When the samples are calcined at 1200 °C / 2hrs and quenched at room temperature, the t-ZrO_2 phase in the ZrO_2 aerogel transforms into m-ZrO_2 while in the YSZ aerogel continues stable without undesirable phase changes. These phase transformations are in good agreement with the exothermic peaks detected by the DSC curves. Namely, the peak found at 419 °C for the ZrO_2 aerogel corresponds to the transformation from amorphous to a mixture of monoclinic and tetragonal phases, whereas the peak at 455 °C of the YSZ sample represents an amorphous-to-tetragonal phase transition.

The presence of t-ZrO_2 at low temperature (500 °C) as in the ZrO_2-500 aerogel seems to have an inconsistency with the phase diagram established in 1975 [111] where t-ZrO_2 phase exists at high temperature (1170 – 2370 °C). Thus, to study the effect of temperature on the crystallographic evolution of the ZrO_2-AO and YSZ-AO aerogels, *in-situ* XRD

measurements were carried out every 100 °C from room temperature up to 1200 °C along with a study of temperature on the crystallite size.

As can be seen in **Fig. 4.9**, the ZrO_2-AO aerogel is amorphous up to 400 °C. However, at 500 °C, there is a sign of partial crystallization and the XRD displays the formation of the t-ZrO_2 with (011) orientation. At 700 °C, the oriented planes ($\bar{1}11$) and (111) appear corresponding to the m-ZrO_2 phase which is an indicator that the t-ZrO_2 transforms into the m-ZrO_2 phase.

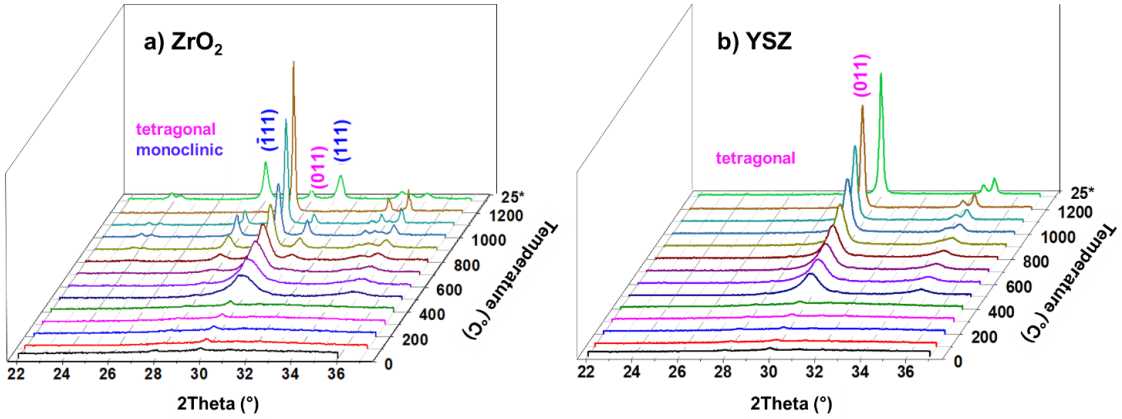

Fig. 4.9. Temperature-dependent XRD patterns of a) ZrO_2 and b) YSZ aerogels. In-situ XRD measurements from 25 to 1200 °C were performed during the calcination of the amorphous aerogels in order to determine their crystallographic evolution. The last pattern (25*) was recorded upon quenching [10].

In the interval from 700 to 1000 °C, the monoclinic is the dominant phase due to the tetragonal peaks are gradually reduced, while the monoclinic peaks become more intense. Another important observation is that as the temperature rises throughout the process, the diffraction peaks become sharper. This effect is an indication of a growth in crystal size due to the effect of temperature. Then, when the sample reaches 1100 °C, a new phase change takes place, most of the monoclinic phase is transformed back into tetragonal, and at 1200 °C, there is only tetragonal phase present. Subsequently, once the sample is cooled down to room temperature, the tetragonal phase is transformed into the monoclinic since it is the stable phase at these conditions. As can be seen in **Fig. 4.9b**, the YSZ-AO aerogel is amorphous up to 400 °C and at 500 °C the first crystallization peak appears (011) corresponding to the t-ZrO_2. Contrary to the ZrO_2-AO sample, there is no phase transition and single t-ZrO_2 is conserved the whole heating and cooling process. The only apparent

change is the sharpening of the t-ZrO_2 diffraction peaks. Thus, the ZrO_2 aerogel can be composed of either single-phase or a mixture of monoclinic and tetragonal phases in the range of 25 – 1200 °C. On the other hand, the developed synthesis yield a YSZ aerogel with high purity t-ZrO_2 phase and good thermal stability due to the tetragonal phase remains unchanged. In summary, the ZrO_2 aerogel experiment a phase evolution upon heat treatment is as follows: 1) initially the amorphous phase is dominant and transforms to tetragonal at 419 °C; 2) in the temperature range of 500 – 1000 °C, a tetragonal-to-monoclinic phase transition takes place leading the coexistence of monoclinic and tetragonal phases; 3) the monoclinic phase transforms to a tetragonal-dominant phase at 1100 °C with a complete transformation at 1200 °C; and 4) upon cooling-down the tetragonal phase completely transforms into monoclinic phase. For high-temperature coatings applications such as TBCs, these crystalline phase changes are critical since are accompanied by volume changes. These variations in volume induce enforced failure of the coating system.

Another important observation is the sharpening of the diffraction peaks as the temperature increases (**Fig. 4.9**), which might be indicative of crystallite size growth. Thus, the correlation between the phase transitions and the crystallite size was investigated. The crystallite size was calculated using Scherrer's equation (**Eq. 3.1**) and the phase composition of the ZrO_2 aerogel was determined by Rietveld refinement using the reference patterns of m-ZrO_2 (ICSD code: 18190) and t-ZrO_2 (ICSD code: 72950). Distributed nanocrystals can exist in the amorphous matrix of the as-prepared ZrO_2-AO aerogel. Such crystallites can be either monoclinic or tetragonal and can behave as preferential sites for grain growth in the dominantly amorphous ZrO_2 [94].

From **Fig. 4.10** is noticed that at 500 °C, amorphous zirconia mostly crystallizes into t-ZrO_2 with crystallites of ca. 6 nm. As the temperature rises, gradual growth of the crystals occurs and at 1000 ° C, they measure between 20 and 31 nm. During this period, there is a tendency in which the t-ZrO_2 phase is transformed into m-ZrO_2. However, as the temperature increases further, the crystals growth between 45-52 nm and the tetragonal phase begins to be dominant (1100 °C) and until at 1200 ° C it is the only phase present.

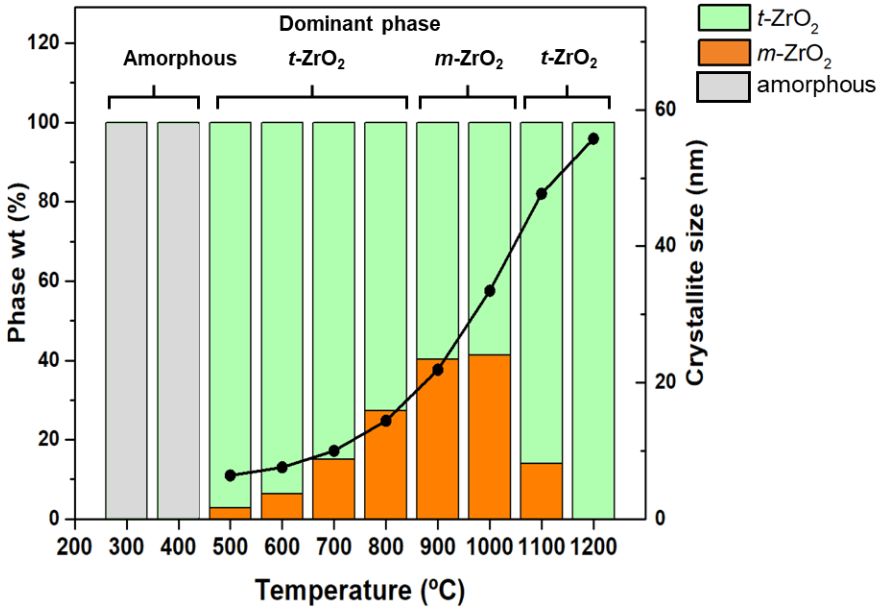

Fig. 4.10. The crystalline phase transitions of ZrO_2 aerogel during heat treatment. Correlation between the composition of the crystalline phase and crystallite size at different temperatures [10].

Based on the obtained results the tetragonal phase can exist only if the aerogel contains nanometer-sized crystallites. Several studies have reported the existence of the tetragonal phase at room temperature and provided various explanations for such behavior. Garvie stated that the crystallite size and therefore, free energy has an effect on the stabilization of the tetragonal crystalline phase [102]. In other words, m-ZrO_2 has a lower bulk free energy but t-ZrO_2 has a lower surface free energy. For crystallites below a certain critical size of 30 nm, the surface free energy term dominates over the bulk free energy term and the stabilization of the tetragonal phase becomes favorable. Moreover, Bedilo [86] suggested that tetragonal zirconia can exist at room temperature due the presence of organic compounds in the as-prepared aerogel matrix, as a consequence of the sol-gel technique. The burning of organic residues during calcination leads to local overheating and the stabilization of t-ZrO_2. Mitsuhashi *et.al.* [112] reported that such stabilization is due to strain effects in the nanoparticle regime. Others proposed that the formation of t-ZrO_2 is due to the short-range structural similarities between the amorphous phase and the t-ZrO_2 phase [113–116]. Garvie proposed that during calcination, initially a trace amount of m-ZrO_2 forms, because a small portion of the crystallites is bigger than the critical phase transition size. At higher temperatures, the size of the crystallites increases and the entire sample transforms to m-ZrO_2.

The obtained results show that the phase transformation of ZrO_2 is related to the crystallite size growth as temperature effect. Thus, the correlation between the crystallite size, temperature and phase stability of the ZrO_2 aerogel is displayed in **Fig. 4.11.**

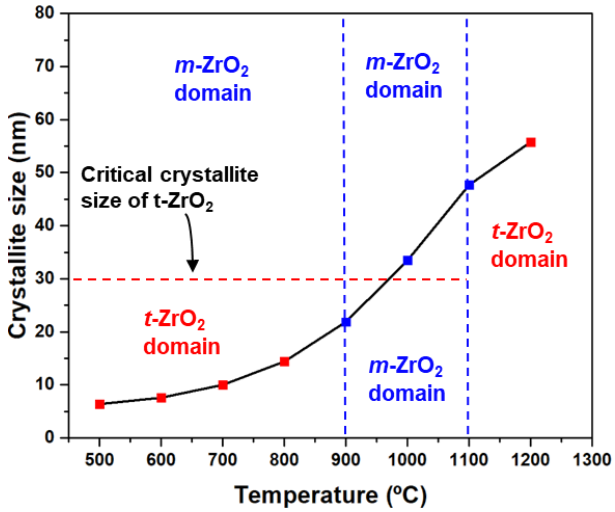

Fig. 4.11. Effect of temperature on crystallite size observed during the heat treatment of ZrO_2-AO aerogel. Crystallite size was calculated from in-situ XRD data (see **Fig. 4.9**) [10].

First, the amorphous ZrO_2 transforms into a t-ZrO_2 phase (crystallite size: 6.0 – 13.6 nm) in a thermodynamically controlled process that finishes at ca. 800 ºC. As the temperature increases to 900 ºC, the crystallite size approaches the critical size of t-ZrO_2 of 30 nm and the thermodynamic stability of the tetragonal and monoclinic phases become comparable. This results in a tetragonal-to-monoclinic phase transformation which becomes clearly visible at 1000 ºC where the critical crystallite size is reached (31.7 nm). The temperature component becomes dominant again close to the monoclinic-to-tetragonal phase transformation temperature of 1170 ºC. Subsequent heating at 1200 ºC leads to the complete transformation to a pure tetragonal phase.

The developed synthetic route to produce Zr-based aerogels intended for high-temperature coatings applications, yields high-quality bulk aerogels. All these studied properties are transferred from the bulk to the coating form. Namely, the temperature reduces considerably the porosity and therefore shrinks the material up to 60 % as in the case of the ZrO_2. However, the YSZ aerogel demonstrated lesser shrinkage degree and enhanced phase stability since single-phase tetragonal zirconia was present from the room temperature up to 1200 °C.

4.3. $Ln_2Zr_2O_7$ (Ln=La^{3+}, $Nd^{3+,}$ Gd^{3+} and Dy^{3+}) aerogels: Synthesis

In past years, rare-earth zirconate systems with pyrochlore or fluorite structures have emerged from seeking new materials that contribute to enhancing the current applications such as in the TBCs. Following the same trend, aerogels are promising nanomaterials to be used as material precursors for this important industrial application. Even more interesting, the combination of both systems such as aerogels and rare-earth zirconates has started the motivation to produce aerogels with $Ln_2Zr_2O_7$ composition. Namely, the main goal of this research stage is to synthesize rare-earth zirconate aerogels and study their properties with respect to potential TBC applications. To this purpose, a variant of the previously described synthetic protocol for ZrO_2/YSZ aerogels synthesis was tailored to be able to prepare 4 rare-earth zirconate aerogels ($Ln_2Zr_2O_7$; *Ln* = La^{3+}, $Nd^{3+,}$ Gd^{3+}, and Dy^{3+}). Such studies do not exist in the literature. Since such aerogels (LnZA) were prepared for the first time, conventional powders (LnZP), and the aerogels' counterpart xerogels (LnZX) were prepared by co-precipitation and sol-gel method, for comparison purposes, respectively. Upon preparation, physicochemical characterization was performed to all the studied systems.

4.3.1. Lanthanide zirconate $Ln_2Zr_2O_7$ aerogels (LnZA)

Single-phase pyrochlore zirconates are of great interest for TBCs applications due to, among other properties, its thermal stability that even surpasses the over exploited YSZ-based TBC. To develop a methodology to synthesize lanthanide zirconate (LZ) aerogels with pyrochlore structure, very strict synthetic conditions must be carried out. In a first series of experiments, lanthanide zirconate aerogels (LZA_1, $La_2Zr_2O_7$; NZA_1; $Nd_2Zr_2O_7$; GZA_1, $Gd_2Zr_2O_7$; DZA_1; $Dy_2Zr_2O_7$) were investigated.

Following a similar procedure as the YSZ aerogels, two solutions were prepared. In the first one, 0.1 mL of HNO_3 was diluted in 5 mL of 1-propanol. Then, after 5 minutes under mild stirring, the $Zr(OPr)_4$ was slowly added. Once the reagents were homogenized, $Ln(NO_3)_3{\cdot}xH_2O$ was added and kept under stirring for 30 min. The ratio Zr:Ln was kept 1:1. A second solution containing 5 mL of 1-propanol and 0.4 mL of H_2O was prepared. Then both solutions were mixed together. Immediately after both solutions were mixed, a colored wet gel was obtained (**Fig. 4.12**).

Fig. 4.12. Obtained LZ wet gels after different gelation times. From left to right: $La_2Zr_2O_7$, $Nd_2Zr_2O_7$, $Gd_2Zr_2O_7$, and $Dy_2Zr_2O_7$.

After gelation was completed, the standard supercritical drying was performed (**Section 3.1.2**). Then the as-obtained aerogel was dried at 120 °C for 12 hrs to remove non-extracted by-products. Finally, all samples were calcined (1000 °C for 5hrs) to investigate the obtained crystalline structure.

As can be observed in **Fig. 4.13**, the neodymium zirconate aerogel (NZA_1), gadolinium zirconate aerogel (GZA_1) and the dysprosium zirconate aerogel (DZA_1) are single-phase $Ln_2Zr_2O_7$ system. However, the lanthanum zirconate aerogel (LZA_1) was a mixture of $Ln_2Zr_2O_7$ with lanthanum oxide (La_2O_3; hexagonal). The existence of the La_2O_3 phase may come from unreacted $La(NO_3)$ due to the formation of $La_2Zr_2O_7$ is conducted by the interaction of Zr^{4+} and La^{3+} ions. Particularly, in the sol-gel method, so that the hydrolysis and condensation reactions are carried out, all the reagents involved have to interact simultaneously, and initially this occurs in a liquid medium. However, as the reactions proceed, the formation of nanoparticles distributed throughout the volume takes place. Once the amount of nanoparticles increases to a number such that they begin to interact with each other, the stability of the sol breaks down and results in a gradual increase (which can be fast or slow) of the viscosity of the sol until it gels (gel point). Then, the sol transforms into a rigid wet gel that hinders the movement of species that did not react before gelation. Such a reduction in movement may result in a certain amount of reagents – like lanthanum – no longer interacting with zirconium molecules but reacting with neighboring molecules to form La_2O_3.

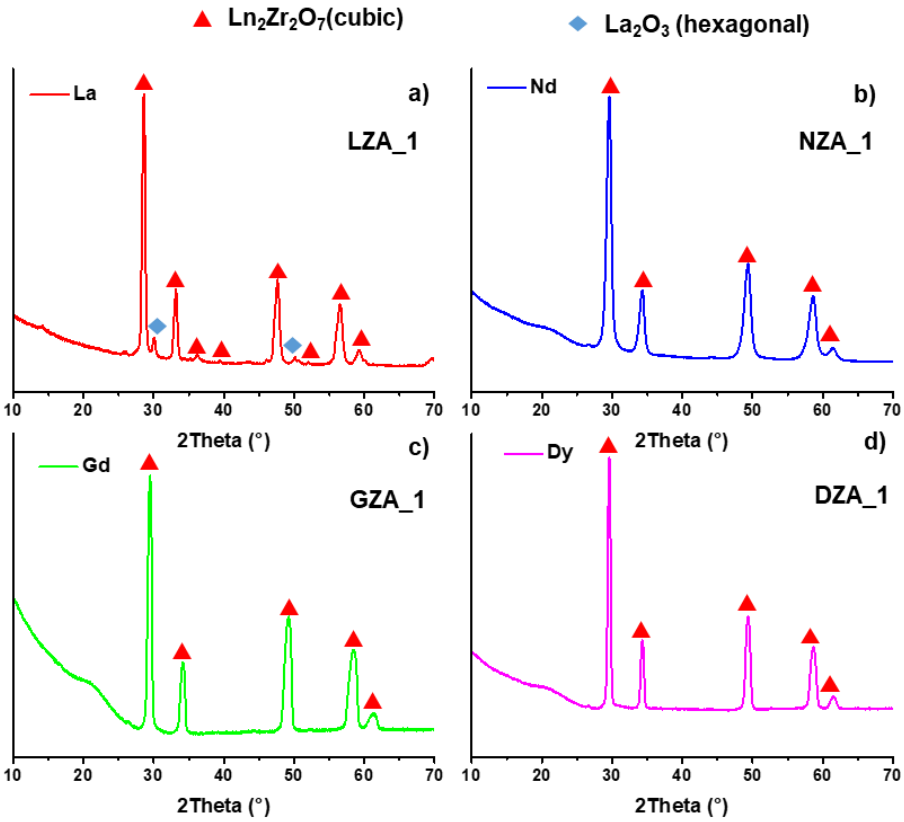

Fig. 4.13. Powder X-ray diffraction pattern of the calcined samples at 1000 °C / 5hrs.

To extend the gelation time and therefore longer reaction period, the solvent concentration was increased as shown in **Table 4.6**. As can be seen, the gradual increase of the 1-propanol resulted in longer gelation times and extends the reaction period before the sol turns into a gel. In **Fig. 4.14**, are displayed the X-ray patterns of the calcined samples at 1000 °C / 5hrs with different 1-propanol concentrations.

Table 4.6. The phase composition of the calcined aerogels with different volumes of 1-propanol and the agreement indices of the phase composition analyses.

Sample	1-propanol/mL	Tg/(min)	Rp	Re	GOF	Wt. % $La_2Zr_2O_7$	Wt. % La_2O_3
LZA_20	20	20	4.5	3.0	4.0	97.7	2.3
LZA_25	25	35	4.4	2.8	4.5	93.5	6.5
LZA_30	30	50	5.4	3.0	5.9	96.2	3.8
LZA_35	35	120	4.8	3.0	5.3	91.9	8.1

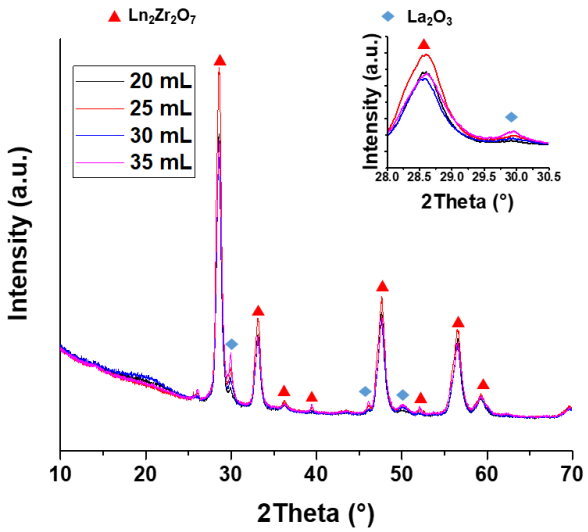

Fig. 4.14. X-ray diffraction patterns of the calcined LZX using different 1-propanol concentrations.

Unexpectedly, the increase in the gelation time seems to have a direct effect in the formation of the undesired secondary phase (La_2O_3); being the sample with 20 mL of 1-propanol the aerogel with less presence of lanthanum oxide (2.3 wt.%). On the contrary, the sample with 35 mL owns a larger amount (8.1 wt.%). In the binary system Zr^{4+}/La^{3+} in solution, as in the present case study, the hydrolysis and condensation reactions are more complicated since it is greatly affected by the pH of the reaction medium. Namely, according to the mechanisms proposed in the previous section, condensation reactions can result in either the formation of Zr-O-Zr, La-O-La, or Zr-O-La bonds. However, has been reported that under acid pH, Zr^{4+} tends to form the Zr-O-Zr bonds [117]. If this occurs, La^{3+} ions cannot easily be hydrolyzed to form the hydroxo bond (La-OH). Then, a relatively rapid formation of Zr-O-Zr and a slowdown of the La-O-Zr and La-O-La link occurs. If this process takes place, the three-dimensional gel will be rich in Zr-O-Zr bonds. Therefore, the La^{3+} ions that did not react either form La_2O_3 or are washed out in the aging process or in supercritical drying.

This effect can be corroborated in the LZA_12 experiment in **Table 4.7**. When an excess of La^{3+} is present, Zr^{4+} becomes the limiting reagent and thus, as the reactions proceeds, during the formation of $La_2Zr_2O_7$, most of the Zr^{4+} ions are consumed, while the La^{3+} ones are chemically active in the system, prone to form the La_2O_3 (13.3 %). On the other hand, when there is an excess of Zr^{4+}, the limiting reagent is the La^{3+} ions which result in the formation of t-ZrO_2 as in the sample LZA_21.

Table 4.7. The phase composition of the calcined aerogels with different reagents ratio and the agreement indices of the phase composition analyses.

Sample	Zr:La (mol)	H_2O (mL)	Rp	Re	GOF	Wt. % $La_2Zr_2O_7$	Wt. % La_2O_3	Wt. % t-ZrO_2
LZA_12	1:2	0.3	4.8	3.0	4.2	86.7	13.3	-
LZA_21	2:1	0.3	5.8	2.3	9.7	68.3	-	31.7
LZA_2101	2:1	0.1	6.4	4.6	8.2	62.3	-	37.7
LZA_2104	2:1	0.4	4.3	2.2	6.1	37.4	-	62.6

From these two experiments is reasonable the fact that changes in the Zr:La, directly affect the purity of the final aerogel, developing the formation of secondary phases, either La_2O_3 or ZrO_2. An additional factor that can be affecting such results is the water concentration. Namely, the amount of water in the medium affects greater the hydrolysis of $Zr(OPr)_4$ than that of $La(NO_3)_3$. As can be seen in **Fig. 4.15**, when there is a relatively large amount of water (sample LZA_1104 with 0.4 mL of H_2O), the formation of the t-ZrO_2 phase is significantly favored while with a small amount of water (0.1 mL of sample LZA_1101, **Table 4.7**), the amount of the tetragonal phase is considerably reduced. In fact, the sample in which the only water present comes from the reagents (0.02 mol in the LZA_1100 sample), revealed only the $La_2Zr_2O_7$ phase. This reaffirms the sensitivity of sol-gel reactions to the H_2O concentration when a zirconium propoxide such as $Zr(OPr)_4$ is used, which controls the hydrolyzing of the compounds.

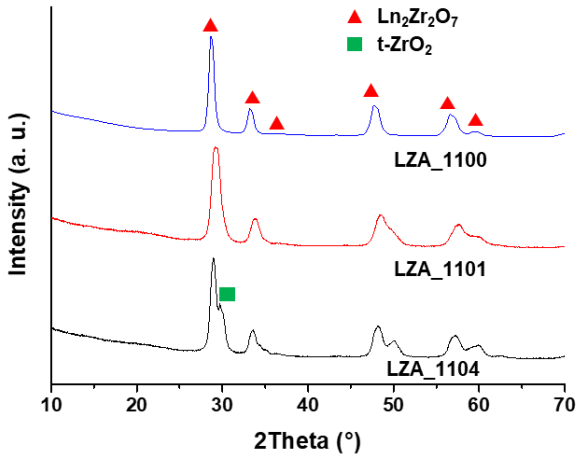

Fig. 4.15. Powder XRD patterns of the lanthanum zirconate aerogels synthesized with different [H_2O] and a Zr : La ratio 1 : 1.

From these experiments can be stated that the formation of $La_2Zr_2O_7$ is always prioritized over the other secondary phases such as La_2O_3 and t-ZrO_2, which forms upon changes in the limiting reagents.

Since this is the first time $Ln_2Z_2O_7$ (LZ) in aerogel form is produced, for comparison purposes two additional materials were parallel analyzed; namely the well-known LZ powders (LnZP; Ln = La, Nd, Gd, and Dy) synthesized by co-precipitation method and LZ xerogels (LnZP; Ln = La, Nd, Gd, and Dy) which only differ with aerogels by their drying methodology.

4.3.2 $Ln_2Zr_2O_7$ materials characterization: powders, xerogels, and aerogels

To investigate the crystalline phase of the studied lanthanide zirconate powders, xerogels, and aerogels upon calcination, all the studied materials were summited to a heat treatment (**Table 4.8**) and analyzed by XRD as shown in **Fig. 4.16**.

Table 4.8. Summary of the calcination process performed to each as-obtained sample.

Sample	Label	S_1 (°C)	R_1 (°C/min)	D_1 (h)	S_2 (°C)	R_2 (°C/min)	D_2 (h)
***Ln*$_2$Zr$_2$O$_7$ powders**	*Ln*ZP	120	3.3	12	1000	3.3	5
***Ln*$_2$Zr$_2$O$_7$ xerogels**	*Ln*ZX	120	3.3	12	1000	3.3	5
***Ln*$_2$Zr$_2$O$_7$ aerogels**	*Ln*ZA	120	3.3	12	1000	3.3	5

* S: temperature setpoint; R: used heating ramp; D: dwell time; Ln = La, Nd, Gd, and Dy.

In comparison with the ZrO_2 and YSZ aerogels with a mixture of tetragonal and monoclinic zirconia or single-phase tetragonal respectively, after calcination at 1000 °C all the samples presented a cubic crystalline structure consistent to the Miller indices (222), (400), (440), (622), and (444) which can be assigned to cubic phase with either ordered pyrochlore (P) or disordered fluorite (F) structures. The main distinction between these two structures is two characteristic diffraction peaks of the pyrochlore structure located at 2θ on 36° and 45° oriented in (331) and (551) respectively. However, these peaks commonly have low intensity and are difficult to detect owing to the broadened nature of the XRD peaks of the nanostructured materials and their variations with the processing [74]. For instance, the synthesis of $La_2Zr_2O_7$ powders by co-precipitation method yields single-phase pyrochlore after calcination at 1000 °C [118] while other authors report pyrochlore phase $La_2Zr_2O_7$ xerogels after calcination at 1000 °C by means of a combination of sol-gel and hydrothermal

methods [119]. Fuentes *et.al.* obtained several $Gd_{2-x}Ln_xZr_2O_7$ materials with fluorite structure by a mechanical induced reaction method from the room temperature up to 800 °C and further phase transition to pyrochlore structure [120]. Thus, the pre/post-processing has an important influence on the crystalline phase of the final product. This, coupled with the difficulty of detecting the P phase, makes the use of an additional technique, such as Raman spectroscopy, necessary to determine the composition of the materials. Another important observation was the broadening of the diffraction peaks that tends to increase proportionally with the atomic number of the incorporated rare-earth ion. Hence, the crystallite size of all the studied materials was estimated by Scherrers' equation (**Eq. 3.1**). In the **Fig. 4.16d** are displayed the crystallite sizes of powders, xerogels, and aerogels.

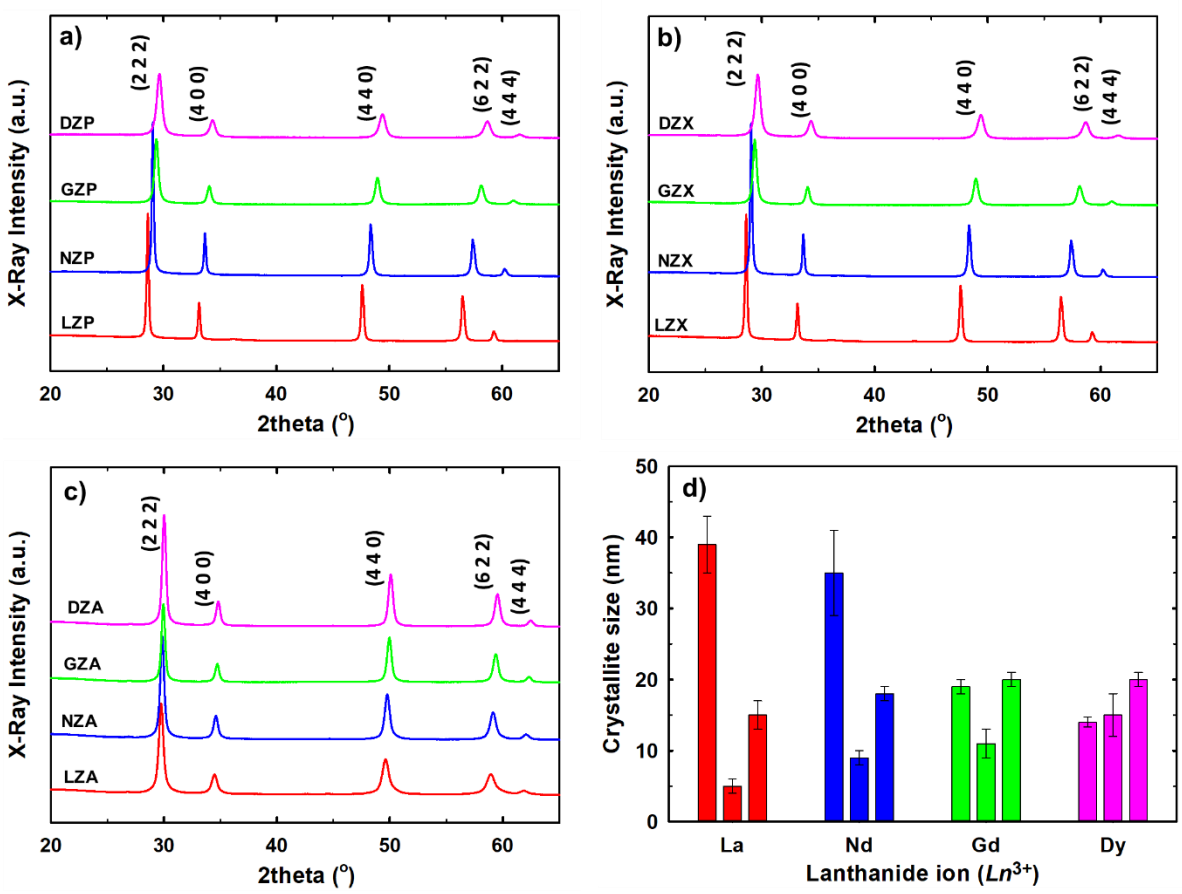

Fig. 4.16. X-ray diffraction patterns of the calcined materials at 1000 °C: a) powders (LnZP); b) xerogels (LnZX); c) aerogels (LnZA) and d) calculated crystallite size as a function of the lanthanide ion (Ln^{3+}). For each element, from left to right, each bar corresponds to LnZP, LnZX, and LnZA, respectively [121].

As can be seen, the lanthanide zirconate powders (LnZP) have crystallites of 39±4, 35±6, 19±1, and 14±0.7 nm for LZP, NZP, and GZP respectively. The values show that the crystals tend to decrease as the atomic number of the rare earth ion increases. These results suggest that in the case of powders (synthesis by co-precipitation) crystal growth is inhibited largely by incorporating larger rare-earth ions. In the case of materials prepared by sol-gel chemistry, the opposite effect takes place as in the case of xerogels (LnZX) and aerogels (LnZA). In these materials, the trend is the higher the atomic number, the smaller the crystallites. For instance, the LXZ has a crystallite size of 5±1 nm while the DXZ of 15±3 nm. In general, the sol-gel materials are composed up to 8 times smaller crystallites than the powders. There is a noticeable difference in crystallite sizes in relation to the synthesis followed to obtain different materials since the post-processing after the synthesis was identical.

As mentioned above, there are differences in the crystalline structure of phases F and P that are imperceptible to the XRD technique and that can have a great impact on the structural properties of the material. Due to this, it is necessary to study in-depth the effect of the incorporation of different rare-earth ions in the materials.

According to the group theory (**Eq. 4.1**) [122,123], the difference between the pyrochlore and fluorite structures in $Ln_2Zr_2O_7$ compounds is that the pyrochlore structure has 6 Raman active modes in the center of the Brillouin zone, while the fluorite structure is characterized by a single Raman active mode (F_{2g} located at approx. 466 cm^{-1}) which due to randomly distribution of oxygen atoms in the lattice, this band shape is broad.

$$\Gamma = A_{1g} + E_g + 4F_{2g} \qquad (\boldsymbol{Eq.\,4.\,1})$$

To investigate these structural variations, the samples were analyzed by means of Raman spectroscopy at room temperature (**Fig. 4.17**). As can be observed, for the LZP (**Fig. 4.17a)**, the observed vibrational modes are a band at 514 cm^{-1} which corresponds to the A_{1g} mode assigned to O-Zr-O bending vibrations of ZrO_6 octahedral; the most intense band is located at 297 cm^{-1} assigned to the E_g mode and is correlated to Zr-O bending vibrations; the last bands located at 391 and 495 cm^{-1} are assigned to La-O and Zr-O stretching vibrations with some contribution of bending vibrations, respectively, corresponding to the

F_{2g} mode [124–126]. Raman band analysis complements the XRD findings and ordered pyrochlore structure (Fd3m) was determined in the LZP sample. In the case of the NZP (**Fig. 4.17b**) the same vibrational modes were detected. First, the A_{1g} mode was located at 519 cm^{-1} related to the O-Zr-O bending. Then most intense band was situated at 306 cm^{-1} corresponding to the E_g mode. Lastly, the F_{2g} vibration modes were observed at 385 and 585 cm^{-1} [125,127]. In the case of GZP and DZP samples, similar results were obtained. Raman spectra do not show the single band of a typical fluorite structure, but several ones can be observed (**Fig. 4.17c-d**). Nevertheless, the contributions of all the vibrational modes can not be clearly assigned without fitting Lorentzian functions due to the broadening of the collected spectra. The Raman spectra of the GZP and DZP show the characteristic bands of pyrochlore structures, however, in these cases was not possible to determine whether DZP and GZP have pyrochlore or defect fluorite structures. Taking this under consideration, previous publications suggest that DZP and GZP compounds represent disordered fluorite structures with some order at the microdomain levels [126]. This effect has been observed in materials obtained by different synthetic routes [125,126,128].

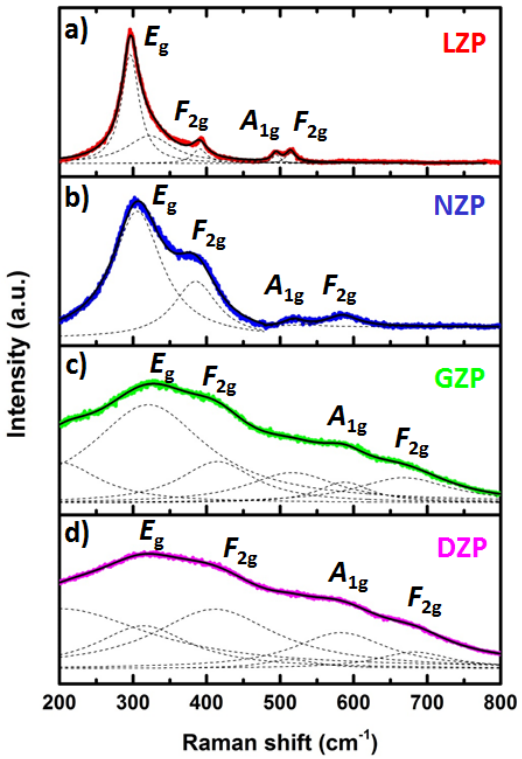

Fig. 4.17. Raman spectra of LnZP materials at ambient conditions: a) LZP, b) NZP, c) GZP and d) DZP. Vibrational modes of the pyrochlores and/or fluorite structures are identified [121].

In general, similar patterns were obtained from the LnZX (**Fig. 4.18**). The vibrational bands of the LZX were located at 298, 392, 497 and 517 cm^{-1} for A_{1g}, E_g, F_{2g} respectively (**Fig. 4.18a**). The obtained spectra of all the xerogels are slightly broader in comparison with their LnZP counterparts. Namely, the spectrum of the sample with La^{3+} ions is to some extent broader than the LZP. Additionally, the GZX and DZX samples are very similar to the powders since, according to the vibrational modes obtained, it results in fluorite structure with small contributions corresponding to the pyrochlore phase. However, the NZX sample is very different since its pattern is very broad which is composed of comparable vibrational modes to those of the NZA aerogel which is detailed below. The combination of XRD and Raman spectroscopy shows the change of structure in LnZP and LnZX nanostructured materials when replacing the *Ln* site by either La^{3+}, Nd^{3+}, Gd^{3+}, or Dy^{3+} cations, leading into a transformation from ordered pyrochlore structure to a disordered fluorite structure with a certain order at the microdomains. The tendency to have disordered structure increases with moving from La^{3+} to Dy^{3+} in the lanthanide series.

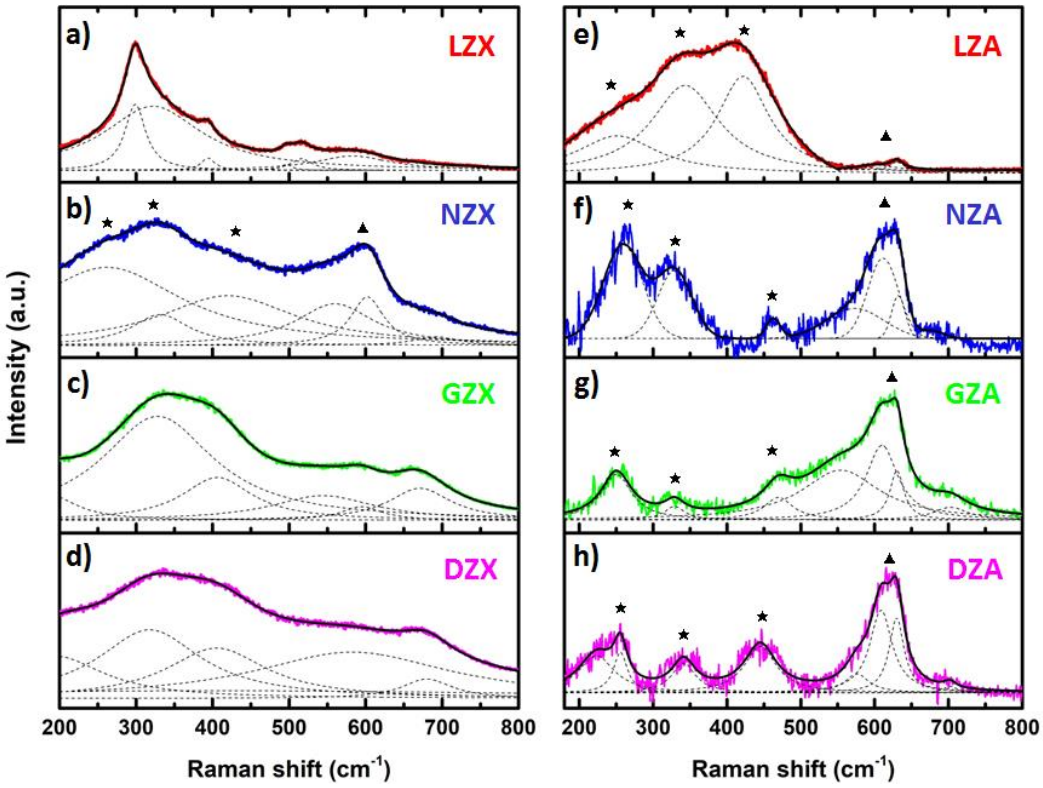

Fig. 4.18. Raman spectra of LnZX and LnZA materials at ambient conditions: a) LZX, b) NZX, c) GZX, d) DZX, e) LZA, f) NZA, g) GZA and h) DZA. Vibrational modes of tetragonal zirconia are depicted with stars (*) and vibrational modes of LnZ cubic phase are depicted with triangles (▲) [121].

The Raman spectra of aerogels are displayed in **Fig. 4.18e-h**. A broad band between 530-670 cm^{-1}, characterizes the patterns of the LnZA and additional poorly defined bands associated with the disordered oxygen sublattice [85]. This behavior was observed in the NZA, GZA, and DZA where the cubic structure is the dominant phase as demonstrated by band with maximum around 500-650 cm^{-1}.

However, was not possible to clearly state whether fluorite or pyrochlore structures. These samples also have various bands distributed along the spectrum located between 250-259, 328-339, and 450-470 cm^{-1}, which are attributed to a small amount of the tetragonal phase of the zirconia [129] since the cubic zirconia has a single Raman band [130].

The presence of the t-ZrO_2 was not possible to detect by XRD due to the great similarity between both patterns [131] and the amount of tetragonal phase is below the detection limit of XRD technique (~3% wt. in a two-phase mixture). For instance, the LZA sample presented all the characteristic bands of both t-ZrO_2 and $La_2Zr_2O_7$ structures.

The LZX and NZX contain only pyrochlore structure and the GZX and DZX are composed of mainly fluorite with some amount of pyrochlore structure. All the synthesized aerogels have a mixture of $Ln_2Zr_2O_7$ and t-ZrO_2. Since both systems were prepared with the same composition (ambient drying and supercritical drying for xerogels and aerogels, respectively), these results suggest that the drying process has an influence in the final crystalline structure of the prepared materials. Some authors have reported the influence of the supercritical drying in the final properties of materials [132–135]. However, the supercritical drying process is a relatively new method of processing of materials and is still under constant research to understand its direct influence.

To identify the energetic processes taking place in the LZ materials, simultaneous analysis of thermal analysis and mass spectrometry of the as-prepared samples were performed from 25 up to 1400 °C. In the LnZP samples, an endothermic peak (**Fig. 4.19**) appears from 50 to 200 °C, which according to the MS data (**Fig. 4.20**), corresponds to the desorption of H_2O molecules. Such water release results in a weight loss of 8, 12, 5, and 6 wt.% for LZP, NZP, GZP, and DZP respectively, and continues up to ~400 °C with the exception of GZP where it is observed at up to 600 °C.

Then, as the temperature rises, the combustion of organic compounds occurs in two stages. The first was identified as an exothermic peak from 200 to 400 °C, consistent with the detection of CO, CO_2, and NO_x in the MS plots. In the second combustion process, based on the DSC plot, an additional exothermic peak situated between 600-800 °C was observed. However, from the MS data was appreciated that the thermal event finalized beyond 1000 °C as in the LZP. In fact, in certain samples, the degradation of encapsulated of residual synthesis compounds continues up to 1300 °C as in the case of NZP and DZP.

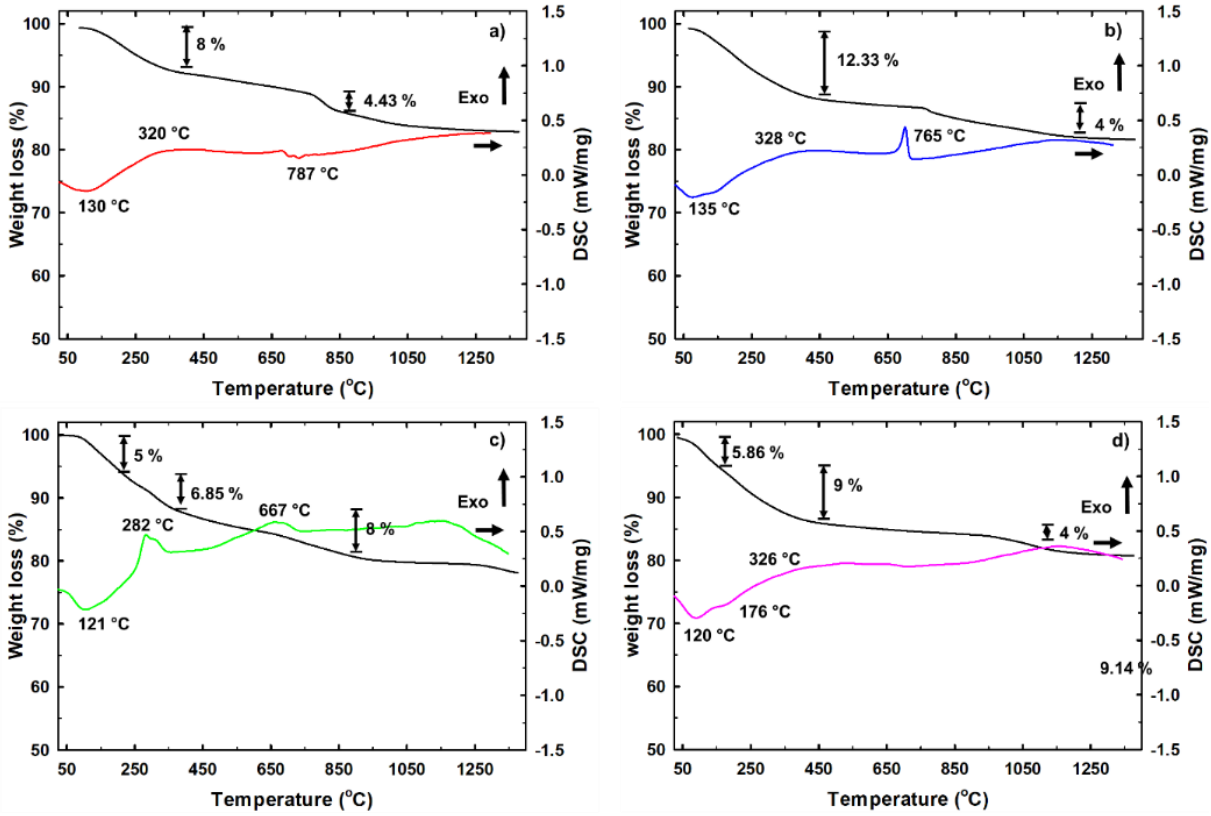

Fig. 4.19. DSC/TGA patterns (from 25 to 1400 °C) of the as-obtained $Ln_2Zr_2O_7$ powders; a) $La_2Zr_2O_7$; b) $Nd_2Zr_2O_7$; c) $Gd_2Zr_2O_7$; and d) $Dy_2Zr_2O_7$ [121].

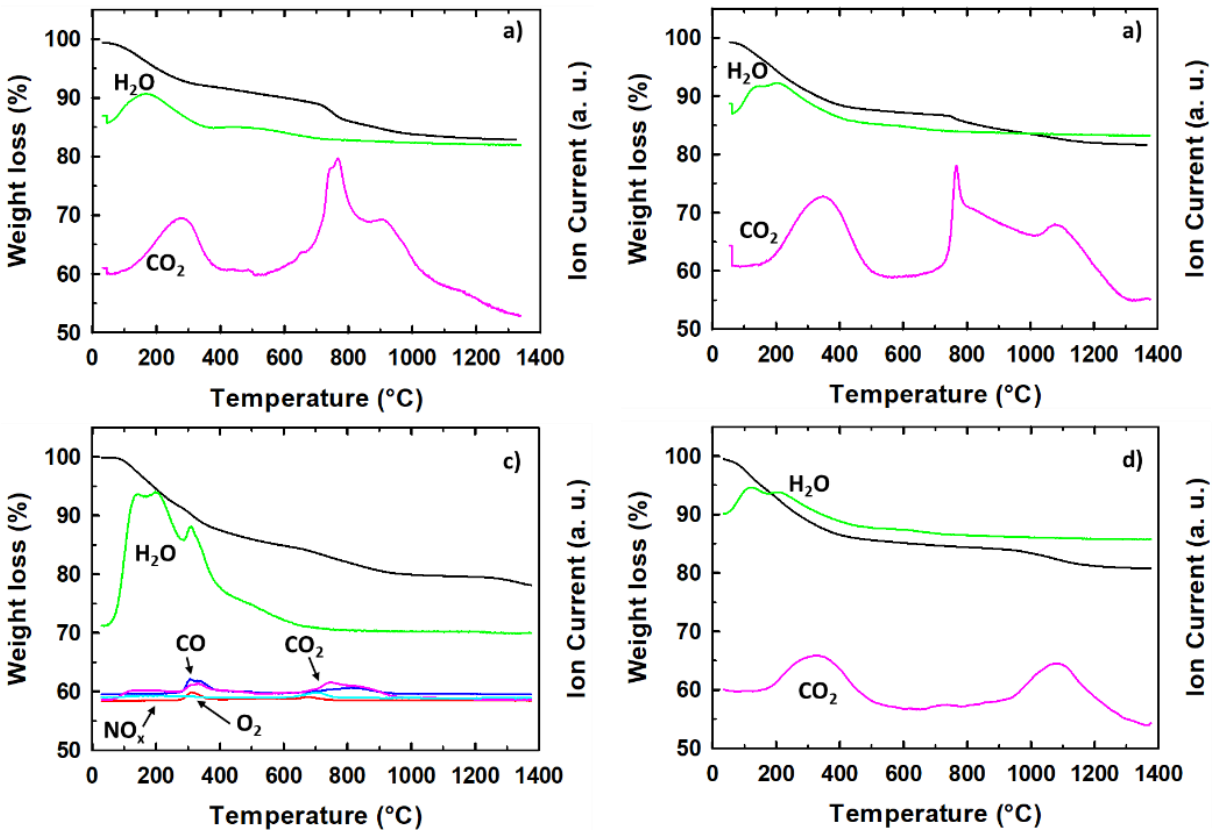

Fig. 4.20. Thermogravimetric analysis (TGA) and mass spectrometry (MS) of the as-prepared LnZP. Comparison of the simultaneous TG signals (black line) and MS signals at m/z: H_2O: 18, CO: 28, O_2: 32, CO_2: 44, and NO_x: 14; 30; 46, Graph a) LZP; b) NZP; c) GZP; and d) DZP [121].

The thermogravimetric results of the LnZX are depicted in **Fig. 4.21**. All the xerogel samples follow similar behavior. The release of adsorbed H_2O was shown as an endothermic peak with a maximum of around 123 °C. Subsequently, a broad exothermic peak was displayed from 400 to 600 °C which results in a weight change of 15.8, 8.8, 8.4, and 8 %wt. for LZX, NZX, GZX, and DZX, respectively. These energetic processes are directly correlated with the degradation of nitrates and residual carbonate intermediate compounds from the synthesis procedure, as confirmed by the presence of CO, CO_2 and NO_x in the MS plots (**Fig. 4.22**).

In general, the xerogels showed a considerably higher amount of organic compounds, this is because all the samples were analyzed as obtained without any additional process, and due to the synthetic method, the xerogels were only dried at room temperature while the powders have a stage of washing with distilled water as described in **section 3**.

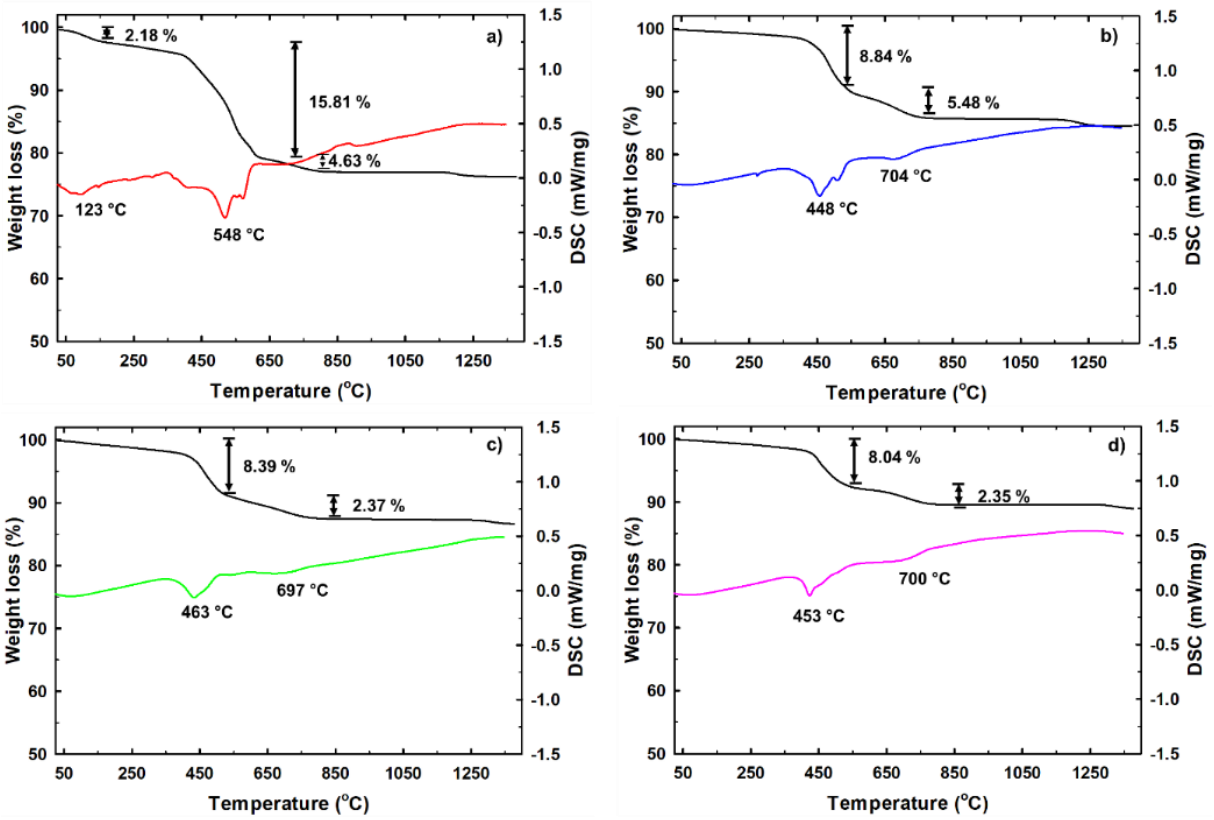

Fig. 4.21. DSC/TGA patterns (from 25 to 1400 °C) of the as-obtained $Ln_2Zr_2O_7$ xerogels; a) $La_2Zr_2O_7$; b) $Nd_2Zr_2O_7$; c) $Gd_2Zr_2O_7$; and d) $Dy_2Zr_2O_7$ [121].

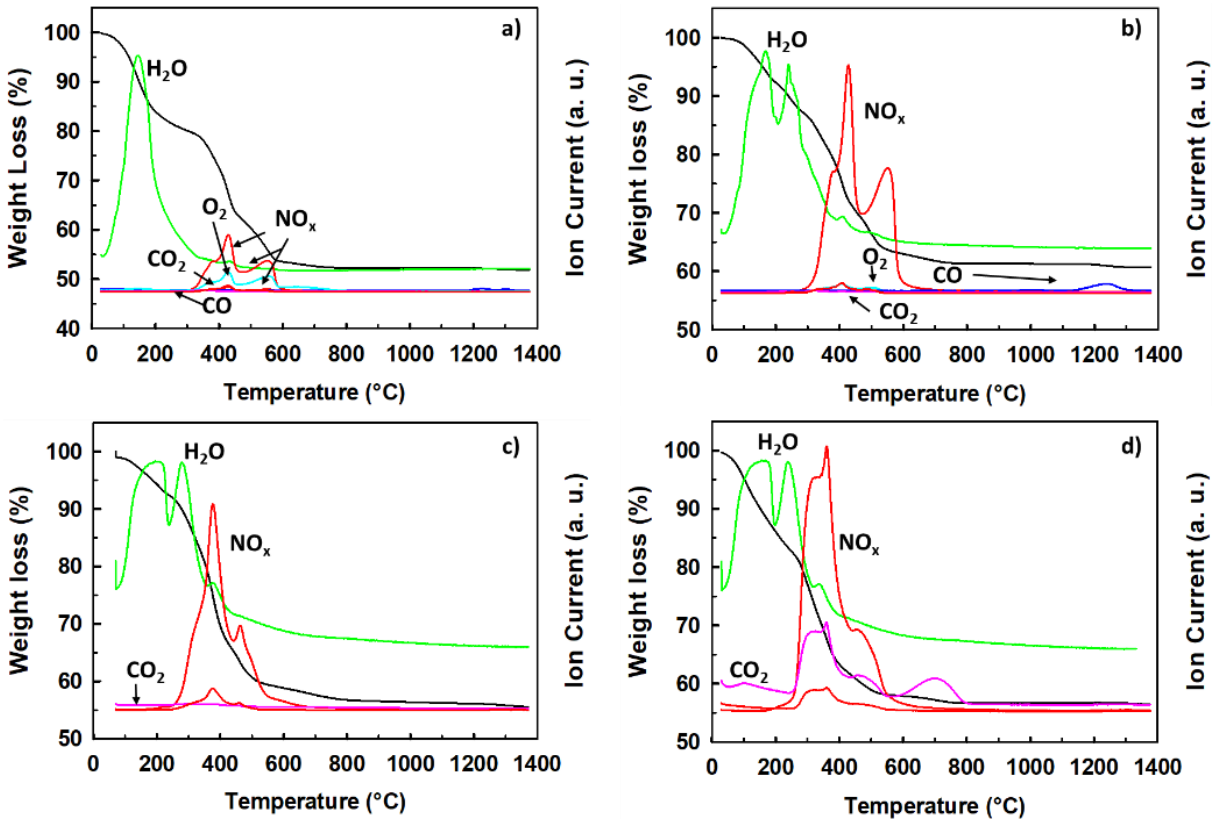

Fig. 4.22. Thermogravimetric analysis (TGA) and mass spectrometry (MS) of the as-prepared LnZX. Comparison of the simultaneous TG signals (black line) and MS signals at m/z: H_2O: 18, CO: 28, O_2: 32, CO_2: 44, and NO_x: 14; 30; 46, Graph a) LZX; b) NZX; c) GZX; and d) DZX [121].

In the case of the LnZA samples, the desorption of H_2O was located from 110 °C up to 140 °C (**Fig. 4.23** and **Fig. 4.24**) and is associated with a weight loss of 15, 10.9, 13.1, and 9.4 %wt. for LZA, NZA, GZA, and DZA respectively. In this case, the combustion of organic compounds is displayed as a broad exothermic event which takes place between 150 °C to 400 °C. At this range, two maximums were observed ranging between 221-237 °C and 330-344 °C. From the MS data, the first peak was related to the fast elimination of acetone (showed as CO and CO_2 in the MS curve) form the surface together with residual H_2O. The second maximum is due to the thermal degradation of leftover compounds from the synthesis such as HNO_3, 1-propanol, etc. which are displayed as NO_x, CO, CO_2, and O_2 in the MS plots. This exothermic process leads to a mass loss of 21, 16, 15.7 and 15.1% for LZA, DZA, GZA, and DZA, respectively. Then, a sharp exothermic peak is present at 645, 588, 552, and 527 °C for LZA, NZA, GZA, and DZA respectively. These isolated events are associated with the crystallization transition of all the aerogel samples. As can be seen, there is a

decreasing trend in the crystallization temperature as the atomic number of the incorporated Ln^{3+} ion increases which is attributed to the size and nature of the lanthanide element [10,136,137].

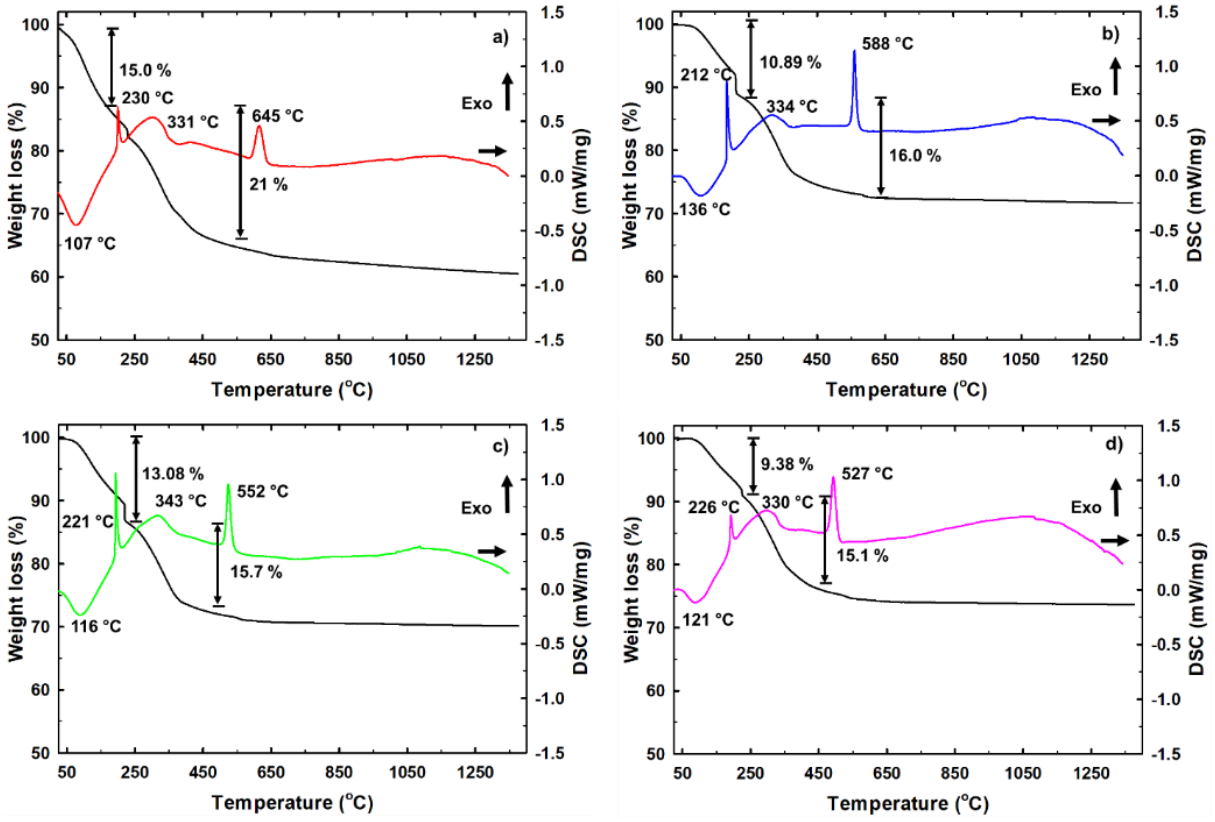

Fig. 4.23. TGA/DSC patterns recorder from room temperature to 1400 °C of the as-obtained $Ln_2Zr_2O_7$ aerogels; a) $La_2Zr_2O_7$; b) $Nd_2Zr_2O_7$; c) $Gd_2Zr_2O_7$, and d) $Dy_2Zr_2O_7$ [121].

In comparison with the ZrO_2 and YSZ aerogels described in **section 4.2**, the LnZA has a substantial increment in the crystallization temperature. Namely, the rare-earth-free ZrO_2 has a value of 419 °C, while adding of Y^{3+} to the structure increased the crystallization up to 455 °C. On the other hand, in addition to crystallizing directly from amorphous to cubic phase, LZ aerogels have much higher crystallization temperatures of up to >220 °C (e.g. LZA has a value of 645 °C while ZrO_2 419 °C or YSZ 455 °C).

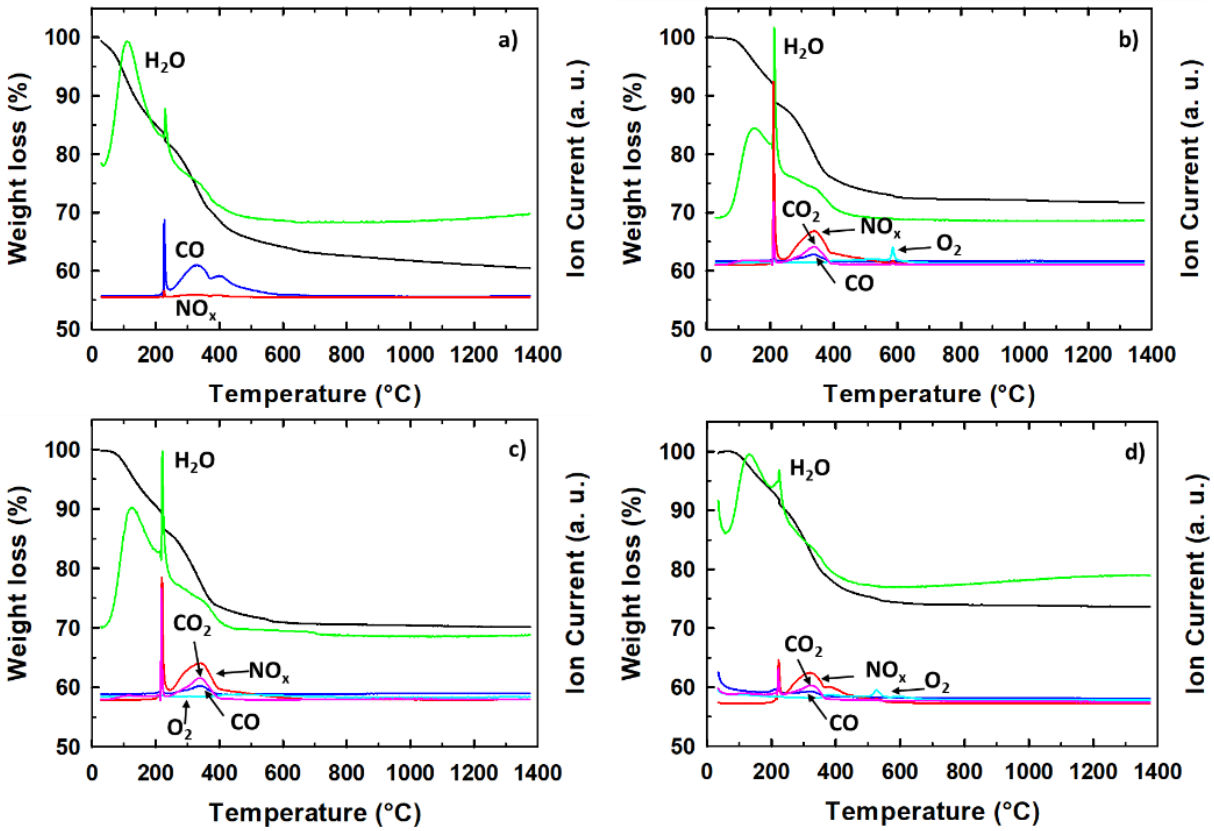

Fig. 4.24. Thermogravimetric analysis (TGA) and mass spectrometry (MS) of the as-prepared LnZA. Comparison of the simultaneous TG signals (black line) and MS signals at m/z: H_2O: 18, CO: 28, O_2: 32, CO_2: 44, and NO_x: 14; 30; 46, Graph a) LZP; b) NZP; c) GZP; and d) DZP [121].

For high-temperature coatings applications, the microstructural changes upon heat treatment are important. Thus, to study the temperature effect on the surface morphology of the materials, scanning electron microscopy (SEM) was carried out on the calcined samples at 1000 °C / 5hrs (**Fig. 4.25**). As can be seen in **Fig. 4.25a**, the LnZP are formed by a dense surface of grain sizes of ~100 nm with a random orientation. These grains build a larger microstructure with several aggregates where few amount of micropores are apparent. Note that all the powders revealed similar arrangements thus the morphology is unaffected to the lanthanide ion present in the nanostructure (Appendix A). On the other hand, the xerogels (**Fig. 4.25b**) are composed of spherical particles of ~100 nm. These aggregated particles are roughly consolidated upon calcination. However, despite the consolidation, a highly porous material was obtained in comparison with LnZP. Interestingly, despite the calcination, the aerogels showed the typical morphology of this type of material, which is built by aggregated spherical particles (~ 70 nm) with large extent of open porosity, distributed along the surface

(**Fig. 4.25c**). Contrary to the xerogels, the aerogels do not show any consolidation of the particles/aggregates that demonstrates excellent resistance upon thermal sintering. The main difference between these three morphologies is in the used method of synthesis. In the case of powders, dense particles grow and precipitate in a liquid medium, while materials prepared by sol-gel (e.g. xerogels and aerogels), are naturally porous at an intermediate stage of preparation (wet gel) and the drying process determines the final porosity of the material.

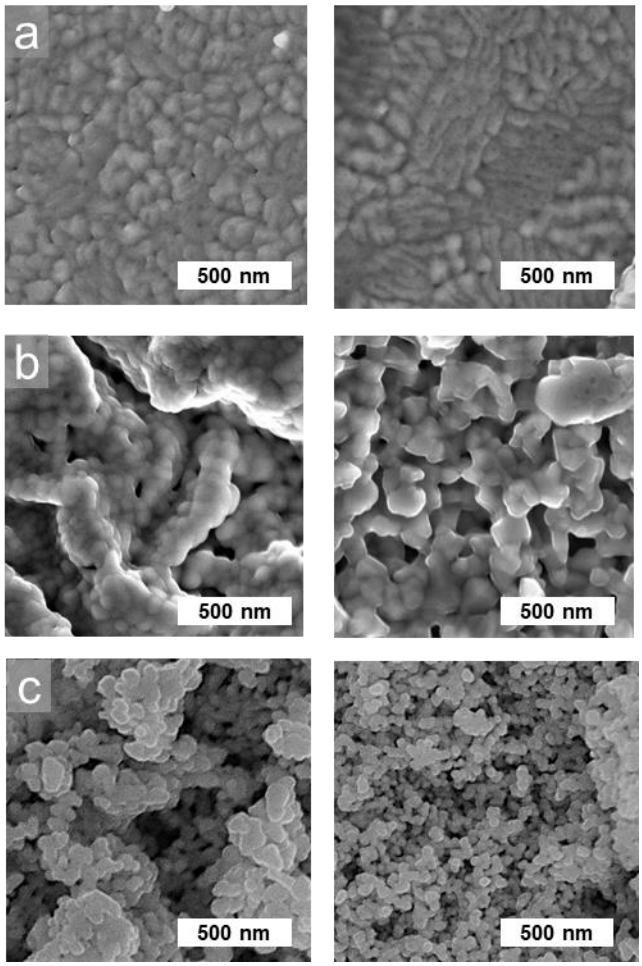

Fig. 4.25. Scanning electron microscopy: Surface morphology of the calcined $La_2Zr_2O_7$ and $Gd_2Zr_2O_7$ powders (LnZP) (a), xerogels (LnZX) (b) and aerogels (LnZA) (c) at 1000 °C/5h. Additional SEM pictures are shown in Appendix A [121].

The porosity and specific surface area of the LnZP, LnZX, and LnZA materials were investigated by means of N_2 adsorption measurements upon calcination at 1000 °C / 5hrs. The isotherms of the LnZP are of type III according to the International Union of Pure and

Applied Chemistry (IUPAC) [110] in which no inflection point was detected and therefore no clearly distinguishable monolayer and multilayer formation of nitrogen (**Fig. 4.26**). This is because the apparent porosity is due to the interparticle unions rather than porosity of the bulk material as can be seen in the micrograph (**Fig. 4.25a**). Therefore, such analysis was not relevant. On the other hand, the obtained isotherms of the LnZX samples (type I(b) with the absence of hysteresis) revealed that the xerogels are composed of mostly micropores (d < 2nm) as can be seen in **Fig. 4.26b**.

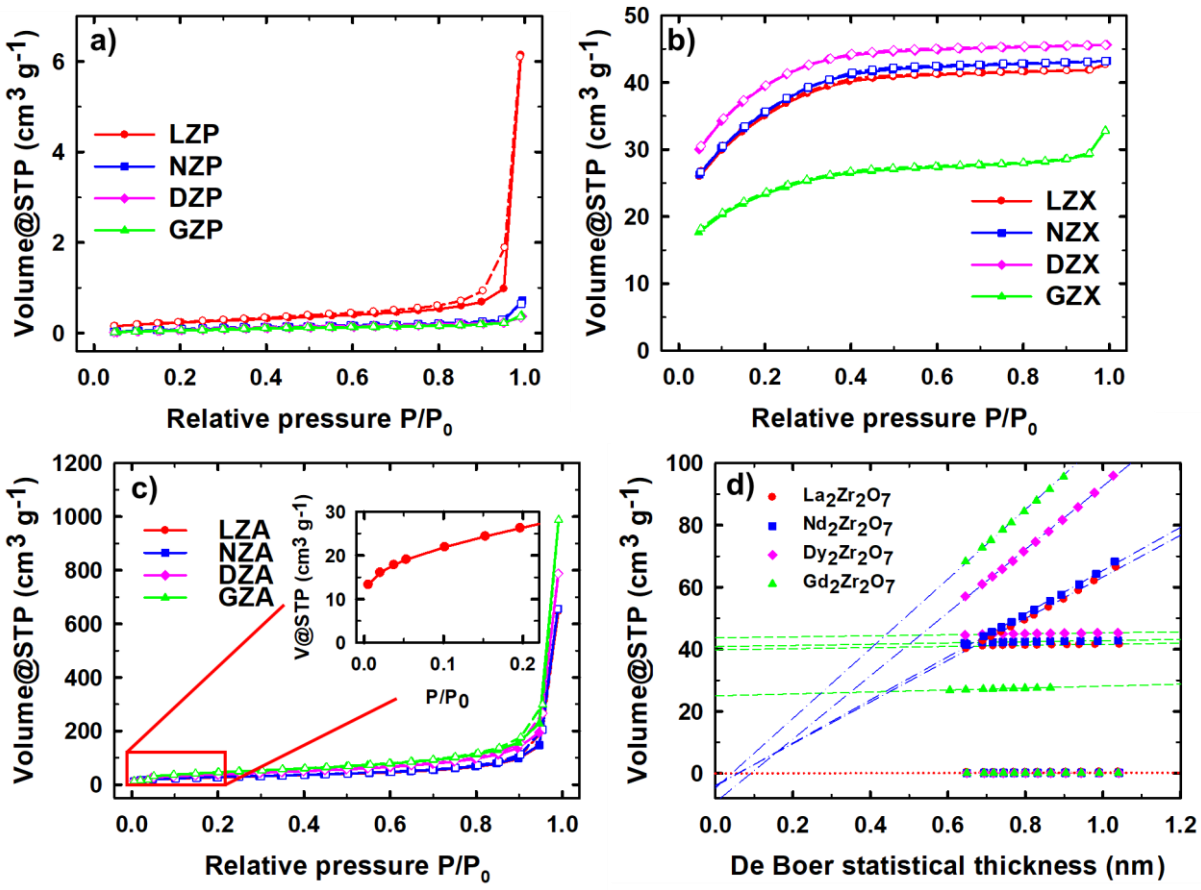

Fig. 4.26. Nitrogen adsorption-desorption isotherms of a) powders; b) xerogels; and c) aerogels. Inset: magnification of the $La_2Zr_2O_7$ aerogel adsorption isotherm at low relative pressures; d) V-t plot of all $Ln_2Zr_2O_7$ materials reported herein used for determination of the microporosity, the red, green, and blue lines are for powders, xerogels, and aerogels, respectively [121].

The LnZA isotherms are displayed in **Fig. 4.26c**. The aerogels are distinguished by type II isotherms and with small adsorbed nitrogen volume at low relative pressure values (P/P_0) and with practically no hysteresis loop as can be seen in the inset of the **Fig. 4.26c**. As can

be seen, the LnZA samples adsorbed roughly 20 times more nitrogen than LnZX samples and more than 150 times than the LnZP. This is the result of the significantly larger pore volume of LnZA (**Table 4.9**). The specific surface areas (S_{BET}) are summarized in **Table 4.9**. In general, the materials with the largest surface areas are the LnZX and LnZA, specifically, the DZX and GZA with values of 144 and 168 m^2g^{-1} respectively, whereas the LnZP showed to be quite dense materials with surface areas < $1m^2g^{-1}$. In comparison with the previously reported S_{BET} for LZ materials, the values herein reported are smaller [117,138,139]. However, the values reported in **Table 4.5** for the ZrO_2 and YSZ aerogels (in the order of 80-114 m^2g^{-1}), are somewhat comparable with surface areas of around 100-139 m^2g^{-1} of those of the LnZA.

Table 4.9. Summary of N_2 sorption analysis of calcined samples [121].

Sample	S_{BET} (m^2g^{-1})	C value	Micropore		Pore diameter		Total pore
			area (m^2g^{-1})	volume (cm^3g^{-1})	average (nm)	characteristic* (nm)	volume (cm^3g^{-1})
LZP	0.9	42 ± 4	0.2	0.000	-	-	0.010
NZP	0.3	12 ± 1	0.1	0.000	-	-	0.001
GZP	0.3	7 ± 1	0.1	0.000	-	-	0.001
DZP	0.4	5 ± 2	0.1	0.000	-	-	0.001
LZX	124 ± 18	162 ± 16	121	0.062	2.1	1.7	0.066
NZX	129 ± 19	111 ± 10	126	0.063	2.1	1.7	0.067
GZX	85 ± 12	129 ± 13	80	0.039	2.4	1.7	0.051
DZX	144 ± 19	128	142	0.068	2.0	1.7	0.071
LZA	100 ± 10	89 ± 8	-	-	40.0	120	1.0
NZA	102 ± 11	103 ± 9	-	-	39.9	110	1.02
GZA	168 ± 16	66 ± 6	-	-	36.5	131	1.53
DZA	139 ± 14	74 ± 6	-	-	35.2	119	1.22

* Characteristic pore diameter: estimated at the maximum of the distribution curve

Even, it can be considered again that the LnZA have a better resistance against the consolidation of the particles (and shrinkage) since the ZrO_2/YSZ were calcined at 500 °C for 2 hours and those of LZ at 1000 °C for 5 hours thus being treated at a much higher temperature and for longer time leading to no densification of the LnZA – also supported by the SEM images in **Fig. 4.25** – as it happened with those of ZrO_2 and YSZ (for those samples no significant values were reported after calcination at 1200 °C due to large densification; **Fig. 4.5** and **Table 4.6**).

Notwithstanding the aerogels presented the largest S_{BET} values, the xerogels adsorbed the higher portion of nitrogen. This might be indicative that the xerogel materials have greater adsorption enthalpies as revealed by the higher *C* constant values than those for aerogels. The *C*-constant is associated with the affinity of the interaction between adsorbent and adsorbate [140] and the presence of microporosity [140,141]. From the *V-t* plots (**Fig. 4.26d**) can be noticed that xerogels have positive intercepts (green regression lines) with the axis of adsorbed N_2 volume that recognizes the presence of microporosity while the aerogels (blue regression lines) have nearly zero intercepts. Therefore, these results suggest that the quantification of the S_{BET} of xerogels is mainly consequence of high micropore area (**Table 4.9**). The pore size distributions of the LnZX and LnZA are presented in **Fig. 4.27**.

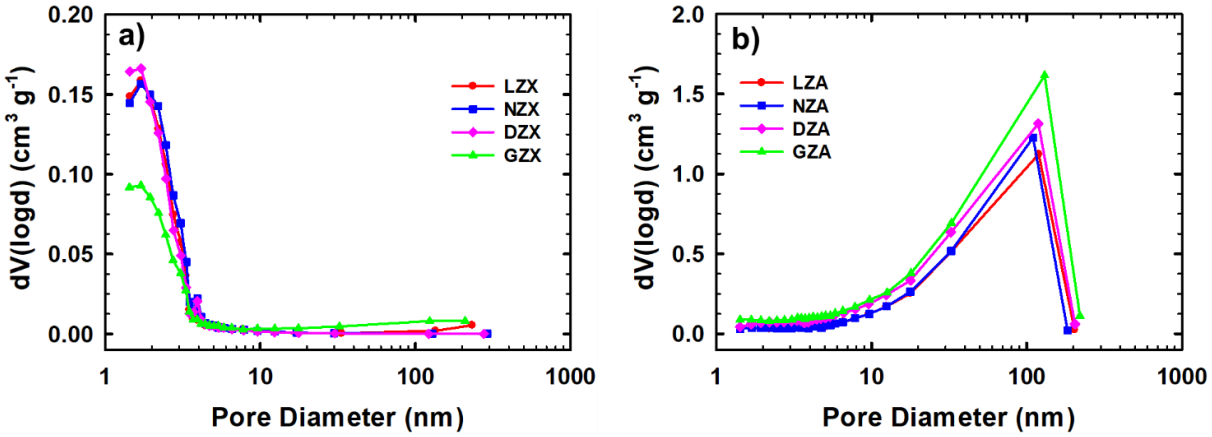

Fig. 4.27. Pore size distributions of a) xerogels indicative of narrow microporosity and b) aerogels indicative of broad meso- and macro-porosity [121].

From the pore size distribution graphs, it is clear that the porosity of the xerogels is very narrow ranging between 1 to 4 nm with an average of ca. 2 nm. The aerogel samples, on the contrary, demonstrated wider pore size distributions with pore sizes between 8 and 250 nm with an average pore size ranging 35-40 nm. Overall, the porosity of ZrO_2/YSZ aerogels is similar to that of the LnZA aerogels. Although there is a significant variation in the characteristic pore diameter, specifically, the LnZA aerogels have up to 3 times higher pore diameter than the ZrO_2/YSZ, coupled with similar pore volume (1.6 vs 1 cm^3g^{-1} for YSZ and LZ, respectively), suggests that the LnZA have very elongated pores in comparison at ZrO_2/YSZ.

The adaptability of the synthesis method optimized to prepare Zr-based aerogels was validated in terms of obtaining high purity materials such as in this case aerogels and xerogels with $Ln_2Zr_2O_7$ structure. The physicochemical properties and crystallinity of the synthesized materials are highly dependent on the synthetic protocol. The co-precipitation method resulted in highly densified materials with surface areas below 1 m^2g^{-1} while the sol-gel yield highly porous networks built by aggregates of nanoparticles with high specific surface area in the order of 130 $m^2\ g^{-1}$ upon calcination at 1000 °C / 5hrs. Those values are larger than the ZrO_2 and YSZ aerogels that after calcination process experimented high densification that resulted in a dramatic drop of their specific surface area (below 1 $m^2\ g^{-1}$). Such calcination process developed the evolution of $Ln_2Zr_2O_7$ structure with either ordered pyrochlore structure (LZP, NZP, LZX, NZX), and disordered fluorite (GZP, DZP, GZX, and DZX). On the other hand, the aerogels are mainly composed of $Ln_2Zr_2O_7$ structure with traces of t-ZrO_2. As comparison, a mixture of m-ZrO_2/t-ZrO_2 and t-ZrO_2 constituted the ZrO_2 and YSZ aerogels, respectively.

4.4. Preparation of aerogel-based coatings by soft chemistry deposition techniques

In this section, different deposition techniques of aerogels which includes doctor-blade, dip-coating, and a variant called slurry dip-coating are described.

4.4.1. Doctor-blade: tape casting

In a typical experiment, a strip of adhesive tape was applied on the edges of the substrate to form a cavity with an area of 20x20 mm. Then, to control the coating thickness, 50 or 100 μL of freshly produced YSZ sol (**Section 4**) were instantly deposited into the cavity using a micropipette. This process was carried out at room temperature and eventually, the sol became a wet gel in the form of a coating between 125 and 250 μm. Immediately after gelation, the coated substrates were transferred to a container with 1-propanol and aged for 24 hrs. Then the wet gel coatings were immersed into a solution containing a 1-propanol/acetone mixture (volume ratio, 3 : 1; exchanged to 1 : 1, 1 : 3, and 0 : 3 every 24 hrs). Throughout the aging process, the coatings were fracture-free and without apparent shrinkage. Finally, the wet gel coatings were supercritically dried using CO_2.

Some changes were made in order to perform the supercritical drying of the coatings due to when the samples were placed parallel to the base (**Fig. 4.28a**), the CO_2 collided with the substrate causing the coating deformation and therefore a total detachment occurred (**Fig. 4.28b**). To counteract this, the samples were placed vertically with respect to the base (**Fig. 4.28c**), so that the coated part was parallel to the CO_2 path and allowed its flow through the gel during extraction avoiding the deformation. The maximum drying temperature was 45 °C and 100 bar of pressure. The detailed drying process can be found in **Section 3**.

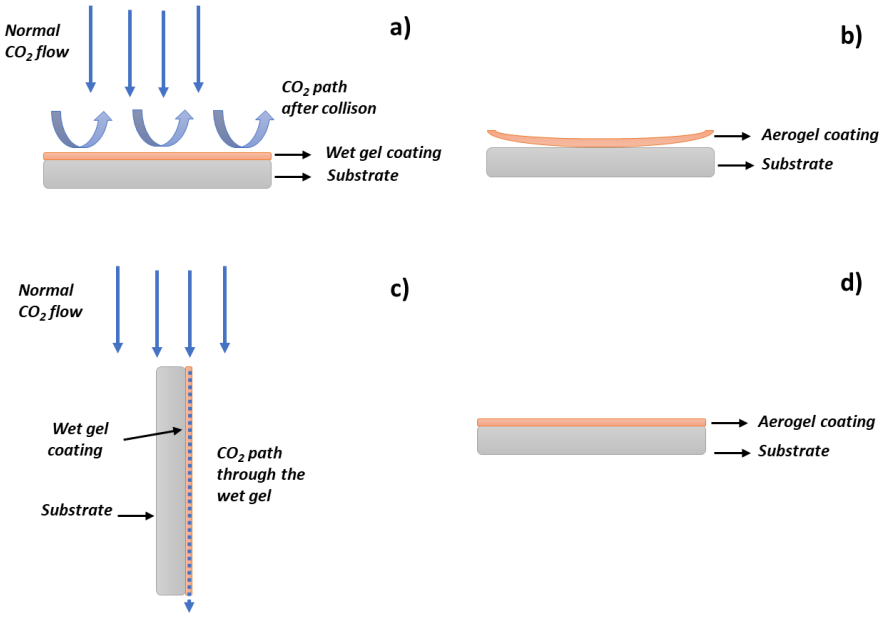

Fig. 4.28. Schematic representation of the placement of the coatings during the supercritical drying process. (a) coating set perpendicular to the CO_2 path, (b) obtained aerogel coating when placed in a vertical position, (c) coating set in parallel to the CO_2 path, (d) obtained aerogel coating when placed in parallel position.

In these series of samples, the thickness of the coating was varied by the dropped volume of sol onto the substrate: low thickness samples were prepared dropping 125 μL (hereafter 125YSZ) and thicker samples with 250 μL (250YSZ).

From macroscopic observations (**Fig. 4.29b**), is visible a thin white aerogel coating which is covering a large part of the substrate surface with exception of the edges (125YSZ), whereas the thicker coating is entirely fractured and greater uncoated surface is exposed (250YSZ). In the SEM images are noticed fragmented pieces of aerogel that are barely coating the surface with large non-coated portions (**Fig. 4.29c, f**). On the contrary, the

substrate in the 125YSZ sample is almost fully covered (**Fig. 4.29e**), although there is some detachment on the edges. Cracks of some tens of microns are propagated on the coating.

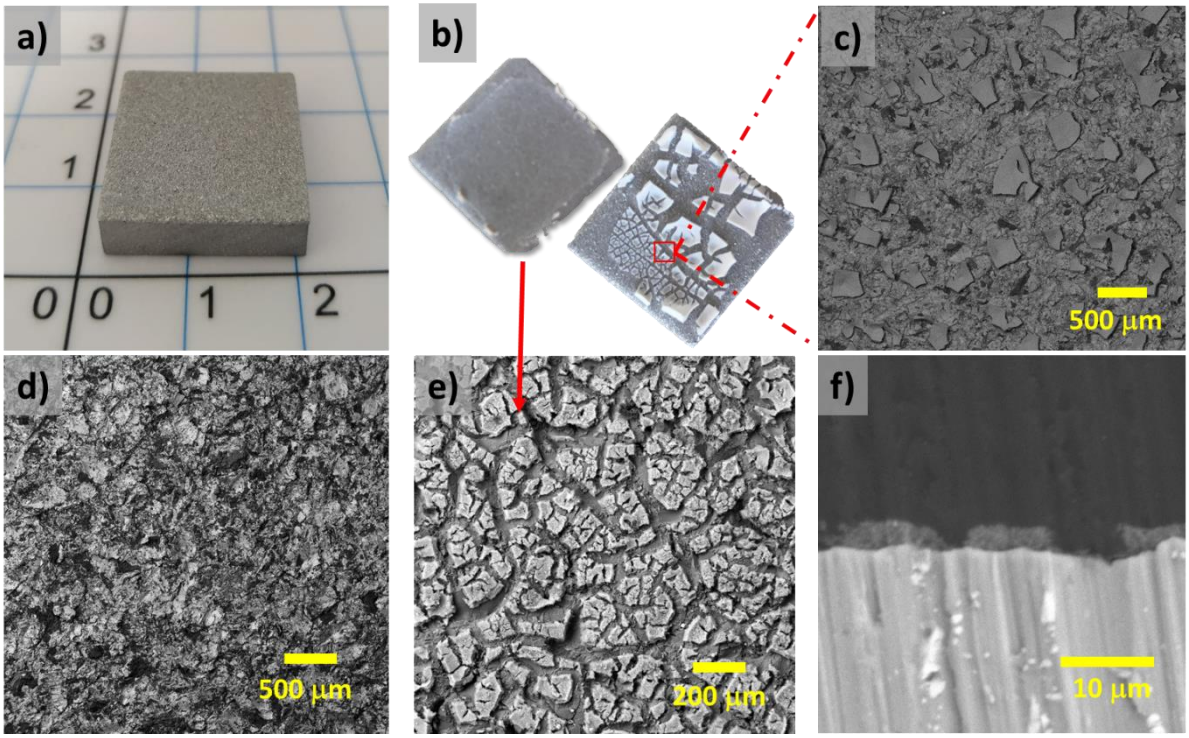

Fig. 4.29. Surface morphology of the doctor-blade coatings; a) square aluminum grit blasted substrate before deposition; b) 125YSZ (upper left), 250YSZ (down right); c) surface morphology of the 250YSZ sample; e) surface morphology of the 150YSZ sample; f) cross-section of the 150YSZ sample.

Both, the spallation on the edges, and the presence of cracks are related to the irreversible shrinkage of aerogels which takes place during the CO_2 extraction. Directly upon supercritical drying, the aerogel coatings shrunk ~30 % and ~10 % for 250YSZ and 125YSZ respectively. It has been reported that when the aerogel coating is adhered to the surface, upon shrinkage, tensile stress is generated. If this stress is larger than the tensile strength of the material, is released in form of cracks (**Fig. 4.30**) [142,143]. The tensile stress during drying is directly proportional to the film thickness and viscosity. Namely, stress tends to be greater when the coating is thick since the shrinkage is larger. In this case, the thickest sample (250YSZ) presented major fractures even is completely detached from the surface. On the other hand, although in the thin sample (125YSZ) the cracks are dispersed on the substrate, and the total detachment did not occur.

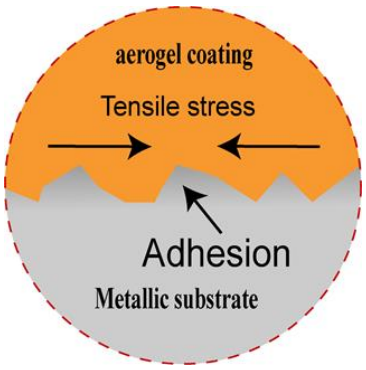

Fig. 4.30. Generated tensile stress produced during the aerogel coating shrinkage.

Several studies have shown that some of the drawbacks of sol-gel coatings on both metal and glass substrates are the cracking, low thickness limits, and the drying process that generates cracks. Such cracks are more frequent in thick coatings (above 30 microns) because the critical thickness is exceeded. For instance, He *et.al.* [77] prepared SiO_2 crack-free aerogel films of 2 - 3.6 μm on FTO substrates by the tape doctor-blade method. In a recent study, Saem *et.al.* [144] developed a technique to prepare aerogel coatings of tunable thickness ranging between 3 μm and < 100 μm in either glass or flexible or polymeric substrates. Crack-free thin silica coatings have been obtained below 200 nm on glass and ITO substrates [145].

4.2.2. Dip-coating: sol approach

These coatings were prepared by dipping the substrate into a sol and then vertically removed. Coatings were obtained using solutions at different aging times due the viscosity increase with the aging [146,147]. Thus, the substrates were dipped after 1 and 2.5 minutes after sol preparation. Once the deposited sol layer became a gel, the wet gel coatings were immediately submitted to the standard soaking and subsequent supercritical drying processes described in **Section 3**.

It can be seen that there is an enormous difference in the surface of the coating obtained at a short aging time (**Fig. 4.31a**) with respect to that of a longer aging period (**Fig. 4.31b**). In a short time, the surface is formed by small pieces of aerogel that do not cover the entire surface since they are scattered throughout the substrate.

Fig. 4.31 shows the micrographs of the prepared coatings at different aging times.

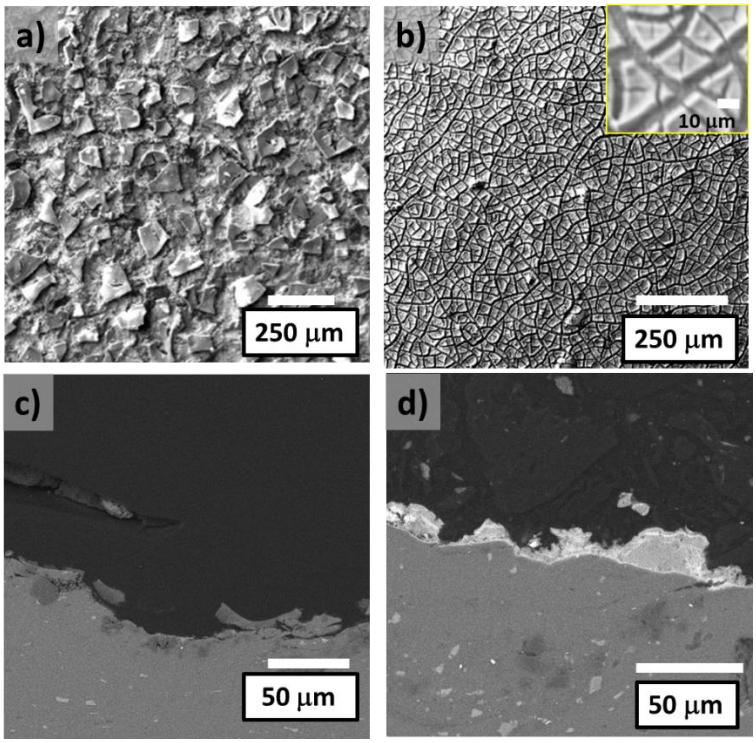

Fig. 4.31. Coatings prepared by the sol-gel coating varying the aging period of the precursor sol; a) surface of the coating after 1 min; b) surface of the coating after 2.5 min; c) cross-section of the coating after 1 min; d) cross-section of the coating after 2.5 min.

In contrast, the surface of the more aged sample is noticeably more homogeneous and the aerogel layer covers most of the substrate. Along the entire surface, several cracks of around 10 µm are observed. Similar to the previous deposition method, these cracks are an effect of the tensile stress generated by the contraction of the coating upon drying. In fact, it can be found in the literature that only very thin coatings below 5 µm are free or cracks. For instance, Wang *et.al.* prepared aerogel coatings of ~142 nm by dip-coating in a solution of SiO_2 aerogel nanoparticles [148]. Others report crack-free multilayer silica aerogel coatings of 5 µm on silicon wafers by the dip-coating method [149]. Innocenzi *et.al.* prepared ZrO_2 coatings of <150 nm on metallic Ni and Al substrates by the dip-coating technique.

4.2.3. Dip-coating: slurry

The samples were prepared on MAR-M-247 Ni-based alloy substrates previously grit blasted and cleaned as described in **section 3.** The depositions were made at room temperature. In this case, the approach was drastically changed since the aerogel was not

synthesized directly on the substrate. Specifically, aerogels of $La_2Zr_2O_7$ were prepared and subsequently ground in an agate mortar to have a fine aerogel powder. Then, to control the particle size, the powder was sieved and only particles below 25 micrometers were used. Although more than > 95 % of the powder generated complied with such particle size.

Table 4.10. Summary of the prepared slurry coatings with lanthanum zirconate aerogel.

Sample	Depositions	Wt.% of aerogel
L1D10	1	10
L2D10	2	10
L3D10	3	10
L1D20	1	20
L2D20	2	20
L3D20	3	20
L1D30	1	30
L2D30	2	30
L3D30	3	30

Then, a slurry composed of different amounts of LZA aerogel powder and its precursor sol was prepared since it is proven that the sol functions as both particle-particle and powder-substrate binder [150]. Finally, the substrates were dipped into the slurry. After each deposition, the coating was dried at 50 °C for 5 min. The studied variables were: the powder loading (10-30% wt.) and the number of deposits (1-3).

Fig. 4.32 shows the surface morphology of the coatings produced with 10 %wt. and different dips. In general, the 10 %wt. slurry produced coatings formed by aerogel aggregates of ~50 μm (**Fig. 4.32a-c**). As the number of deposits increase, a slight coarsening of the surface can be noticed. However, despite the number of depositions, uncoated zones were revealed as blue spots (aluminum) by the EDX images (**Fig. 4.32g-i**). Although the number of depositions progressively enhanced the aerogel coating, non-coated spots are still present even after 3 deposits. This poor performance is due to the low amount of powder dispersed in the slurry used to produce the coating.

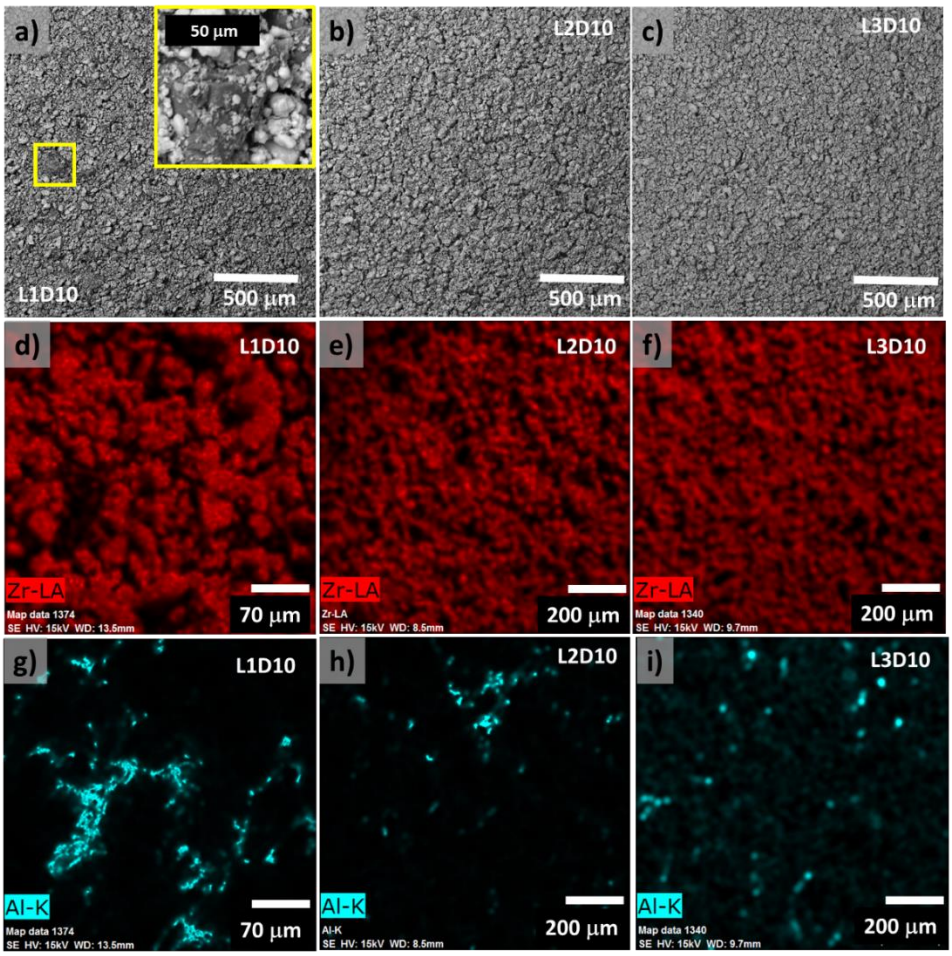

Fig. 4.32. Surface morphology of the produced coatings by the slurry composed of 10% of lanthanum aerogel powder and its former sol; a) L1D10; b) L2D10; c) L3D10; d-i) EDX images of the coatings.

The amount of aerogel on the substrate was significantly improved with the slurry of 20% as can be seen in **Fig. 4.33**. With one deposit, a slightly tortuous surface is observed since the roughness has not been completely filled by the aerogel. These irregularities disappear after the second deposit and improve even more to the third deposit. Slight cracks appear after the second deposit and increase to the third as well as the coarsening of the coating being indicative of the higher amount of aerogel powder. Although there are fewer aluminum spots compared to the samples prepared with 10%, some uncoated spots can still be observed as revealed by the EDX images (**Fig. 4.33g-i**).

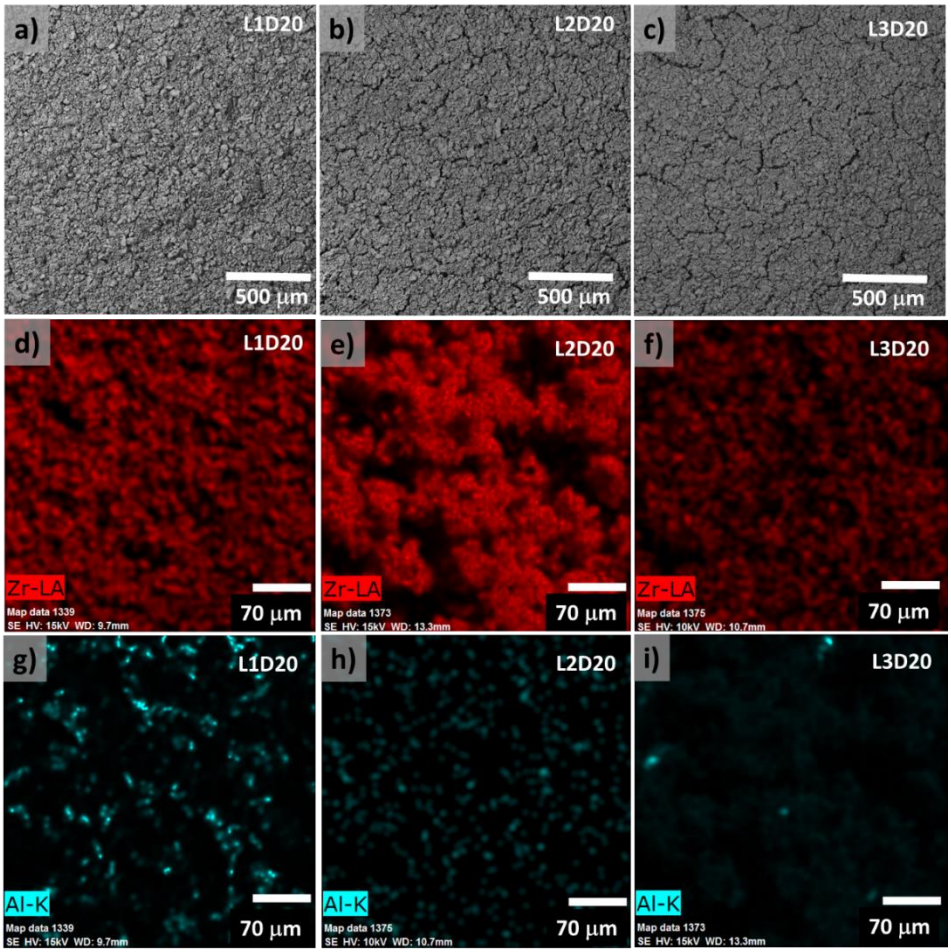

Fig. 4.33. Surface morphology of the produced coatings by the slurry composed of 20% of lanthanum aerogel powder and its former sol; a) L1D20; b) L2D20; c) L3D20; d-i) EDX images of the coatings.

By increasing the amount of powder to 30%, a thick surface formed by aggregates of about 50 µm is obtained from the first deposit (**Fig. 4.34**). Unlike the previous samples of 10 and 20%, in this case, in all the deposits it was possible to cover the entire surface, as corroborated by the EDX images (**Fig. 4.34d-f**).

A common feature in most of the studied samples is the appearance of cracks (so-called "mud cracks" [151]). There are several factors that favor the presence of cracks in slurry-based coatings such as drying speed, drying temperature, solution composition, deposited amount, and particle size, among others [146,151–154]. In general, when coating formed by a colloidal suspension is applied to a dense substrate, during the drying process, the coating contracts due to evaporation of the solvent. Constrained by the solid substrate, this volume reduction generates stress on the coating. If the stress is greater than the strength

of the material, the stress is released in the form of a crack. In this case is attributed to the amount of deposited powder since these cracks were more pronounced as the slurry composition increased as well as the number of deposits.

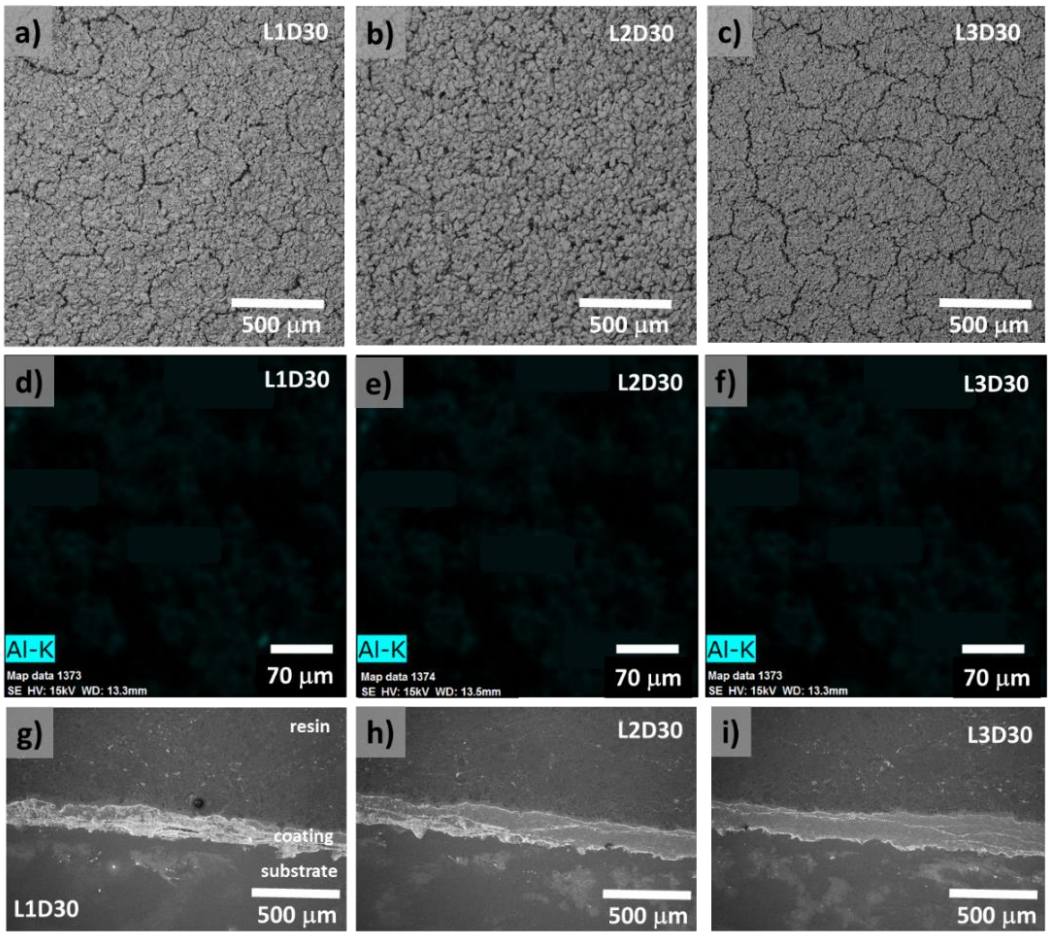

Fig. 4.34. Surface morphology of the produced coatings by the slurry composed of 30% of lanthanum aerogel powder and its former sol; a) L1D30; b) L2D30; c) L3D30; d-f) EDX images of the coatings; g-i) cross-section of the obtained coatings.

From the different studied deposition methods in this work, dip-coating with a slurry formulation of 30% wt. resulted in the most homogeneous and controlled thickness. The high amount of deposited aerogel powder gave an increasing thickness with the number of depositions from ~100 nm at ~250 nm as displayed in **Fig. 4.34g-i**. It is important to highlight that most of the problems that were detected in the deposition methods previously studied such as: detaching, shrinkage, low thickness, cracks segmenting the coating, among others, were eliminated with this approach.

4.2.3.1. Heat treatment effect

Based on the thickness of the coating, the sample L3D30 was selected to reproduce onto a Ni-based superalloy substrate to study possible microstructural changes upon calcination. The heating program was set up to 600, 800, and, 1000 °C with a ramp of 1 °C / min^{-1} and dwell time of 30 min. **Fig. 4.35** shows the scanning electron images after calcination at 600 °C (600L3D), 800 °C (800L3D), and 1000 °C (1000L3D).

Post calcination, new and more marked cracks appeared. The most affected sample was the one treated at 1000 °C. However, the aggregates that build the coating did not reveal changes in the entire temperature range. Even, as can be seen in **Fig. 4.35h**, after the heat treatment at 1000 °C, the aerogel retains its highly porous structure. As in the bulk sample, the coating preserves the porosity which corroborates the great resistance to sintering. However, unlike the aerogels in bulk form, despite the heat treatment, the coatings did not apparently reveal signs of massive shrinkage as can be seen in **Fig. 4.35c-inset**.

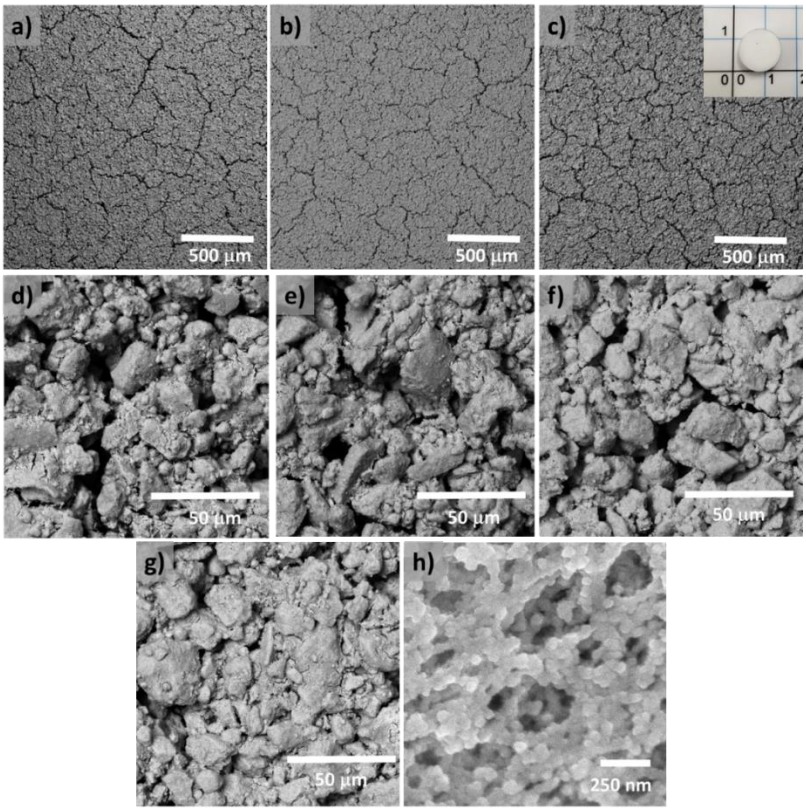

Fig. 4.35. Surface morphology of the L3D30 coating submitted to different calcination temperatures. a) 600L3D; b) 800L3D; c) 1000L3D; d-f) higher magnification detail of the coatings; g) detail of the L3D30 before calcination; h) detail of the 1000L3D coating.

Fig. 4.36 shows the diffractograms of the calcined coatings along with the pattern of the precursor aerogel powder crystallized at 1000 °C / 5hrs. The pattern of the coating treated at 600 °C revealed mostly an amorphous structure with a sign of crystallization. Such crystallization temperature is in agreement with that one of the bulk $La_2Zr_2O_7$ aerogel (crystallization starts at ~600 °C, **Fig. 4.23**). Upon calcination, the broad peaks tend to be more defined until very narrow peaks form the diffraction pattern at 1000 °C corresponding to the $La_2Zr_2O_7$ structure. Similar narrowing phenomena occurred in the bulk aerogel samples as effect of the crystallite size growth.

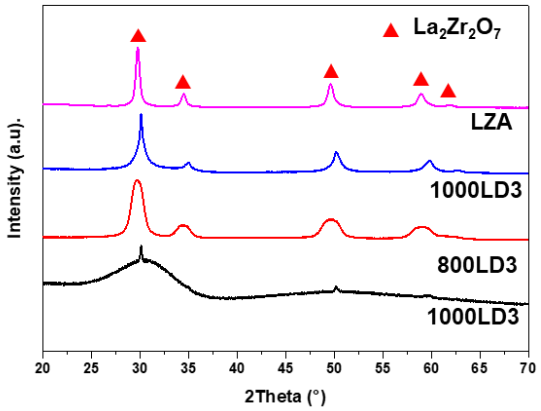

Fig. 4.36. XRD patterns of the calcined coatings.

4.2.3.2. Furnace cycling oxidation test: coating performance under simulated operating conditions

High-temperature coatings (i.e. TBCs) are constantly subjected to long heating-cooling cycles. For this test, two coated substrates (L2D30 and L3D30) were subjected to successive heating-cooling cycles into a furnace. The top temperature was set at 1100 °C / 60 min and quenched at the room temperature. Upon cooling down, the samples were visually examined to detect any possible variation. **Fig. 4.37** shows digital pictures of coated substrates after exposition to 1 and up to 4 cycles (**Fig. 4.37a-e**), low magnification SEM images after 4 cycles (**Fig. 4.37f-g**), expelled region as the boundary coating-substrate (**Fig. 4.37h**), and high magnification SEM images after 4 cycles. Both samples showed similar behavior. From the macroscopic images is clearly visible that a progressive detachment occurs with the heating-cooling cycles, mostly all the coating has detached out from the substrate after 4 cycles.

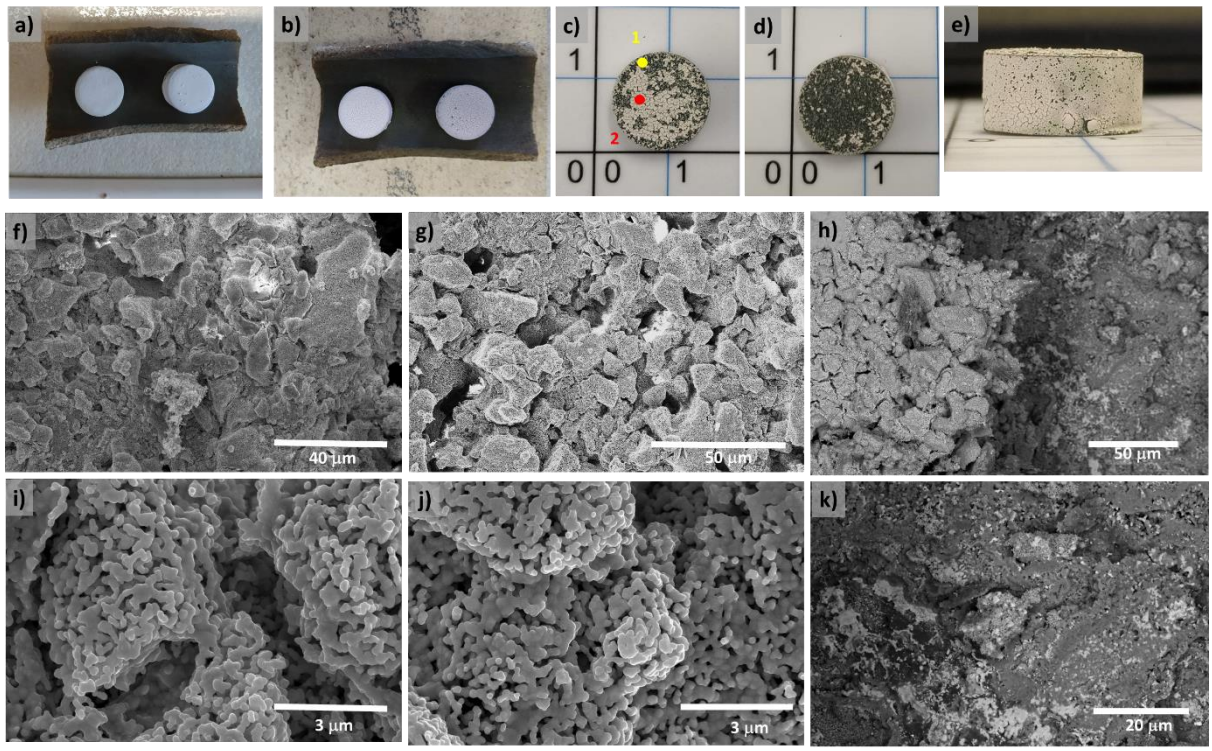

Fig. 4.37. Macroscopic and microscopic images of the L3D30 coatings after 4 heating-cooling cycles at 1100 °C. a-d) Digital photos of the coatings after 1, 2, 3, and 4 cycles, respectively; e) side view of the coating; f-g) low magnification of the L2D30 and L3D30 coatings, respectively; h) aerogel-substrate interface; i-j) high magnification images of the L2D30 and L3D30 coatings, respectively; k) oxide growth. All SEM images were taken after 4 cycles.

Coarsening of the surface coating occurs upon exposition to heating-cooling cycling as revealed by the SEM images. Namely, there is a sintering process producing larger and denser aggregates at the macroscopic level (**Fig. 4.37f-g**). Nonetheless, although sintering of the nanoparticles, the aggregates are highly porous as can be appreciated in **Fig. 4.37i-j**. For porous coatings, this result is very important. Despite the high-temperature treatment, the $La_2Zr_2O_7$ aerogel coating has an enhanced resistance to densification. LZ aerogels proved to maintain the characteristic porous structure of these materials. In addition, in the failure zone are visible some traces of aerogel adhered and the growth oxide layer in light gray as effect of exposure of the metallic substrate to the oxidizing environment.

5. Conclusion

In this thesis, a systematic study of the physicochemical properties of Zr-based aerogels was carried out. Namely, the synthesis, calcination process, type of aerogel and deposition, must be carefully considered for high-temperature coatings applications. To this purpose, ZrO_2, YSZ, and $Ln_2Zr_2O_7$ (Ln=La^{3+}, Nd^{3+}, Gd^{3+}, and Dy^{3+}) aerogels were successfully synthesized. Throughout the experimental work done can be concluded the following points:

1) A simplified synthetic route allowed obtaining high-purity aerogel materials was found. When zirconium propoxide is involved, the water concentration plays a determinant role in the sol-gel reactions. The incorporation of a disproportionate amount of water can lead to the formation of precipitates or to the development of secondary phases in the final product.
2) According to the proposed reaction mechanism, nitric acid is determinant to control the sol-gel reactions. Insufficient acid results in the partial hydrolysis of the propoxy groups and therefore uncontrolled precipitation occurs. The adequate HNO_3 concentration drives the hydrolysis/condensation reactions to form a free-precipitate wet gel in a few minutes while oversaturation caused complete inhibition of the gelation.
3) By means of the tunable synthesis method, it was possible to prepare either pure ZrO_2, rare-earth-doped aerogels such as YSZ, or 4 new compositions of rare-earth zirconates in the form of aerogels and xerogels such as $La_2Zr_2O_7$, $Nd_2Zr_2O_7$, $Gd_2Zr_2O_7$, and $Dy_2Zr_2O_7$.
4) The calcination has a great impact on the physicochemical properties of the aerogels. Upon calcination, the ZrO_2 and YSZ suffer from almost complete densification losing their porosity in its totality. On the other hand, the $Ln_2Zr_2O_7$ aerogels retain high surface areas at similar calcination conditions.
5) The phase composition varied regarding the material. The ZrO_2 aerogel firstly crystallizes to tetragonal followed by a complex phase transformation pathway determined by the crystallite size in a range of temperatures. In general, excellent phase stability resulted when a trivalent rare-earth ion (Ln^{3+}) which was added to the zirconium oxide structure. Namely, the YSZ experimented an

amorphous-to-tetragonal phase transition was found stable from room temperature up to 1200 °C. The phase composition of the $Ln_2Zr_2O_7$ materials is highly dependent on the synthesis and the incorporated rare-earth element. Specifically, regarding the powders (co-precipitation) and xerogels (sol-gel) yielding single-phase pyrochlore ($La_2Zr_2O_7$ and $Nd_2Zr_2O_7$) or fluorite ($Gd_2Zr_2O_7$, $Dy_2Zr_2O_7$) cubic phases. The new system of rare-earth zirconate aerogels resulted in a mixture of $Ln_2Zr_2O_7$ and traces of tetragonal phases. All these phases were stable in studied temperature range up to 1200 °C.

6) The deposition of aerogels as a coating by soft chemistry routes must be performed under strictly controlled conditions. The direct formation of a wet gel onto the substrate surface suffers from extensive shrinkage upon supercritical drying. The combination of shrinkage and adhesion of the aerogel causes tensile stress that yields cracking and detachment of the deposited coating. The magnitude of these stresses seems larger in thick coatings than thinner ones.
7) The coating deposition by means of the formulation of a slurry and 30% wt. of fine aerogel powder demonstrated to be the most suitable approach in comparison with the solution dip coating and the doctor-blade methods. Mostly all the drawbacks were avoided since there is no evident shrinkage and detaching of the coating.
8) Both bulk and coating $La_2Zr_2O_7$ aerogels demonstrated enhanced thermal stability by the retention of its porous nature upon calcination. Despite certain consolidation of the nanoparticles, the aggregates that built the coating showed several open pores ranges below 1 μm even after continuous heating-cooling cycles at the temperatures higher than 1000 °C.

Future Work

The coating deposition of thermal-stable and highly porous aerogels was successfully completed by the slurry dip-coating method with a composition of 30% wt. of aerogel powder. The homogeneity, deposited amount and thickness was substantially improved in comparison with the other studied methods. However, the consolidation aggregate-aggregate and adhesion coating-substrate need to be enhanced due was not able to withstand the heating-cooling cycling test. Therefore, the use of a robust method such as atmospheric plasma spray can be a very promising approach to produce the ceramic top layer in TBCs using as a source the materials Ln_2Zr_2O7 synthesized in this research work.

References

[1] F. Rechberger, M. Niederberger, Synthesis of aerogels: From molecular routes to 3-dimensional nanoparticle assembly, *Nanoscale Horizons*. 2 (**2017**) 6–30. https://doi.org/10.1039/c6nh00077k.

[2] S. Yoon, G.D. Han, D.Y. Jang, J.W. Kim, D.H. Kim, J.H. Shim, Fabrication of yttria-stabilized zirconia aerogel for high-performance thermal barrier coating, *J. Alloys Compd.* 806 (**2019**) 1430–1434. https://doi.org/10.1016/j.jallcom.2019.07.156.

[3] L. Pin, C. Pilgrim, J. Feist, Y. Le Maoult, F. Ansart, P. Lours, Characterisation of thermal barrier sensor coatings synthesised by sol-gel route, *Sensors Actuators, A Phys.* 199 (**2013**) 289–296. https://doi.org/10.1016/j.sna.2013.03.022.

[4] L. Pin, V. Vidal, F. Blas, F. Ansart, S. Duluard, J.P. Bonino, Y. Le Maoult, P. Lours, Optimized sol-gel thermal barrier coatings for long-term cyclic oxidation life, *J. Eur. Ceram. Soc.* 34 (**2014**) 961–974. https://doi.org/10.1016/j.jeurceramsoc.2013.10.013.

[5] L. Pin, F. Ansart, J.-P. Bonino, Y. Le Maoult, V. Vidal, P. Lours, Reinforced sol–gel thermal barrier coatings and their cyclic oxidation life, *J. Eur. Ceram. Soc.* 33 (**2013**) 269–276. https://doi.org/10.1016/j.jeurceramsoc.2012.07.037.

[6] G. Moskal, L. Swadzba, B. Mendala, M. Góral, M. Hetmanczyk, Degradation of the TBC system during the static oxidation test, *J. Microsc.* 237 (**2010**) 450–455. https://doi.org/10.1111/j.1365-2818.2009.03290.x.

[7] C. Wang, X. Cui, G. Jin, Z. Gao, J. Jin, Z. Cai, Y. Fang, Ceramic fibers reinforced functionally graded thermal barrier coatings, *Adv. Eng. Mater.* 19 (**2017**) 1700149. https://doi.org/10.1002/adem.201700149.

[8] I. Smirnova, P. Gurikov, Aerogel production: Current status, research directions, and future opportunities, *J. Supercrit. Fluids*. 134 (**2018**) 228–233. https://doi.org/Https://doi.org/10.1016/j.supflu.2017.12.037.

[9] I. Smirnova, P. Gurikov, Aerogels in chemical engineering: strategies toward tailor-made aerogels, *Annu. Rev. Chem. Biomol. Eng.* 8 (**2017**) 307–334. https://doi.org/10.1146/annurev-chembioeng-060816-101458.

[10] J. Torres-Rodríguez, J. Kalmár, M. Menelaou, L. Čelko, K. Dvořak, J. Cihlář, J. Cihlař, J. Kaiser, E. Győri, P. Veres, I. Fábián, I. Lázár, Heat treatment induced phase

transformations in zirconia and yttria-stabilized zirconia monolithic aerogels, *J. Supercrit. Fluids*. 149 (**2019**). https://doi.org/10.1016/j.supflu.2019.02.011.

[11] A.E. Danks, S.R. Hall, Z. Schnepp, The evolution of 'sol–gel' chemistry as a technique for materials synthesis, *Mater. Horiz.* 3 (**2016**) 91–112. https://doi.org/10.1039/c5mh00260e.

[12] B.L. Cushing, V.L. Kolesnichenko, C.J. O'Connor, Recent advances in the liquid-phase syntheses of inorganic nanoparticles, *Chem. Rev.* 104 (**2004**) 3893–3946. https://doi.org/10.1021/cr030027b.

[13] C. Sanchez, J. Livage, M. Henry, F. Babonneau, Chemical modification of alkoxide precursors, *J. Non. Cryst. Solids*. 100 (**1988**) 65–76. https://doi.org/10.1016/0022-3093(88)90007-5.

[14] P.B. Wagh, A. Venkateswara Rao, D. Haranath, Influence of catalyst (citric acid) concentration on the physical properties of TEOS silica aerogels, *J. Porous Mater.* 4 (**1997**) 295–301. https://doi.org/10.1023/a:1009633524487.

[15] G. Kickelbick, P. Wiede, U. Schubert, Variations in capping the $Zr_6O_4(OH)_4$ cluster core: X-ray structure analyses of $[Zr_6(OH)_4O_4(OOC–CH=CH_2)10]_2$(μ-OOC–$CH=CH_2)_4$ and $Zr_6(OH)_4O_4(OOCR)_{12}$(PrOH) (R=Ph, $CMe=CH_2$), *Inorganica Chim. Acta*. 284 (**1999**) 1–7. https://doi.org/Https://doi.org/10.1016/s0020-1693(98)00251-5.

[16] R.B. Mos, M. Nasui, T. Petrisor, M.S. Gabor, R.A. Varga, L. Ciontea, Synthesis, crystal structure and thermal decomposition of $Zr_6O_4(OH)_4(CH_3CH_2COO)_{12}$, *J. Anal. Appl. Pyrolysis*. 97 (**2012**) 137–142. https://doi.org/Https://doi.org/10.1016/j.jaap.2012.06.010.

[17] C. Artner, M. Czakler, U. Schubert, New zirconium and zirconium–titanium oxo cluster types by expansion or metal substitution of the octahedral Zr_6O_8 structural motif, *Inorganica Chim. Acta*. 432 (**2015**) 208–212. https://doi.org/Https://doi.org/10.1016/j.ica.2015.04.013.

[18] F.R. Kogler, M. Jupa, M. Puchberger, U. Schubert, Control of the ratio of functional and non-functional ligands in clusters of the type $Zr_6O_4(OH)_4$(carboxylate)$_{12}$ for their use as building blocks for inorganic-organic hybrid polymers, *J. Mater. Chem.* 14 (**2004**) 3133–3138. https://doi.org/10.1039/b405769d.

[19] X. Li, Y. Jiao, H. Ji, X. Sun, The effect of propylene oxide on microstructure of zirconia monolithic aerogel, *Integr. Ferroelectr.* 146 (**2013**) 122–126. https://doi.org/10.1080/10584587.2013.789763.

[20] L. Zhong, X. Chen, H. Song, K. Guo, Z. Hu, Synthesis of monolithic zirconia aerogel via a nitric acid assisted epoxide addition method, *RSC Adv.* 4 (**2014**) 31666–31671. https://doi.org/10.1039/c4ra04601c.

[21] Z. Zhao, D. Chen, X. Jiao, Zirconia aerogels with high surface area derived from sols prepared by electrolyzing zirconium oxychloride solution: comparison of aerogels prepared by freeze-drying and supercritical CO_2(l) extraction, *J. Phys. Chem. C*. 111 (**2007**) 18738–18743. https://doi.org/10.1021/jp075150b.

[22] C.N. Chervin, B.J. Clapsaddle, H.W. Chiu, A.E. Gash, J.H. Satcher, S.M. Kauzlarich, Aerogel synthesis of yttria-stabilized zirconia by a non-alkoxide sol−gel route, *Chem. Mater.* 17 (**2005**) 3345–3351. https://doi.org/10.1021/cm0503679.

[23] M.A. Worsley, J. Ilsemann, T.M. Gesing, V. Zielasek, A.J. Nelson, R.A.S. Ferreira, L.D. Carlos, A.E. Gash, M. Bäumer, Chlorine-free, monolithic lanthanide series rare earth oxide aerogels via epoxide-assisted sol-gel method, *J. Sol-Gel Sci. Technol.* 89 (**2019**) 176–188. https://doi.org/10.1007/s10971-018-4811-y.

[24] C. Brinker Scherer G., Sol-Gel Science, London, **1990**.

[25] S. Hæreid, J. Anderson, M.A. Einarsrud, D.W. Hua, D.M. Smith, Thermal and temporal aging of TMOS-based aerogel precursors in water, *J. Non. Cryst. Solids*. 185 (**1995**) 221–226. https://doi.org/Https://doi.org/10.1016/0022-3093(95)00016-x.

[26] M.-A. Einarsrud, E. Nilsen, Strengthening of water glass and colloidal sol based silica gels by aging in TEOS, *J. Non. Cryst. Solids*. 226 (**1998**) 122–128. https://doi.org/Https://doi.org/10.1016/s0022-3093(98)00370-6.

[27] M.-A. Einarsrud, E. Nilsen, A. Rigacci, G.M. Pajonk, S. Buathier, D. Valette, M. Durant, B. Chevalier, P. Nitz, F. Ehrburger-Dolle, Strengthening of silica gels and aerogels by washing and aging processes, *J. Non. Cryst. Solids*. 285 (**2001**) 1–7. https://doi.org/Https://doi.org/10.1016/s0022-3093(01)00423-9.

[28] S. Hæreid, M. Dahle, S. Lima, M.-A. Einarsrud, Preparation and properties of monolithic silica xerogels from TEOS-based alcogels aged in silane solutions, *J. Non. Cryst. Solids*. 186 (**1995**) 96–103. https://doi.org/Https://doi.org/10.1016/0022-

3093(95)00039-9.

[29] I. Lázár, I. Fábián, A continuous extraction and pumpless supercritical CO_2 drying system for laboratory-scale aerogel production, *Gels*. 2 (**2016**) 26. https://doi.org/10.3390/gels2040026.

[30] I. Smirnova, Synthesis of silica aerogels and their application as a drug delivery system, Technischen Universität Berlin, **2002**.

[31] Y.-M. Chang, C.-Y. Wu, P.-W. Wu, Synthesis of large surface area carbon xerogels for electrochemical double layer capacitors, *J. Power Sources*. 223 (**2013**) 147–154. https://doi.org/10.1016/j.jpowsour.2012.09.066.

[32] N. Rodríguez, Y.Y. Agámez-Pertuz, E. Romero, J. de J. Díaz-Velásquez, J.A. Odriozola, M.Á. Centeno, Effect of starch as binder in carbon aerogel and carbon xerogel preparation, *J. Non. Cryst. Solids*. 522 (**2019**) 119554. https://doi.org/10.1016/j.jnoncrysol.2019.119554.

[33] Z. Niu, X. He, T. Huang, B. Tang, X. Cheng, Y. Zhang, Z. Shao, A facile preparation of transparent methyltriethoxysilane based silica xerogel monoliths at ambient pressure drying, *Microporous Mesoporous Mater.* 286 (**2019**) 98–104. https://doi.org/10.1016/j.micromeso.2019.05.036.

[34] A. Bisson, A. Rigacci, D. Lecomte, E. Rodier, P. Achard, Drying of silica gels to obtain aerogels: phenomenology and basic techniques, *Dry. Technol.* 21 (**2003**) 593–628. https://doi.org/10.1081/drt-120019055.

[35] G.M. Pajonk, M. Repellin-Lacroix, S. Abouarnadasse, J. Chaouki, D. Klavana, From sol-gel to aerogels and cryogels, *J. Non. Cryst. Solids*. 121 (**1990**) 66–67. https://doi.org/10.1016/0022-3093(90)90106-v.

[36] S. V. Kalinin, L.I. Kheifets, A.I. Mamchik, A.G. Knot'ko, A.A. Vertegel, Influence of the drying technique on the structure of silica gels, *J. Sol-Gel Sci. Technol.* 15 (**1999**) 31–35. https://doi.org/10.1023/a:1008771829173.

[37] G.W. Scherer, Freezing gels, *J. Non. Cryst. Solids*. 155 (**1993**) 1–25. https://doi.org/10.1016/0022-3093(93)90467-c.

[38] N. Leventis, A. Palczer, L. McCorkle, G. Zhang, C. Sotiriou-Leventis, Nanoengineered silica-polymer composite aerogels with no need for supercritical fluid drying, *J. Sol-Gel Sci. Technol.* 35 (**2005**) 99–105. https://doi.org/10.1007/s10971-

005-1372-7.

[39] Svenska Aerogel, (**2019**). https://www.aerogel.se/en/ (accessed September, 2019).

[40] Cabot, (**2019**). http://www.cabotcorp.com/solutions/products-plus/aerogel (accessed September, 2019).

[41] Aspen Aerogels, (**2019**). https://www.aerogel.com/ (accessed September, 2019).

[42] Oros, (**2019**). https://www.orosapparel.com/ (accessed September, 2019).

[43] M. Koebel, A. Rigacci, P. Achard, Aerogel-based thermal superinsulation: An overview, *J. Sol-Gel Sci. Technol.* 63 (**2012**) 315–339. https://doi.org/10.1007/s10971-012-2792-9.

[44] U. Berardi, Aerogel-enhanced insulation for building applications, *Nanotechnol. Eco-Efficient Constr.* (**2019**) 395–416. https://doi.org/10.1016/b978-0-08-102641-0.00017-7.

[45] Y. Yang, H. Wu, L. Yang, T. Xu, Y. Ding, P. Fu, Thermal and day-lighting performance of aerogel glazing system in large atrium building under cooling-dominant climates, *Energy Procedia*. 158 (**2019**) 6347–6357. https://doi.org/10.1016/j.egypro.2019.01.273.

[46] Á. Lakatos, Stability investigations of the thermal insulating performance of aerogel blanket, *Energy Build.* 185 (**2019**) 103–111. https://doi.org/10.1016/j.enbuild.2018.12.029.

[47] J. Fricke, T. Tillotson, Aerogels: production, characterization, and applications, *Thin Solid Films*. 297 (**1997**) 212–223. https://doi.org/Https://doi.org/10.1016/s0040-6090(96)09441-2.

[48] J. Yang, H. Wu, X. Xu, G. Huang, T. Xu, S. Guo, Y. Liang, Numerical and experimental study on the thermal performance of aerogel insulating panels for building energy efficiency, *Renew. Energy*. 138 (**2019**) 445–457. https://doi.org/10.1016/j.renene.2019.01.120.

[49] E. Cuce, P.M. Cuce, C.J. Wood, S.B. Riffat, Toward aerogel based thermal superinsulation in buildings: A comprehensive review, *Renew. Sustain. Energy Rev.* 34 (**2014**) 273–299. https://doi.org/10.1016/j.rser.2014.03.017.

[50] Shih-Kang Fan, Chang-Jin Kim, Jong-Ah Paik, B. Dunn, P.R. Patterson, M.C. Wu, MEMS with thin-film aerogel, in: Tech. Dig. MEMS 2001. 14th IEEE Int. Conf. Micro

Electro Mech. Syst. (Cat. No.01CH37090), IEEE, pp. 122–125. https://doi.org/10.1109/memsys.2001.906494.

[51] V.P.J. Chung, M.-C. Yip, W. Fang, Resorcinol–formaldehyde aerogels for CMOS-MEMS capacitive humidity sensor, *Sensors Actuators B Chem.* 214 (**2015**) 181–188. https://doi.org/10.1016/j.snb.2015.03.024.

[52] X.Y. Sun, W.B. Luo, J. Meng, X. Qing, W.Y. Fu, Y. Shuai, C.G. Wu, Monolithic pyroelectric infrared detectors using SiO_2 aerogel thin films, *Sensors Actuators A Phys.* 228 (**2015**) 69–74. https://doi.org/10.1016/j.sna.2015.03.006.

[53] L. Pin, F. Ansart, J.P. Bonino, Y. Le Maoult, V. Vidal, P. Lours, Processing, repairing and cyclic oxidation behaviour of sol-gel thermal barrier coatings, *Surf. Coatings Technol.* 206 (**2011**) 1609–1614. https://doi.org/10.1016/j.surfcoat.2011.06.043.

[54] C. Wang, X. Cui, G. Jin, Z. Gao, J. Jin, Z. Cai, Y. Fang, Ceramic Fibers Reinforced Functionally Graded Thermal Barrier Coatings, *Adv. Eng. Mater.* 19 (**2017**) 1700149. https://doi.org/10.1002/adem.201700149.

[55] J. Fenech, C. Viazzi, F. Ansart, J.P. Bonino, Elaboration of sol-gel coatings from aerogels and xerogels of doped zirconia for TBC applications, *Adv. Mater. Res.* 89–91 (**2010**) 184–189. https://doi.org/10.4028/www.scientific.net/amr.89-91.184.

[56] A.C. Karaoglanli, T. Grund, A. Turk, T. Lampke, A comparative study of oxidation kinetics and thermal cyclic performance of thermal barrier coatings (TBCs), *Surf. Coatings Technol.* 371 (**2019**) 47–67. https://doi.org/10.1016/j.surfcoat.2018.12.082.

[57] D. Shi, J. Song, S. Li, H. Qi, X. Yang, Cracking behaviors of EB-PVD thermal barrier coating under temperature gradient, *Ceram. Int.* 45 (**2019**) 18518–18528. https://doi.org/10.1016/j.ceramint.2019.06.071.

[58] O. Fabrichnaya, H.J. Seifert, T. Ludwig, F. Aldinger, A. Navrotsky, The assessment of thermodynamic parameters in the Al_2O_3-Y_2O_3 system and phase relations in the Y-Al-O system, *Scand. J. Metall.* 30 (**2001**) 175–183. https://doi.org/10.1034/j.1600-0692.2001.300308.x.

[59] U. Schulz, B. Saruhan, K. Fritscher, C. Leyens, Review on advanced EB-PVD ceramic topcoats for TBC applications, *Int. J. Appl. Ceram. Technol.* 1 (**2004**) 302–315. https://doi.org/10.1111/j.1744-7402.2004.tb00182.x.

[60] C.N. Chervin, B.J. Clapsaddle, H.W. Chiu, A.E. Gash, J.H. Satcher, S.M. Kauzlarich,

Aerogel synthesis of yttria-stabilized zirconia by a non-alkoxide sol−gel route, *Chem. Mater.* 17 (**2005**) 3345–3351. https://doi.org/10.1021/cm0503679.

[61] C.N. Chervin, B.J. Clapsaddle, H.W. Chiu, A.E. Gash, J.H. Satcher,, S.M. Kauzlarich, Role of cyclic ether and solvent in a non-alkoxide sol−gel synthesis of yttria-stabilized zirconia nanoparticles, *Chem. Mater.* 18 (**2006**) 4865–4874. https://doi.org/10.1021/cm061258c.

[62] R. Vassen, X. Cao, F. Tietz, D. Basu, D. Stöver, Zirconates as new materials for thermal barrier coatings, *J. Am. Ceram. Soc.* 83 (**2000**) 2023–2028. https://doi.org/10.1111/j.1151-2916.2000.tb01506.x.

[63] J. He, T. Li, X. Liu, H. Su, Z. Ku, J. Zhong, F. Huang, Y. Peng, Y.-B. Cheng, Influence of phase transition on stability of perovskite solar cells under thermal cycling conditions, *Sol. Energy*. 188 (**2019**) 312–317. https://doi.org/10.1016/j.solener.2019.06.025.

[64] W. Ma, M.O. Jarligo, D.E. Mack, D. Pitzer, J. Malzbender, R. Vaßen, D. Stöver, New generation perovskite thermal barrier coating materials, *J. Therm. Spray Technol.* 17 (**2008**) 831–837. https://doi.org/10.1007/s11666-008-9239-4.

[65] B. Liu, Y. Liu, C. Zhu, H. Xiang, H. Chen, L. Sun, Y. Gao, Y. Zhou, Advances on strategies for searching for next generation thermal barrier coating materials, *J. Mater. Sci. Technol.* 35 (**2019**) 833–851. https://doi.org/10.1016/j.jmst.2018.11.016.

[66] M.O. Jarligo, D.E. Mack, R. Vassen, D. Stöver, Application of plasma-sprayed complex perovskites as thermal barrier coatings, *J. Therm. Spray Technol.* 18 (**2009**) 187–193. https://doi.org/10.1007/s11666-009-9302-9.

[67] M.O. Jarligo, D.E. Mack, G. Mauer, R. Vaßen, D. Stöver, Atmospheric plasma spraying of high melting temperature complex perovskites for TBC application, *J. Therm. Spray Technol.* 19 (**2010**) 303–310. https://doi.org/10.1007/s11666-009-9377-3.

[68] H. Ibégazène, S. Alpérine, C. Diot, Yttria-stabilized hafnia-zirconia thermal barrier coatings: The influence of hafnia addition on TBC structure and high-temperature behaviour, *J. Mater. Sci.* 30 (**1995**) 938–951. https://doi.org/10.1007/bf01178428.

[69] R.L. Jones, R.F. Reidy, D. Mess, Scandia, yttria-stabilized zirconia for thermal barrier coatings, *Surf. Coatings Technol.* 82 (**1996**) 70–76.

https://doi.org/Https://doi.org/10.1016/0257-8972(95)02646-0.

[70] G. Soyez, J.A. Eastman, L.J. Thompson, G.-R. Bai, P.M. Baldo, A.W. McCormick, R.J. DiMelfi, A.A. Elmustafa, M.F. Tambwe, D.S. Stone, Grain-size-dependent thermal conductivity of nanocrystalline yttria-stabilized zirconia films grown by metal-organic chemical vapor deposition, *Appl. Phys. Lett.* 77 (**2000**) 1155–1157. https://doi.org/10.1063/1.1289803.

[71] S.K. Gupta, P.S. Ghosh, C. Reghukumar, N. Pathak, R.M. Kadam, Experimental and theoretical approach to account for green luminescence from $Gd_2Zr_2O_7$ pyrochlore: exploring the site occupancy and origin of host-dopant energy transfer in $Gd_2Zr_2O_7$:Eu^{3+}, *RSC Adv.* 6 (**2016**) 44908–44920. https://doi.org/10.1039/c6ra05113h.

[72] J. Zhang, J. Lian, A.F. Fuentes, F. Zhang, M. Lang, F. Lu, R.C. Ewing, Enhanced radiation resistance of nanocrystalline pyrochlore $Gd_2(Ti_{0.65}Zr_{0.35})_2O_7$, *Appl. Phys. Lett.* 94 (**2009**) 243110. https://doi.org/10.1063/1.3155855.

[73] S. Dey, J.W. Drazin, Y. Wang, J.A. Valdez, T.G. Holesinger, B.P. Uberuaga, R.H.R. Castro, Radiation tolerance of nanocrystalline ceramics: Insights from yttria stabilized zirconia, *Sci. Rep.* 5 (**2015**) 1–9. https://doi.org/10.1038/srep07746.

[74] E. Aleshin, R. Roy, Crystal Chemistry of Pyrochlore, *J. Am. Ceram. Soc.* 45 (**1962**) 18–25. https://doi.org/10.1111/j.1151-2916.1962.tb11022.x.

[75] M.A. Subramanian, G. Aravamudan, G.V. Subba Rao, Oxide pyrochlores — A review, *Prog. Solid State Chem.* 15 (**1983**) 55–143. https://doi.org/10.1016/0079-6786(83)90001-8.

[76] M. Touzin, F. Béclin, Fabrication and characterization of composite sol–gel coatings on porous ceramic substrate, *J. Eur. Ceram. Soc.* 31 (**2011**) 1661–1667. https://doi.org/Https://doi.org/10.1016/j.jeurceramsoc.2011.03.002.

[77] P. He, X. Gao, X. Li, Z. Jiang, Z. Yang, C. Wang, Z. Gu, Highly transparent silica aerogel thick films with hierarchical porosity from water glass via ambient pressure drying, *Mater. Chem. Phys.* 147 (**2014**) 65–74. https://doi.org/10.1016/j.matchemphys.2014.04.007.

[78] X.-D. Gao, X.-M. Li, X.-Y. Gan, Y.-Q. Wu, R.-K. Zheng, C.-L. Wang, Z.-Y. Gu, P. He, Aerogel based SiO_2–TiO_2 hybrid photoanodes for enhanced light harvesting in

dye-sensitized solar cells, *J. Mater. Chem.* 22 (**2012**) 18930. https://doi.org/10.1039/c2jm33945e.

[79] J.J. Pietron, A.M. Stux, R.S. Compton, D.R. Rolison, Dye-sensitized titania aerogels as photovoltaic electrodes for electrochemical solar cells, *Sol. Energy Mater. Sol. Cells*. 91 (**2007**) 1066–1074. https://doi.org/10.1016/j.solmat.2007.02.021.

[80] K. Sing, The use of nitrogen adsorption for the characterisation of porous materials, *Colloids Surfaces A Physicochem. Eng. Asp.* 187–188 (**2001**) 3–9. https://doi.org/10.1016/s0927-7757(01)00612-4.

[81] B.C. Lippens, J.H. de Boer, Studies on pore systems in catalysts: V. The t method, *J. Catal.* 4 (**1965**) 319–323. https://doi.org/10.1016/0021-9517(65)90307-6.

[82] E.P. Barrett, L.G. Joyner, P.P. Halenda, The determination of pore volume and area distributions in porous substances. I. computations from nitrogen isotherms, *J. Am. Chem. Soc.* 73 (**1951**) 373–380. https://doi.org/10.1021/ja01145a126.

[83] F.T.L. Muniz, M.A.R. Miranda, C. dos Santos, J.M. Sasaki, The Scherrer equation and the dynamical theory of X-ray diffraction, *Acta Crystallogr. Sect. A.* 72 (**2016**) 385–390. https://doi.org/10.1107/s205327331600365x.

[84] C.N. Chervin, B.J. Clapsaddle, H.W. Chiu, A.E. Gash, J.H. Satcher,, S.M. Kauzlarich, Aerogel synthesis of yttria-stabilized zirconia by a non-alkoxide sol−gel route, *Chem. Mater.* 17 (**2005**) 3345–3351. https://doi.org/10.1021/cm0503679.

[85] B.J. N. Chervin, Aerogel synthesis of yttria stabilized zirconia by a non alcoxide sol gel route, *Chem. Mater.* 17 (**2005**) 3345–3351.

[86] A.F. Bedilo, K.J. Klabunde, Synthesis of high surface area zirconia aerogels using high temperature supercritical drying, *Nanostructured Mater.* 8 (**1997**) 119–135. https://doi.org/Https://doi.org/10.1016/s0965-9773(97)00011-1.

[87] H. Gao, Z. Zhang, Z. Shi, J. Zhang, M. Zhi, Z. Hong, Synthesis of high-temperature resistant monolithic zirconia-based aerogel via facile water glass assisted sol–gel method, *J. Sol-Gel Sci. Technol.* 85 (**2018**) 567–573. https://doi.org/10.1007/s10971-017-4571-0.

[88] U.K.H. Bangi, H.-H. Park, Evolution of textural characteristics of surfactant-mediated mesoporous zirconia aerogel powders prepared via ambient pressure drying route, *Int. Nano Lett.* 8 (**2018**) 221–228. https://doi.org/10.1007/s40089-018-0241-7.

[89] Y. Wan, D. Zhao, On the controllable soft-templating approach to mesoporous silicates, *Chem. Rev.* 107 (**2007**) 2821–2860. https://doi.org/10.1021/cr068020s.

[90] J. Wang, H. Wang, Facile synthesis of flexible mesoporous aerogel with superhydrophobicity for efficient removal of layered and emulsified oil from water, *J. Colloid Interface Sci.* 530 (**2018**) 372–382. https://doi.org/Https://doi.org/10.1016/j.jcis.2018.07.002.

[91] M. Motta, C. V Deimling, M.J. Saeki, P.N. Lisboa-Filho, Chelating agent effects in the synthesis of mesoscopic-size superconducting particles, *J. Sol-Gel Sci. Technol.* 46 (**2008**) 201–207. https://doi.org/10.1007/s10971-007-1673-0.

[92] Y. Li, J. Zhao, B. Wang, Low temperature preparation of nanocrystalline Sr0.5Ba0.5Nb2O6 powders using an aqueous organic gel route, *Mater. Res. Bull.* 39 (**2004**) 365–374. https://doi.org/Https://doi.org/10.1016/j.materresbull.2003.11.002.

[93] A.F. Bedilo, K.J. Klabunde, Synthesis of high surface area zirconia aerogels using high temperature supercritical drying, *Nanostructured Mater.* 8 (**1997**) 119–135. https://doi.org/10.1016/s0965-9773(97)00011-1.

[94] D.A. Ward, E.I. Ko, Synthesis and structural transformation of zirconia aerogels, *Chem. Mater.* 5 (**1993**) 956–969. https://doi.org/10.1021/cm00031a014.

[95] C.N. Chervin, B.J. Clapsaddle, H.W. Chiu, A.E. Gash, J.H. Satcher,, S.M. Kauzlarich, A non-alkoxide sol−gel method for the preparation of homogeneous nanocrystalline powders of $La_{0.85}Sr_{0.15}MnO_3$, *Chem. Mater.* 18 (**2006**) 1928–1937. https://doi.org/10.1021/cm052301j.

[96] Z. Zhang, Q. Gao, Y. Liu, C. Zhou, M. Zhi, Z. Hong, F. Zhang, B. Liu, A facile citric acid assisted sol-gel method for preparing monolithic yttria-stabilized zirconia aerogel, *RSC Adv.* 5 (**2015**) 84280–84283. https://doi.org/10.1039/c5ra13999f.

[97] D.J. Suh, T.-J. Park, Sol−gel strategies for pore size control of high-surface-area transition-metal oxide aerogels, *Chem. Mater.* 8 (**1996**) 509–513. https://doi.org/10.1021/cm950407g.

[98] N. Shimoda, K. Nakayama, K. Kiyota, S. Satokawa, Synthesis of tetragonal zirconia in mesoporous silica and its catalytic properties for methanol oxidative decomposition, *RSC Adv.* 7 (**2017**) 55819–55829. https://doi.org/10.1039/c7ra10942c.

[99] R. Sui, A.S. Rizkalla, P.A. Charpentier, Direct synthesis of zirconia aerogel

nanoarchitecture in supercritical CO_2, *Langmuir*. 22 (**2006**) 4390–4396. https://doi.org/10.1021/la053513y.

[100] L. Sun, H. Guo, H. Peng, S. Gong, H. Xu, Phase stability and thermal conductivity of ytterbia and yttria co-doped zirconia, *Prog. Nat. Sci. Mater. Int.* 23 (**2013**) 440–445. https://doi.org/10.1016/j.pnsc.2013.06.013.

[101] L.B. Hamouda, A. Ghorbel, New process to control hydrolysis step during sol-gel preparation of sulfated zirconia catalysts, *J. Sol-Gel Sci. Technol.* 39 (**2006**) 123–130. https://doi.org/10.1007/s10971-006-9174-0.

[102] R.C. Garvie, The occurrence of metastable tetragonal zirconia as a crystallite size effect, *J. Phys. Chem.* 69 (**1965**) 1238–1243. https://doi.org/10.1021/j100888a024.

[103] F. Lu, J. Zhang, M. Huang, F. Namavar, R.C. Ewing, J. Lian, Phase transformation of nanosized ZrO_2 upon thermal annealing and intense radiation, *J. Phys. Chem. C*. 115 (**2011**) 7193–7201. https://doi.org/10.1021/jp109558s.

[104] O.Y. Kurapova, V.G. Konakov, Phase evolution in zirconia based systems, *Rev. Adv. Mater. Sci.* 36 (**2014**) 177–190.

[105] S. Shukla, S. Seal, Mechanisms of room temperature metastable tetragonal phase stabilisation in zirconia, *Int. Mater. Rev.* 50 (**2005**) 45–64. https://doi.org/10.1179/174328005x14267.

[106] S. Shukla, S. Seal, Thermodynamic tetragonal phase stability in sol-gel derived nanodomains of pure zirconia, *J. Phys. Chem. B.* 108 (**2004**) 3395–3399. https://doi.org/10.1021/jp037532x.

[107] C. Stöcker, A. Baiker, Zirconia aerogels: effect of acid-to-alkoxide ratio, alcoholic solvent and supercritical drying method on structural properties, *J. Non. Cryst. Solids*. 223 (**1998**) 165–178. https://doi.org/Https://doi.org/10.1016/s0022-3093(97)00340-2.

[108] R. Haul, S. J. Gregg, K. S. W. Sing: Adsorption, surface area and porosity. 2. Auflage, Academic Press, London 1982. 303 Seiten, *Berichte Der Bunsengesellschaft Für Phys. Chemie*. 86 (**1982**) 957. https://doi.org/10.1002/bbpc.19820861019.

[109] C.J. Gommes, A.P. Roberts, Stochastic analysis of capillary condensation in disordered mesopores, *Phys. Chem. Chem. Phys.* 20 (**2018**) 13646–13659. https://doi.org/10.1039/c8cp01628c.

[110] M. Thommes, K. Kaneko, A. V. Neimark, J.P. Olivier, F. Rodriguez-Reinoso, J.

Rouquerol, K.S.W. Sing, Physisorption of gases, with special reference to the evaluation of surface area and pore size distribution (IUPAC Technical Report), *Pure Appl. Chem.* 87 (**2015**) 1051–1069. https://doi.org/10.1515/pac-2014-1117.

[111] H.G. Scott, Phase relationships in the zirconia-yttria system, *J. Mater. Sci.* 10 (**1975**) 1527–1535. https://doi.org/10.1007/bf01031853.

[112] T. Mitsuhashi, M. Ichihara, U. Tatsuke, Characterization and stabilization of metastable tetragonal ZrO_2, *J. Am. Ceram. Soc.* 57 (**1974**) 97–101. https://doi.org/10.1111/j.1151-2916.1974.tb10823.x.

[113] X. Xu, X. Wang, Fine tuning of the sizes and phases of ZrO_2 nanocrystals, *Nano Res.* 2 (**2009**) 891–902. https://doi.org/10.1007/s12274-009-9092-x.

[114] J. Vage, K. Doi, C. Mazieres, Nature and thermal evolution of amorphous hvdrated zirconium Oxide, *J. Am. Ceram. Soc.* 51 (**1968**) 349–353. https://doi.org/Doi:10.1111/j.1151-2916.1968.tb15952.x.

[115] V.G. Keramidas, W.B. White, Raman scattering study of the crystallization and phase transformations of ZrO_2, *J. Am. Ceram. Soc.* 57 (**1974**) 22–24. https://doi.org/Doi:10.1111/j.1151-2916.1974.tb11355.x.

[116] E. Tani, M. Yoshimura, S. Somiya, Formation of ultrafine tetragonal ZrO_2 powder under hydrothermal conditions, *J. Am. Ceram. Soc.* 66 (**1983**) 11–14. https://doi.org/10.1111/j.1151-2916.1983.tb09958.x.

[117] S. Wang, W. Li, S. Wang, J. Jiang, Z. Chen, Synthesis of well-defined hierarchical porous $La_2Zr_2O_7$ monoliths via non-alkoxide sol–gel process accompanied by phase separation, *Microporous Mesoporous Mater.* 221 (**2016**) 32–39. https://doi.org/10.1016/j.micromeso.2015.08.031.

[118] H. Chen, Y. Gao, Y. Liu, H. Luo, Coprecipitation synthesis and thermal conductivity of $La_2Zr_2O_7$, *J. Alloys Compd.* 480 (**2009**) 843–848. https://doi.org/10.1016/j.jallcom.2009.02.081.

[119] S. Wang, W. Li, S. Wang, Z. Chen, Synthesis of mesoporous $La_2Zr_2O_7$ with high surface area by combining epoxide-mediated sol-gel process and solvothermal treatment, *Microporous Mesoporous Mater.* 234 (**2016**) 137–145. https://doi.org/10.1016/j.micromeso.2016.07.020.

[120] A.F. Fuentes, S.M. Montemayor, M. Maczka, M. Lang, R.C. Ewing, U. Amador, A

critical review of existing criteria for the prediction of pyrochlore formation and stability, *Inorg. Chem.* 57 (**2018**) 12093–12105. https://doi.org/10.1021/acs.inorgchem.8b01665.

[121] J. Torres-Rodriguez, V. Gutierrez-Cano, M. Menelaou, J. Kaštyl, J. Cihlář, S. Tkachenko, J.A. González, J. Kalmár, I. Fábián, I. Lázár, L. Čelko, J. Kaiser, Rare-earth zirconate $Ln_2Zr_2O_7$ (Ln: La, Nd, Gd, and Dy) powders, xerogels, and aerogels: preparation, structure, and properties, *Inorg. Chem.* (**2019**) acs.inorgchem.9b01965. https://doi.org/10.1021/acs.inorgchem.9b01965.

[122] L. Zhou, Z. Huang, J. Qi, Z. Feng, D. Wu, W. Zhang, X. Yu, Y. Guan, X. Chen, L. Xie, K. Sun, T. Lu, Thermal-driven fluorite–pyrochlore–fluorite phase transitions of $Gd_2Zr_2O_7$ ceramics probed in large range of sintering temperature, *Metall. Mater. Trans. A Phys. Metall. Mater. Sci.* 47 (**2016**) 623–630. https://doi.org/10.1007/s11661-015-3234-4.

[123] K. Shimamura, T. Arima, K. Idemitsu, Y. Inagaki, Thermophysical properties of rare-earth-stabilized zirconia and zirconate pyrochlores as surrogates for actinide-doped zirconia, *Int. J. Thermophys.* 28 (**2007**) 1074–1084. https://doi.org/10.1007/s10765-007-0232-9.

[124] D. Michel, M.P. y Jorba, R. Collongues, Study by raman spectroscopy of order-disorder phenomena occurring in some binary oxides with fluorite-related structures, *J. Raman Spectrosc.* 5 (**1976**) 163–180. https://doi.org/10.1002/jrs.1250050208.

[125] S. Wang, W. Li, S. Wang, Z. Chen, Synthesis of nanostructured $La_2Zr_2O_7$ by a non-alkoxide sol–gel method: from gel to crystalline powders, *J. Eur. Ceram. Soc.* 35 (**2015**) 105–112. https://doi.org/10.1016/j.jeurceramsoc.2014.08.032.

[126] F.N. Sayed, V. Grover, K. Bhattacharyya, D. Jain, A. Arya, C.G.S. Pillai, A.K. Tyagi, $Sm_{2-x}Dy_xZr_2O_7$ pyrochlores: probing order-disorder dynamics and multifunctionality, *Inorg. Chem.* 50 (**2011**) 2354–2365. https://doi.org/10.1021/ic200108u.

[127] C. Kaliyaperumal, A. Sankarakumar, J. Palanisamy, T. Paramasivam, Fluorite to pyrochlore phase transformation in nanocrystalline $Nd_2Zr_2O_7$, *Mater. Lett.* 228 (**2018**) 493–496. https://doi.org/10.1016/j.matlet.2018.06.087.

[128] B.P. Mandal, N. Garg, S.M. Sharma, A.K. Tyagi, Preparation, XRD and raman spectroscopic studies on new compounds $RE_2Hf_2O_7$ (RE=Dy, Ho, Er, Tm, Lu, Y):

Pyrochlores or defect-fluorite?, *J. Solid State Chem.* 179 (**2006**) 1990–1994. https://doi.org/10.1016/j.jssc.2006.03.036.

[129] A. Feinberg, C.H. Perry, Structural disorder and phase transitions in ZrO_2-Y_2O_3 system, *J. Phys. Chem. Solids*. 42 (**1981**) 513–518. https://doi.org/10.1016/0022-3697(81)90032-9.

[130] S. Vasanthavel, B. Derby, S. Kannan, Tetragonal to cubic transformation of SiO_2-Stabilized ZrO_2 polymorph through dysprosium substitutions, *Inorg. Chem.* 56 (**2017**) 1273–1281. https://doi.org/10.1021/acs.inorgchem.6b02361.

[131] C.N. Chervin, B.J. Clapsaddle, H.W. Chiu, A.E. Gash, J.H. Satcher, S.M. Kauzlarich, Aerogel synthesis of yttria-stabilized zirconia by a non-alkoxide sol-gel route, *Chem. Mater.* 17 (**2005**) 3345–3351. https://doi.org/10.1021/cm0503679.

[132] I. Lázár, J. Kalmár, A. Peter, A. Szilágyi, E. Győri, T. Ditrói, I. Fábián, Photocatalytic performance of highly amorphous titania–silica aerogels with mesopores: The adverse effect of the in situ adsorption of some organic substrates during photodegradation, *Appl. Surf. Sci.* 356 (**2015**) 521–531. https://doi.org/10.1016/j.apsusc.2015.08.113.

[133] Y.V. Kolen'ko, A.V. Garshev, B.R. Churagulov, S. Boujday, P. Portes, C. Colbeau-Justin, Photocatalytic activity of sol–gel derived titania converted into nanocrystalline powders by supercritical drying, *J. Photochem. Photobiol. A Chem.* 172 (**2005**) 19–26. https://doi.org/10.1016/j.jphotochem.2004.11.004.

[134] H. Li, G. Li, J. Zhu, Y. Wan, Preparation of an active SO_4^{2-}/TiO_2 photocatalyst for phenol degradation under supercritical conditions, *J. Mol. Catal. A Chem.* 226 (**2005**) 93–100. https://doi.org/10.1016/j.molcata.2004.09.028.

[135] R. Moussaoui, K. Elghniji, M. ben Mosbah, E. Elaloui, Y. Moussaoui, Sol–gel synthesis of highly TiO_2 aerogel photocatalyst via high temperature supercritical drying, *J. Saudi Chem. Soc.* 21 (**2017**) 751–760. https://doi.org/10.1016/j.jscs.2017.04.001.

[136] M. Ozawa, M. Kimura, Preparation and characterization of zirconium dioxide catalyst supports modified with rare earth elements, *J. Less Common Met.* 171 (**1991**) 195–212. https://doi.org/10.1016/0022-5088(91)90143-r.

[137] O. Gorban, S. Synyakina, G. Volkova, S. Gorban, T. Konstantiova, S. Lyubchik, Formation of metastable tetragonal zirconia nanoparticles: Competitive influence of

the dopants and surface state, *J. Solid State Chem.* 232 (**2015**) 249–255. https://doi.org/10.1016/j.jssc.2015.09.026.

[138] L. Kong, I. Karatchevtseva, D.J. Gregg, M.G. Blackford, R. Holmes, G. Triani, A novel chemical route to prepare $La_2Zr_2O_7$ pyrochlore, *J. Am. Ceram. Soc.* 96 (**2013**) 935–941. https://doi.org/10.1111/jace.12060.

[139] A. Joulia, E. Renard, D. Tchou-Kien, M. Vardelle, S. Rossignol, Rare earth oxides pyrochlore compounds by soft chemistry, in: Adv. Ceram. Coatings Mater. Extrem. Environ. II, John Wiley & Sons, Ltd, **2012**: pp. 57–65. https://doi.org/10.1002/9781118217474.ch5.

[140] ISO, Iso 9277:2010, 2010 (**2010**) 24.

[141] M. Thommes, Physical adsorption characterization of nanoporous materials, *Chemie Ing. Tech.* 82 (**2010**) 1059–1073. https://doi.org/10.1002/cite.201000064.

[142] A. Díaz-Parralejo, A. Macías-García, E.M. Cuerda-Correa, R. Caruso, Influence of the type of solvent on the textural evolution of yttria stabilized zirconia powders obtained by the sol–gel method: Characterization and study of the fractal dimension, *J. Non. Cryst. Solids*. 351 (**2005**) 2115–2121. https://doi.org/10.1016/j.jnoncrysol.2005.03.046.

[143] A. Díaz-Parralejo, A. Macías-García, J. Sánchez-González, M.Á. Díaz-Díez, E.M. Cuerda-Correa, Influence of the experimental parameters on the synthesis process of yttria-doped zirconia sol–gel films, *Surf. Coatings Technol.* 204 (**2010**) 2257–2261. https://doi.org/10.1016/j.surfcoat.2009.12.015.

[144] T. Or, S. Saem, A. Esteve, D.A. Osorio, K.J. De France, J. Vapaavuori, T. Hoare, A. Cerf, E.D. Cranston, J.M. Moran-Mirabal, Patterned cellulose nanocrystal aerogel films with tunable dimensions and morphologies as ultra-porous scaffolds for cell culture, *ACS Appl. Nano Mater.* 2 (**2019**) 4169–4179. https://doi.org/10.1021/acsanm.9b00640.

[145] Z. Teng, G. Zheng, Y. Dou, W. Li, C.-Y. Mou, X. Zhang, A.M. Asiri, D. Zhao, Highly ordered mesoporous silica films with perpendicular mesochannels by a simple stöber-solution growth approach, *Angew. Chemie Int. Ed.* 51 (**2012**) 2173–2177. https://doi.org/10.1002/anie.201108748.

[146] L. Scandola, S. Latorrata, R. Matarrese, C. Cristiani, I. Nova, Effect of thickness and

cracking phenomena on the photocatalytic performances of Ti/TiO_2 photoanodes produced by dip coating, *Mater. Chem. Phys.* 234 (**2019**) 1–8. https://doi.org/10.1016/j.matchemphys.2019.05.074.

[147] A.C. Pierre, G.M. Pajonk, Chemistry of aerogels and their applications, *Chem. Rev.* 102 (**2002**) 4243–4266. https://doi.org/10.1021/cr0101306.

[148] C.-T. Wang, C.-L. Wu, I.-C. Chen, Y.-H. Huang, Humidity sensors based on silica nanoparticle aerogel thin films, *Sensors Actuators B Chem.* 107 (**2005**) 402–410. https://doi.org/10.1016/j.snb.2004.10.034.

[149] M. Seyedjalali, M.R. Madani, Silica aerogel thick film, an alternative to micromachined air gap for thermal insulation, *Electron. Lett.* 51 (**2015**) 849–850. https://doi.org/10.1049/el.2015.0088.

[150] D.A. Barrow, T.E. Petroff, R.P. Tandon, M. Sayer, Characterization of thick lead zirconate titanate films fabricated using a new sol gel based process, *J. Appl. Phys.* 81 (**1997**) 876–881. https://doi.org/10.1063/1.364172.

[151] E. Santanach Carreras, F. Chabert, D.E. Dunstan, G.V. Franks, Avoiding "mud" cracks during drying of thin films from aqueous colloidal suspensions, *J. Colloid Interface Sci.* 313 (**2007**) 160–168. https://doi.org/10.1016/j.jcis.2007.03.076.

[152] P.C. Innocenzi, M. Guglielmi, M. Gobbin, P. Colombo, Coating of metals by the sol-gel dip-coating method, *J. Eur. Ceram. Soc.* 10 (**1992**) 431–436. https://doi.org/10.1016/0955-2219(92)90018-9.

[153] A. Torabi, T.H. Etsell, P. Sarkar, Dip coating fabrication process for micro-tubular SOFCs, *Solid State Ionics*. 192 (**2011**) 372–375. https://doi.org/10.1016/j.ssi.2010.09.050.

[154] P. Xu, A.S. Mujumdar, B. Yu, Drying-induced cracks in thin film fabricated from colloidal dispersions, *Dry. Technol.* 27 (**2009**) 636–652. https://doi.org/10.1080/07373930902820804.

Appendix A

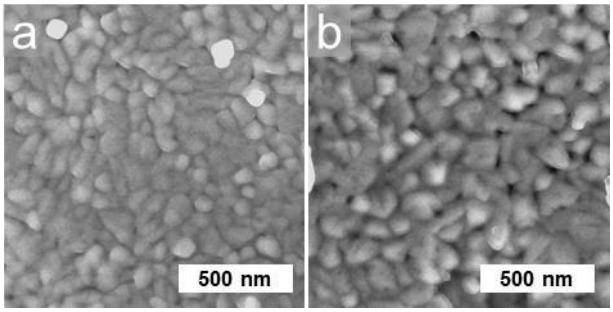

Fig. A1. Scanning electron microscopy: Surface morphology of the calcined powders at 1000 °C / 5 hrs.

a) $Nd_2Zr_2O_7$ and b) $Dy_2Zr_2O_7$.

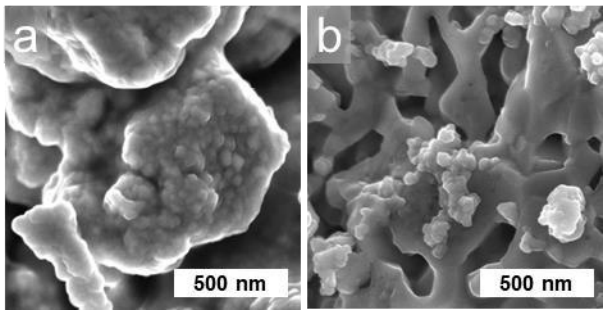

Fig. A2. Scanning electron microscopy: Surface morphology of the calcined xerogels at 1000 °C / 5 hrs.

a) $Nd_2Zr_2O_7$ and b) $Dy_2Zr_2O_7$.

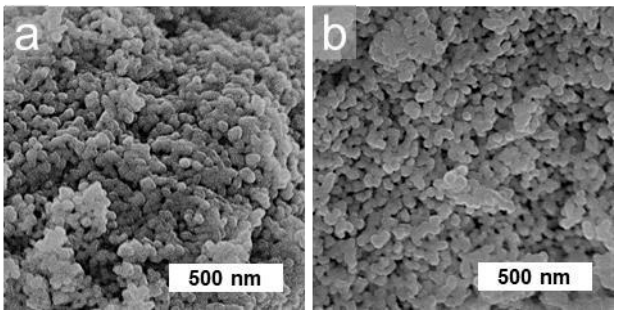

Fig. A3. Scanning electron microscopy: Surface morphology of the calcined aerogels at 1000 °C / 5 hrs.
a) $Nd_2Zr_2O_7$ and b) $Dy_2Zr_2O_7$.

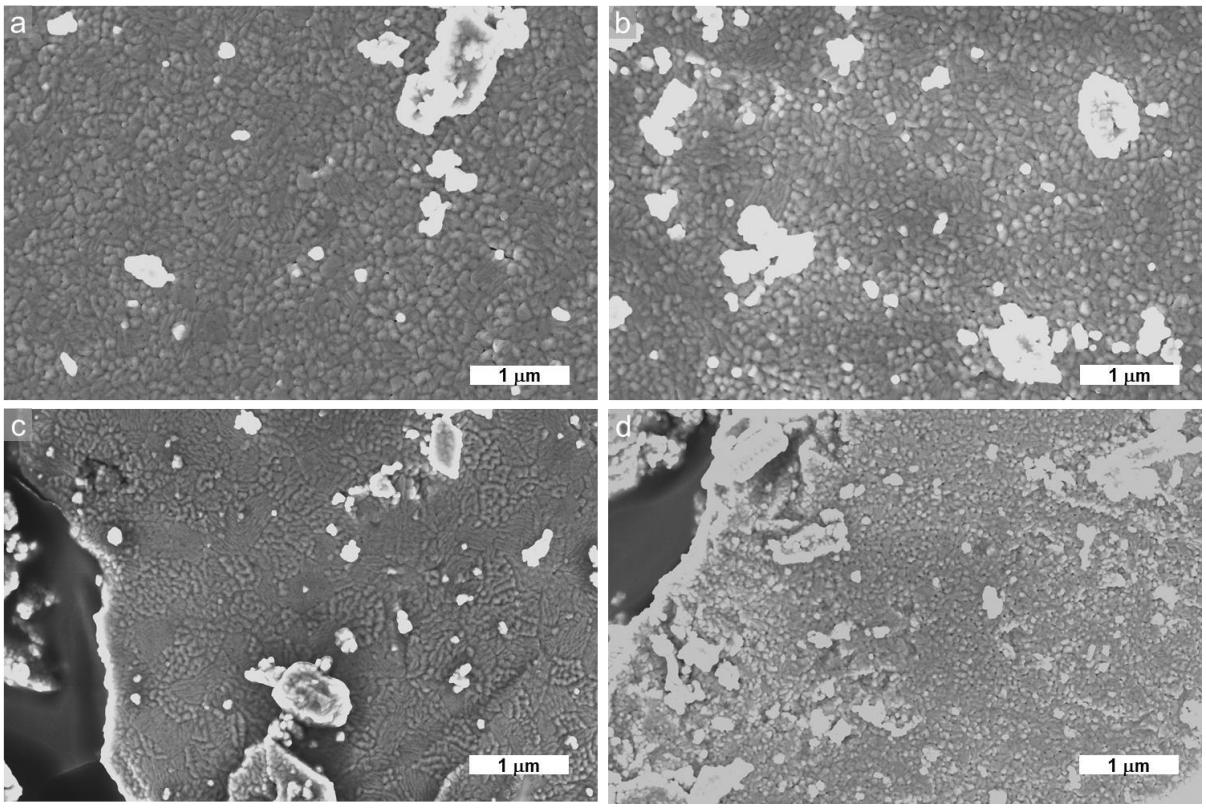

Fig. A4. Scanning electron microscopy: Lower magnification surface morphology of the calcined powders at 1000 °C / 5 hrs; a) $La_2Zr_2O_7$; b) $Nd_2Zr_2O_7$; c) $Gd_2Zr_2O_7$; and d) $Dy_2Zr_2O_7$.

Fig. A5. Macrographs of the as-obtained materials; a) LZP; b) LZX; and c) LZA

List of publications

1. Rare-earth Zirconate $Ln_2Zr_2O_7$ (Ln: La, Nd, Gd and Dy) Powders, Xerogels and Aerogels: Preparation, Structure and Properties.
   Jorge Torres-Rodriguez, Vanessa Gutierrez-Cano, Melita Menelaou, Jaroslav Kaštyl, Jaroslav Cihlář, Serhii Tkachenko, Jesús A. González, József Kalmár, István Fábián, István Lázár, Ladislav Čelko, Jozef Kaiser. *Inorganic Chemistry*, **2019**. DOI: 10.1021/acs.inorgchem.9b01965

2. Heat treatment induced phase transformations in zirconia and yttria-stabilized zirconia monolithic aerogels.
   Jorge Torres-Rodríguez, József Kalmár, Melita Menelaou, Ladislav Čelko, Karel Dvořak, Jaroslav Cihlář, Jaroslav Cihlař Jr, Jozef Kaiser, Enikő Győri, Péter Veres, István Fábián, István Lázár. *The Journal of Supercritical Fluids, **2019***. DOI: 10.1016/j.supflu.2019.02.011

3. Robocasting of controlled porous $CaSiO_3$-SiO_2 structures: mechanical behavior and catalytic activity. M. Casas-Luna, **J. A. Torres-Rodríguez**, O. U. Valdés-Martínez, N. Obradović, K. Slámečka, K. Maca, J. Kaiser, E.B. Montúfar, L. Čelko. *Ceramics International*, **2019**. Submitted.

4. Influence of Surfactants on SiO_2 Aerogels. **Jorge Torres-Rodríguez.**; Mariano Casas-Luna.; Serhii Tkachenko. *Metal 2017 Conference Prosceedings*. Ostrava: TANGER Ltd., **2018**. s. 1135-1140. ISBN: 978-80-87294-79-6

5. Casas Luna, M., Tkachenko, S., Klakurková, L., **Torres-Rodriguez, J,** Zikmund, T. Micro-Computed Tomography of Interconnected Mg-TCP Composites Obtained by Current Assisted Metal Infiltration. *Metal 2017 Conference Prosceedings.* Ostrava: TANGER Ltd., 2018. s. 1669-1675. ISBN: 978-80-87294-79-6.

Abbreviations list

Acac	*Acetylacetone*
APS	*Air Plasma Spray*
DSC	*Differential Scanning Calorimetry*
EB-PVD	*Electron Beam Physical Vapor Deposition*
F	*Fluorite crystalline structure*
FCT	*Furnace Cycling oxidation Test*
FWHM	*Full Width at Half Maximum*
GOF	*Goodness Of Fit*
HMDSO	*Hexamethyldisiloxane*
IR	*Infrared*
IUPAC	*International Union of Pure and Applied Chemistry*
LZ	*Lanthanide Zirconate*
MEMS	*Microelectromechanical System*
MS	*Mass Spectrometry*
P	*Pyrochlore crystalline structure*
Pc	*Critical pressure*
PEG	*Polyethylene Glycol*
rpm	*Revolutions er minute*
SCD	*Supercritical Drying*
SCF	*Supercritical Fluid*
SEM	*Scanning Electron Microscope*
TBC	*Thermal Barrier Coating*
Tc	*Critical temperature*
TGA	*Thermogravimetric Analysis*
TMCS	*Trimethylchlorosilane*
TMOS	*Tetramethyl orthosilicate*
XRD	*X-ray diffraction*
YSZ	*Yttria-stabilized zirconia*

Internship, trainings, and other activities

- University of Debrecen, Debrecen, Hungary
- Teaching and training to undergraduate students at the Central European Institute of Technology (CEITEC), Brno University of Technology.

Participation in Research Projects

TE02000011 “Research Center of surface treatments”, 2014 – 2019. Technology Agency of the Czech Republic (TA CR); WP7 – High adherence coatings (2012 - 2019); coordinator – Assoc. Prof. Ladislav Čelko.

LIST OF FIGURES

LIST OF TABLES

LIST OF SCHEMES